IONOACOUSTIC RANGE VERIFICATION OF CLINICAL PROTON BEAMS

M.Sc. Jannis Schauer

Vollständiger Abdruck der von der Fakultät für Luft- und Raumfahrttechnik der Universität der Bundeswehr München zur Erlangung des akademischen Grades eines

Doktors der Naturwissenschaften (Dr. rer. nat.)

genehmigten Dissertation.

1. Gutachter: Prof. Günther Dollinger

2. Gutachter: Prof. Katia Parodi

Die Dissertation wurde am 26.01.2023 bei der Universität der Bundeswehr München eingereicht und durch die Fakultät für Luft- und Raumfahrttechnik am 30.05.2023 angenommen. Die mündliche Prüfung fand am 19.07.2023 statt.

Zusammenfassung

Die Protonentherapie zur Bestrahlung von Tumoren hat entscheidende Vorteile gegenüber der herkömmlichen Methode mit Röntgenstrahlung. Die endliche Reichweite der Protonen mit einem Dosismaximum (Bragg-Peak) kurz vor dem Ende ihrer Reichweite ermöglicht eine höhere Dosiskonformität zum Tumor. Die Reichweitenunsicherheit der Protonen verhindert derzeit, dass die Vorteile der Protonentherapie voll ausgeschöpft werden können. Die Ionoakustik ist ein vielversprechender Ansatz, um die Reichweite der Protonen in situ zu messen und könnte eine Anpassung der Bestrahlung im Falle gemessener Abweichungen vom Bestrahlungsplan ermöglichen. Die Energiedeposition eines gepulsten Protonenstrahls erzeugt ein akustisches Signal, das nach seiner Propagation auf der Patientenoberfläche detektiert werden kann. Die Flugzeit des Signals ist ein Maß für den Abstand zwischen dem Bragg-Peak und dem akustischen Detektor. Diese Information kann auf elegante Weise mit einem Ultraschallbild kombiniert werden, sodass die Position des Bragg-Peaks relativ zur Anatomie des Patienten ausgewertet werden kann.

Ziel der vorliegenden Arbeit war der Nachweis von ionoakustischen Signalen bei Bestrahlungsdosen, die typische Bestrahlungsdosen in einer Fraktion von etwa $2\,Gy$ nicht überschreiten. Ionoakustische Signale von $20\,MeV$-Protonen wurden in einem Wasserphantom mit unterschiedlichen Pulsdauern und Strahlströmen gemessen. Die Signale wurden mit Hilfe eines Signal-Rausch-Verhältnisses (SNR_D) miteinander verglichen, das eine bestimmte Dosisgrenze berücksichtigt. Es wurde ein Signalverarbeitungsfilter entwickelt, der das SNR_D der Signale durch Korrelation mit einer simulierten Filterfunktion (Template) um einen Faktor 3-6 erhöht. Es wurde festgestellt, dass ein optimaler SNR_D bei Verwendung des maximal verfügbaren instantanen Strahlstroms erzielt wird. Die ideale Pulsdauer nimmt mit zunehmender Energie zu, und bei Pulsen, die die ideale Dauer überschreiten, ist es ratsam, den Puls in mehrere Pulse idealer Dauer aufzuteilen und anschließend die entsprechenden Signale zu mitteln.

Die Ergebnisse wurden in einem Folgeexperiment am Centre-Antoine-Lacassagne (CAL),

einem klinischen Protonentherapiezentrum in Nizza, Frankreich, angewandt. Ionoakustische Signale wurden auf der hautähnlichen Oberfläche eines anthropomorphen Abdominalphantoms mit einem Sensor gemessen, der starr an einer Ultraschallsonde befestigt war. Durch Anwendung des Korrelationsfilters auf die akustischen Signale, welche von einem einzelnen Protonen Pencilbeam erzeugt wurden, konnte eine stabile Flugzeit bei einer Dosis von $1,2\,Gy$ am Bragg-Peak bestimmt werden. Nach Auswertung von 48 unabhängigen Messungen wurde eine statistische Unsicherheit bezüglich der Position des Bragg-Peaks von etwa $0,5\,mm$ festgestellt. Mit Hilfe einer einzigen Kalibrierungsmessung unter Verwendung eines optoakustischen Aufbaus wurde die aus dem ionoakustischen Signal gewonnene Flugzeit verwendet, um die entsprechende Bragg-Peak-Position im Ultraschallbild relativ zur Anatomie des Phantoms robust zu markieren. Der Abstand zwischen der ausgewerteten Bragg-Peak-Position und der erwarteten Bragg-Peak-Position, welche durch eine Bestrahlungsplanung festgelegt wurde, beträgt $1,1\,mm \pm 0,5\,mm$ und ist damit kleiner als die Reichweitenunsicherheit, die Protonen bei der gegebenen Eindringtiefe von $4\,mm$ üblicherweise in einem klinischen Kontext zugeordnet wird. Die Messungen zeigen, dass die Ionoakustik die Möglichkeit einer Verifizierung der Reichweite im Submillimeterbereich in einer klinischen Umgebung bietet. Die ausgewertete Flugzeit kann nicht nur zur Messung der Entfernungsvariation verwendet werden, sondern lässt sich auch elegant mit einem Ultraschallgerät kombinieren, das die absolute Bragg-Peak-Lokalisierung durchführt. Die Möglichkeit, die Position des Bragg-Peaks in einem Ultraschallbild relativ zur Anatomie des Patienten zu bewerten, bietet die Möglichkeit, eine adaptive Tumorbestrahlung auf der Grundlage ionoakustischer Messungen durchzuführen und so den Nutzen der Protonentherapie zu erhöhen.

Abstract

Proton therapy for the irradiation of tumours has decisive advantages over conventional irradiation with X-Ray photons. The finite range of the protons with an emphasised dose maximum (Bragg peak) shortly before the end of their range allows a higher dose conformity to the tumour. Uncertainty regarding the proton range currently prevents the full benefits of proton therapy from being realised. Ionoacoustics is a promising approach to measure the range of the protons in situ and could allow the adjustment of the irradiation in case of measured deviations from the treatment plan. The energy deposition of a pulsed proton beam generates an acoustic signal which can be detected after its propagation to the patient surface. The time of flight of the signal is a measure of the distance between the Bragg peak and the acoustic detector. This information can be elegantly combined with an ultrasound image, showing the Bragg peak location of the protons relative to the anatomy of the patient.

The aim of the present work was the detection of ionoacoustic signals at irradiation doses that do not exceed typical irradiation doses in a fraction of approximately $2\,Gy$. Ionoacoustic signals using $20\,MeV$ protons were measured in a water phantom using different pulse durations and beam currents. The signals were compared with each other using a signal-to-noise ratio (SNR_D), which takes into account a given dose limit. A correlation-based signal-processing filter was developed, which increases the SNR_D of the signals by a factor of 3-6 by correlation with simulated filter templates. It was found that optimised ionoacoustic signal SNR_D is obtained using the maximum available instantaneous beam current. The ideal pulse duration increases with increasing energy and for pulses exceeding the ideal duration, it is advisable to split the pulse into several pulses of ideal duration and subsequently average the corresponding signals.

The findings were subsequently applied in a follow-up experiment at the Centre-Antoine-Lacassagne (CAL), a clinical proton therapy centre in Nice, France. Ionoacoustic signals were measured on the skin-like surface of a CIRS 3D abdominal phantom, using a sensor, which was rigidly attached to an ultrasound probe. Applying the correlation filter to the acoustic signals, a stable time of flight could be determined at a dose of $1.2\,Gy$ at the Bragg peak using a single proton pencil beam. After evaluation of 48 independent mea-

surements a statistical uncertainty regarding the Bragg peak position of approximately $0.5\,mm$ was found. By means of a single calibration measurement using an optoacoustic setup, the time of flight obtained from the ionoacoustic signal was used to robustly mark the corresponding Bragg peak location within the ultrasound image relative to the anatomy of the phantom. The distance between the evaluated Bragg peak position and the expected Bragg peak position obtained from irradiation plannig ($1.1\,mm \pm 0.5\,mm$) is smaller than the range uncertainty typically assigned to protons at the given penetration depth ($4\,mm$).

The measurements demonstrate that ionoacoustic offers the possibility of a sub-millimetre range verification in a clinical setting. The evaluated time of flight can not only be used to perform range variation measurements but it can be elegantly combined with an ultrasound device performing absolute Bragg peak localisation. The potential to evaluate the Bragg peak position in an ultrasound image relative to the anatomy of the patient offers the possibility to perform adaptive tumour irradiation based on ionoacoustic measurements and thus increase the benefits of proton therapy.

Table of Contents

Glossary

CAL Centre Antoine Lacassagne.

CT Computed tomography.

CTV Clinical target volume.

CW Continuous wave.

DAQ Data acquisition.

FWHM Full width half maximum.

HU Hounsfield units.

IMPT Intensity modulated proton therapy.

IMRT Intensity modulated radiation therapy.

LNA Low-noise amplifier.

MAPS Moving average power spectrum.

MCS Multiple coulomb scattering.

MLL Maier-Leibnitz-Laboratory.

MRI Magnetic resonance imaging.

NTCP Normal tissue complication probability.

OAR Organ at risk.

PBS Pencil beam scanning.

PET Positron emission tomography.

PMMA Poly(methyl methacrylate).

PMT Photomultiplier tube.

PTV Planning target volume.

RBE Relative biological effectiveness.

SEM Standard error of the mean.

SNR Signal-to-noise ratio.

SOBP Spread out Bragg peak.

SPR Stopping power ratio.

TCP Tumour complication probability.

TIR Total impulse response.

ToF Time of flight.

US Ultrasound.

Chapter 1

Introduction and motivation

According to the World Health Organisation, cancer, along with cardiovascular disease, is the leading cause of death for people between the ages of 30 and 70 in 120 countries around the world [1]. In Germany alone, about half a million people contract cancer every year. This means that about one in three people in Germany will develop cancer in the course of their lives [2].
However, cancer is no longer the incurable disease it is still considered to be. About half of all affected people defeat cancer thanks to at least one of the four main pillars in the fight against cancer. These pillars are surgery to remove the malignant tissue, drugs, including above all chemotherapy, immunotherapy and radiotherapy [2]. In about half of all tumour cases, radiotherapy is involved as a healing tool [2]. Statistically speaking, this means that in the course of a lifetime, one in six Germans is treated with radiotherapy. It is therefore no surprise that the improvement of radiotherapy is the subject of countless current research areas.

1.1 Radiation therapy

The goal of any tumour irradiation is to kill the tumour cells by destroying their DNA. This is achieved using ionising radiation, which enters the tumour region and deposits energy there [3]. The most important parameter in quantifying the correlation between radiation and cell death is the deposited biological dose D which is the deposited energy E per unit mass m.

$$D = \gamma \frac{E}{m} \tag{1.1}$$

The factor γ is the relative biological effectiveness (RBE) and describes a dose enhancement factor dependent on the type of radiation. For high energy X-rays $\gamma = 1$, for protons

used in clinics $\gamma = 1.0 - 1.1$ and for heavier ions $\gamma > 1.1$. The deposited dose leads to a damage in the DNA, which happens either by direct interaction of the DNA with the incident radiation or by radiation-induced free radicals [4]. Here, the incident radiation reacts, for example, with oxygen and thus produces highly reactive oxygen radicals that damage the DNA in a chemical reaction. Both mechanisms, direct and indirect, lead to breaks in one or both strands of the DNA. In principle, a cell is equipped with a repair mechanisms to eliminate damage of this kind, however, if the DNA of the cell is damaged too severely, the DNA repair mechanisms fail and the cell loses the ability to divide or is killed directly by apoptosis or necrosis. The degree of cell damage depends on the number and location of DNA strand breaks. Double strand breaks and double strand break clusters are particularly difficult to repair, as both strands of the DNA double helix are damaged. The irradiation of a cell with $1\,Gy$ of dose using X-rays radiation induces approximately 50 double-strand breaks and 500-1000 single strand breaks [5].

While it is desirable to limit the dose deposition only to the tumour volume, it has to be accepted that a proportion of healthy cells will always be exposed to a non-negligible dose by any kind of radiation therapy. However, in contrast to healthy cells, tumour cells are typically more susceptible to damage by radiation exposure, mainly due to the fact that they divide much faster [6]. This difference in radiation tolerance opens a window, the so-called therapeutic window, which is the difference between the tumour control probability (TCP) and the normal tissue complication probability (NTCP) at a given dose. An illustration of the therapeutic window in shown in figure 1.1.

To date, research is underway to increase this therapeutic window. One important component in increasing the therapeutic window is to reduce the dose deposition in the healthy tissue as much as possible. Depending on the tumour, this can be realised by either internal radiotherapy (Brachytherapy), external radiotherapy or combinations thereof. In Brachytherapy one or more radioactive sources are implanted into or close to the the malignant tissue and either removed after a certain amount of time or implanted permanently [7]. Within external radiotherapy, that is the irradiation of the tumour volume from outside the patient, a dose reduction in the healthy tissue can be realised by irradiation of the tumour volume from different directions. By distributing the radiation energy over a larger volume, the dose in the normal tissue is reduced and the NTCP decreases. A

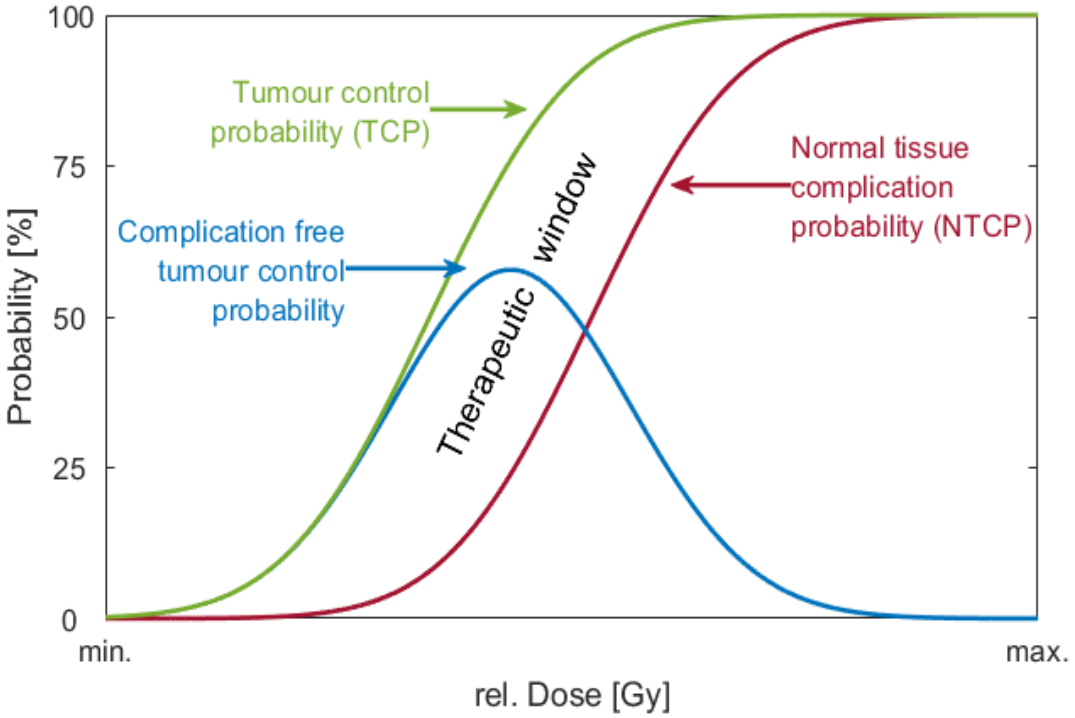

Figure 1.1: Schematic illustration of the therapeutic window. The difference in probability between the the TCP (green) and the NTCP (red) opens a therapeutic window. The size of the therapeutic window is a measure of the complication free tumour control probability (blue) which peaks at the ideal treatment dose. The size of the therapeutic window is dependent on a number of factors related to the tumour location and size.

further development of this multi-directional approach is to irradiate parts of the tumour mainly from one direction while other parts are mainly irradiated from another direction, which is called intensity modulated radiotherapy (IMRT) [8]. Additionally, external radiotherapy makes use of the fact that the regenerative capacity of healthy cells is typically higher than that of tumour cells. It is thus common practise to deliver the total dose is fractions (e.g. 30 times $2\,Gy$ over the period of six weeks) [8] in order to increase the therapeutic window further. A different approach of increasing the therapeutic window in external radiotherapy further is the use of ions, often but not always protons, instead of the commonly used X-ray photons. The clinical use of protons was first proposed in 1946 by Robert Wilson [9] and first used clinically in 1954 [10]. Since then, over 250000 people have undergone proton therapy [11].

1.2 Proton therapy

The advantage of proton therapy over conventional X-ray therapy lies in the characteristic depth-dose distribution of the protons. A comparison between the depth dose distribution of protons and X-ray photons is shown in figure 1.2: The depth dose distri-

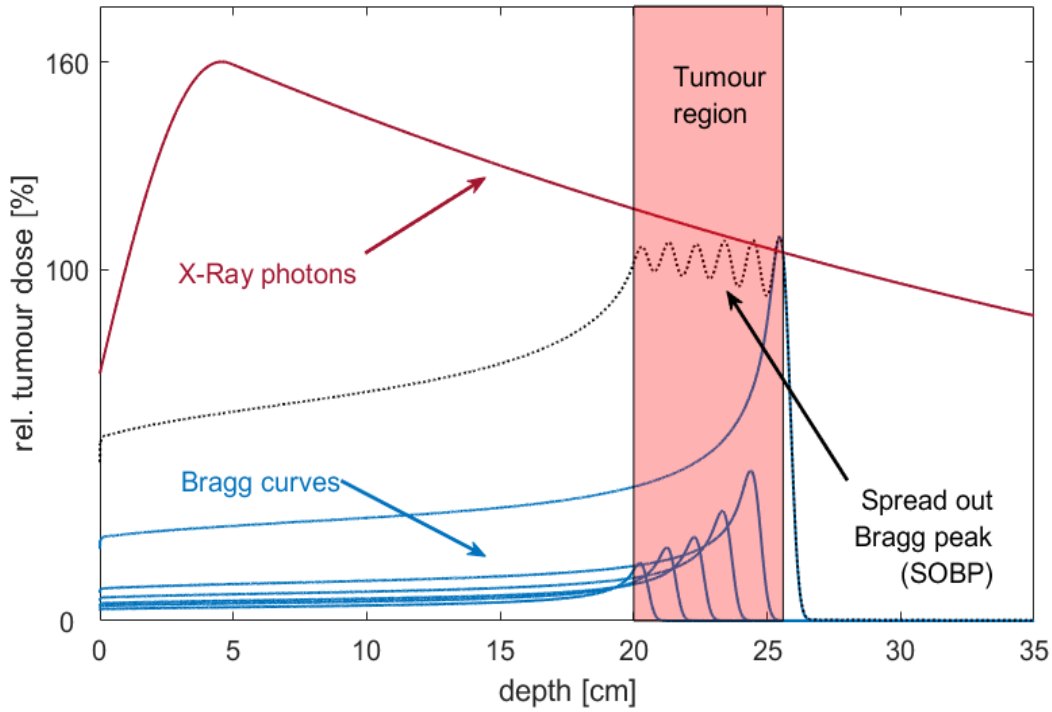

Figure 1.2: Comparison of the depth dose curves of X-ray photons (red) and protons (blue). The X-ray depth dose curve is described by an exponential decay with an initial build up effect. The depth dose deposition of a proton beam of a single energy is called the Bragg curve. By superimposing multiple Bragg curves with varying energy, a so-called spread out Bragg peak (black) can be generated. The more different energies are used for superposition in the SOBP, the more homogeneous is the resulting dose distribution in a potential tumour region (red area).

bution of conventionally used X-ray photons (red) follows an exponential decay after an initial build up region [8]. The build-up effect for photons is directly correlated with the range of the secondary electrons generated in the skin and is therefore located deeper the higher the photon energy is [8]. The maximum dose deposition is thus located closely behind the skin independent on the tumour position.

In contrast, the depth dose distribution of protons, so-called Bragg curves (blue), peak at a finite range, which increases with increasing energy. This location of maximum dose

deposition is called Bragg peak and is ideally located inside the tumour volume. By combining proton beams of different energies, a nearly homogeneous dose distribution can be generated over the entire tumour volume. This is the so-called Spread out Bragg peak (black), SOBP for short, which is used in proton therapy. Using a SOBP, tissue located in front of the tumour volume will not only be exposed to significantly less dose compared to conventional X-ray therapy but will also receive less dose than the tumour volume. Tissue located behind the tumour will be exposed to a negligible amount of dose. The more different energies are used for the generation of the SOBP, the more of a homogeneous dose distribution can be achieved. It has been shown that the use of protons - depending on the tumour and the quality of the irradiation equipment - can reduce the integral dose applied to the body by a factor of 2-3 [12]. At this point it should be mentioned that the use of protons over X-ray photons has the disadvantage of higher treatment costs by about a factor of 2 [13]. Proton therapy is therefore often used for children, since children benefit most from the advantages of the more beneficial dose distribution, resulting, among others benefits, in a reduced probability of secondary tumours.

1.3 Treatment planning

The task of treatment planning includes to adjust the dose to be delivered to the patient as conformal as possible to the tumour volume. For this purpose, the patient is imaged using X-ray computed tomography (CT), potentially in combination with other imaging methods like positron emission tomography (PET) or magnetic resonance imaging (MRI). From the images the tumour location and size is subsequently deduced as well as the position of surrounding organs, which should ideally be kept free of dose. Based on the CT image, it is then decided from which directions and how much dose is to be deposited. Particular care is taken to spare the surrounding organs, the so-called organs at risk (OAR). Even though OARs cannot be spared entirely, care is taken not to exceed certain thresholds of dose, which are dependent on the irradiated organ and the irradiated volume of the organ. In order to select the desired proton energies, the tissue in the beam path is characterised with regard to the ability to decelerate protons, which is done on the basis of the CT image. Before irradiation, the patient is positioned on a movable table,

which is subsequently positioned relative to the proton beam. The beam is typically delivered by means of a rotatable beam line, which allows for an irradiation from multiple directions.

Unfortunately, the procedures of treatment planning and beam delivery are prone to errors. The errors in treatment planning mostly arise due the uncertainty of the CT grey scale values (Hounsfield Units, HU) and their conversion to proton therapy specific quantities like the stopping force, which is decisive for the proton range [14]. This process is further complicated by the limited quality of the CT image due to its resolution, artefacts or noise. The errors in beam delivery are mainly due to anatomical changes of the patient [14] relative to the day of treatment planning. This can be, for example, an increase or decrease in weight or different filling levels of the bladder or intestine. As treatment planning is typically only done once and prior to the first irradiation, these changes may not be taken into account in following fractions of the irradiation. In addition, positioning accuracy of the patient and the movement during irradiation can be an aggravating factor. Although the patients are positioned in a plaster imprint that is created in the beginning of the treatment planning, movements and positioning inaccuracies of several millimetres cannot be ruled out. Depending on the proton facility the assumed uncertainty regarding the distal dose gradient varies. On average a range uncertainty of approximately 3.5% of the range of the protons plus one additional millimetre independent of the proton range is assumed [15]. For deep seated tumours, e.g. in $20\,cm$ depth, this leads to range uncertainties of up to $8\,mm$.

To ensure that, despite these range uncertainties, the entire tumour volume is irradiated with the prescribed dose and no OARs are severely harmed, the actual tumour volume is increased by these uncertainties to form the planning target volume (PTV). Since the PTV is in any case larger than the actual tumour, these safety margins lead to increased normal tissue reactions, since healthy tissue around the tumour is intentionally irradiated with high dose. In addition, this enlarged irradiation volume can lead to the exclusion of ideal irradiation directions, as otherwise OARs would be exposed to a dose which exceeds the maximum dose allowed for this organ, as it is the case with prostate irradiation [16]. The current standard plan is to irradiate the prostate from two directions laterally through the hip bone in order to protect mainly the rectum but also other OARs from

too much radiation exposure. As shown in Tang et. al. [16], anterior irradiation through the bladder or from two directions laterally past the bladder could reduce the dose in all involved OARs except the bladder and would be beneficial, if the large error ranges of the PTV did not prohibit these directions.

1.4 Range verification in ion beam therapy

The reduction of the PTV by better knowledge of the Bragg peak position in the tissue can therefore help to realise more advantageous irradiation geometries in some cases and in any case reduce side effects by reduction of dose deposited in the healthy tissue. Several approaches are being pursued to measure the Bragg peak position online during irradiation.

Arguably the most advanced technique, which has already been clinically tested, is prompt-gamma-imaging [17]. This method is based on the detection of gamma-ray photons, which are generated when target nuclei excited by collision with the impinging protons return to their ground state within nanoseconds. The prompt-gamma-rays are typically detected in a direction perpendicular to the beam axis using, for example, a slit camera. The further procedure differs depending on the research group, but the goal is to use either the energy of the gammas (prompt-gamma-spectroscopy) or the number of detected gammas to draw conclusions about the proton energy and thus the range of the protons [18, 17]. Advantages of this method are its universal applicability independent of irradiation site in the body or irradiation facility. Disadvantages are the expensive instrumentation and the fact that the range of the protons is measured in the coordinate system of the detector. This information is only suitable to measure range differences between two proton beams [19] or the information needs to be mapped onto an image showing the patients anatomy, which is prone to errors. In addition, the generation of prompt-gamma-rays decreases as the energy of the protons decreases, resulting in significantly fewer gammas being generated at the Bragg peak itself than in the previous beam path [20]. Nevertheless, with this method, submillimetre measurements in homogeneous phantoms could be achieved [19].

In contrast to prompt-gamma detection, which uses high-energy photons ($2\,MeV - 10\,MeV$)

[21], positron emission tomography (PET) imaging focuses on $511\,keV$ photons being emitted from β^+-emitters, which are also produced in nuclear interaction of the protons with the target material [22]. The recombination of this positron with an electron in the tissue results in two anti-parallel $511\,keV$ photons as annihilation radiation, which can be detected using PET cameras. As with the usage of prompt-gamma-rays, this process depends on the energy of the protons. From the spatial and temporal distribution of the photons, the annihilation density in the patient and thus the proton range can be deduced. The usage of prompt-gamma-photons and PET share similar advantages and disadvantages however, for PET this is complicated by the fact that the half-lives of β^+-emitters range from milliseconds to minutes. During this time, the respective isotopes can be delocalised, which leads to the so-called wash out effect that complicates the interpretation of the signal [23].

Ionoacoustics, on the other hand, takes a completely different approach for range verification, which, as the name suggests, is acoustic in nature. The dose deposition of a pulsed proton beam causes a minimal temperature increase ($\approx 0.5\,mK$ at $2\,Gy$ dose) which causes a local pressure change. This pressure can be measured with acoustic sensors after its propagation to the patient surface at the skin. In combination with a stable trigger that marks the arrival time of the protons, the time of flight of the pressure wave from its origin at the Bragg peak to the detector can be measured. This information is a measure for the distance between the Bragg peak and the recording sensor, which is not to be mistaken for the proton range measured from the beam entrance of the patient. The main advantages of this method are the simple measurement setup and the comparatively cheap measurement instruments as well as the fact, that the signal is predominantly generated at the location of interest - the Bragg peak. One disadvantage of ionoacoustics is the requirement of a pulsed beam. Currently only few clinical accelerator are suited for ionoacoustic signal generation, however, any kind of proton or heavy ion accelerator could be turned suitable by installing additional pulsing equipment. One additional challenge in ionoacoustics are the noisy signals at clinically relevant dose depositions.

1.5 State of the art and goal

The first experimental evidence of ionoacoustic signals was provided as early as 1979 by Sulak et al. [24]. In this first paper, the signal origin was deduced and the possible application field of beam monitoring or range verification was already recognised. While there were some publications on the topic in the following years [25], the field of ionoacoustics fell out of the focus of scientific research and was only taken up again around 2014 from several groups independently of each other [26, 27, 28, 29]. In this work and follow-ups, the ionoacoustic signal was simulated in detail and the dependencies of the signal on the spatial and temporal structure of the source were investigated [30]. It was found that the central frequency of the signal depends on the spatial extend of the underlying dose distribution as well as the duration and shape of the proton pulse. A method was also established to simulate the signal under realistic conditions, i.e. with heterogeneities in the beam path and the acoustic path [30, 31]. In the work of Lehrack and Assmann, the signal was measured both with low-energy $20\,MeV$ protons [29] and with a clinical energy of $220\,MeV$ [32] and range evaluation coincided with simulation results with sub-millimetre accuracy. In the work of Kellnberger et al. [33], the Bragg peak was imaged using an array of sensors in an inhomogeneous mouse leg phantom.
However, all of this work was limited to simplified conditions in one or more ways. In some experimental demonstrations, a clinically typical dose of $2\,Gy$ was significantly exceeded in order to improve the signal-to-noise ratio (SNR) for reliable signal detection [32]. The ionoacoustic signal detection can also be simplified by using low-energy protons since they produce higher frequency ionoacoustic signals that are more easily detectable [29, 33]. Lastly, most experiments made use of homogeneous phantoms to exclude influences from material heterogeneities in the beam or acoustic path [28, 29, 32].
The aim of this work was first and foremost to significantly increase the SNR of the ionoacoustic signal to reliably detect the ionoacoustic signal at clinical energies, doses and in realistic target phantoms and thus to prove the applicability of ionoacoustics under realistic conditions. In addition, the goal was to extract the range information from the signal and combine it with an ultrasound imaging device to obtain a relative range verification to the anatomy of the irradiated phantom.

Chapter 2

Theoretical concepts of ionoacoustics and signal processing

2.1 Ions in tumour therapy

Ions are by definition atoms or molecules with an electric charge. For tumour therapy, mainly protons are used, which is a hydrogen nucleus with a mass of $m = 1u \approx 1.66 \times 10^{-27}\,kg$ and a charge of $q = 1e \approx 1.60 \times 10^{-19}\,C$. In some facilities, heavier ions are also used for tumour treatment, such as Helium ($m = 4u$, $q = 2e$) , Carbon ($m = 12u$, $q = 6e$) or Oxygen ($m = 16u$, $q = 8e$) [34]. The heavier ions offer a slight advantage in comparison to protons as they increase their RBE at the end of their range and their Bragg peak is sharper in the lateral and in the longitudinal direction, which is advantageous in terms of dose conformity to the tumour volume. However, heavy ions are significantly more difficult and expensive to accelerate and deliver to the tumour site [34]. Although the relationships described in this thesis apply qualitatively to both protons and heavier ions, the quantitative statements always refer to protons unless explicitly stated. The tumours which are suitable for irradiation with protons are typically located at a depth between $0\,cm - 40\,cm$ under the skin. To reach this depth of penetration into the body, the protons need kinetic energies of up to $260\,MeV$, where $1\,MeV \approx 1.60 \times 10^{-13}\,J$. Therefore, they enter the body at up to 60% of the speed of light.

In modern facilities, the beam is delivered through a rotatable beam line called gantry. With the help of a gantry it is possible to set the ideal irradiation position and angle. The point around which the gantry rotates is called the isocentre. Typically, the beam is applied with the so-called pencil beam scanning (PBS) method. In pencil beam scanning a beam of small lateral extend, typically quantified by the standard deviation of its Gaussian shape in the lateral dimension ($\sigma \approx 5\,mm$), is scanned across the tumour volume using scanning magnets. In order to reach all depths of the tumour, the energy of the beam is adjusted accordingly.

2.1.1 Acceleration

The generation of such high-energy protons requires the use of particle accelerators. For this work, experiments were carried out at two different accelerators, the operating principles of which are briefly explained below.

The first type is a linear accelerator, which are typically used for preclinical or research purposes rather than clinical ones. One possible setup for such a linear accelerator is a so-called tandem accelerator, which was installed at the Maier-Leibnitz-Laboratory (MLL) in Garching near Munich until January 2020. This tandem accelerator could accelerate protons up to $28\,MeV$. For the acceleration of protons, first negative hydrogen ions (H^-) are produced, which, after having undergone a pre-acceleration, are fed into a tank filled with an insulating gas (e.g. sulphur hexafluoride, SF_6) [35]. A large positive voltage is generated in the centre of the tank (up to $14\,MV$) using a Van-de-Graaff-generator. This voltage accelerates the negative ions within a vacuum tube to the centre of the tank, where they pass through a so-called stripper foil (e.g. carbon) which strips off the electrons of the projectiles, thus converting the negative hydrogen ions into protons. From here the potential difference is passed through again, resulting in a continuous wave (CW) proton beam with an energy of $E = 2qU$ at the end of the tank. As ionoacoustics requires pulsed beams, the CW-beam of a tandem accelerator will not produce any ionoacoustic signal. However, a CW-beam can be converted into a pulsed beam by the use of a chopper. A chopper consists of one or more pairs of conducting plates positioned on opposite sides of the beam forming a capacitor. By applying a potential difference, the beam is deflected from its original direction and thus be switched on and off.

Even though linear accelerators can be used for clinical applications [36], cyclic accelerators are better suited for this purpose because of their cost-effectiveness and compactness. In particular, clinical facilities mostly use cyclotrons. A cyclotron consists of two D-shaped metal electrodes, the so-called dees, in a vacuum chamber, between which an alternating electric field $\vec{E}$ is applied and whose interior is field-free. The proton source is positioned in the middle of the two dees. In addition, the entire apparatus is penetrated by a static magnetic field $\vec{B}$, which is oriented perpendicular to the electric field. Within the dees, the protons experience the Lorentz force $\vec{F_L}$, which is proportional to their charge

q and their speed $\vec{v}$. The Lorentz force $\vec{F}_L = q\vec{v} \times \vec{B}$ acts perpendicular to the particle velocity and the magnetic field, forcing the particle on a circular path without changing its magnitude of velocity. Between the dees, the protons are accelerated by the electric force $\vec{F}_{el} = q\vec{E}$. By switching the electric field at the correct frequency, the so-called cyclotron frequency f_c, an increase in velocity is achieved with each passage through the gap between the dees.

$$f_c = \frac{q|\vec{B}|}{2\pi m} \tag{2.1}$$

This frequency is independent of the proton velocity and can therefore be kept constant given that all particles share the same charge and mass m. The resulting beam is frequency modulated by the underlying cyclotron frequency in the order of $10^7\,Hz - 10^8\,Hz$, which is often called a quasi-CW beam. However, standard cyclotrons are not suitable for proton therapy since the limit of a cyclotron is reached when the mass of the proton increases significantly, due to relativistic effects. This limit is reached at about 10% of the speed of light, which corresponds to a resulting proton energy of about $5\,MeV$ [37]. To overcome this limitation according to eqn. 2.1, either the magnetic field can be adjusted to the relativistic mass of the protons (isochronous cyclotrons and synchrotrons) or the cyclotron frequency can be adjusted accordingly (synchrocyclotron). Most clinical proton facilities use isochronous cyclotrons [38], however these are unsuitable for ionoacoustics, as they generate quasi-CW-beams and thus not suitable pulses for ionoacoustic signal generation. However, pulsed beams may be generated by installing an additional chopper system in front or behind the cyclotron.

The successor of the standard cyclotron that is best suited for ionoacoustics is the synchrocyclotron. Here, the cyclotron frequency is not kept constant, but is slowed down for high energies, adapted to the relativistic effects [39]. A consequence of this adapted cyclotron frequency is the fact that the current cyclotron frequency only matches a tiny fraction of the protons in the beam line. All protons that are not in phase with the current cyclotron frequency are not accelerated, resulting in a beam that comes in short pulses with a duration in the order of microseconds with a low repetition frequency of the individual pulses in the order of $1\,kHz$. The pulse duration divided by the total repetition period is called the duty cycle and is for synchrocyclotron in the range of 0.1%-2% [39].

Apart from cyclic accelerators, the commissioning of the first 3GHz linac for proton therapy is currently underway [40] (as of 2018). The LIGHT (Linac for Image-Guided Hadron Therapy) project plans patient irradiations with proton energies of up to $230\,MeV$. The pulse duration (up to $5\,\mu s$) and the pulse repetition rate ($200\,Hz$) make this type of accelerator very promising for the application of ionoacoustics.

2.1.2 Interaction of ions with matter

When ions are extracted from the vacuumised beam line, they interact with the medium surrounding them. This interaction takes place on the one hand with the negatively charged shell electrons of the medium and on the other hand with the positively charged atomic nuclei of the medium. These interactions reduce the velocity of the proton in the longitudinal direction with the result that the particle comes to a standstill after a finite range. Additionally, these interactions cause a deflection in the lateral direction, causing the beam to increase in diameter with increasing depth.

Energy loss

The energy loss that slows down the protons and is therefore also responsible for their standstill is quantified by the stopping force S, which is often misleadingly referred to in the literature as stopping power. It is defined as the energy released by the incident particle per unit path length, $S = -\frac{dE}{dx}$. In this formula, a material property, namely the stopping force, is linked to the property of the penetrating particle, namely its energy loss per distance. For proton energies relevant for this work ($20\,MeV - 260\,MeV$), the stopping force can be described in a good approximation exclusively with the electronic stopping force [41], which results from the interaction of the protons with the shell electrons of the surrounding medium. For the given energies, this electronic stopping force is well approximated by the Bethe formula:

$$-\frac{dE}{dx} = \frac{4\pi n z^2}{m_e c^2 \beta^2}\left(\frac{e^2}{4\pi\varepsilon_0}\right)^2\left[ln\left(\frac{2m_e c^2\beta^2}{I(1-\beta^2)}\right) - \beta^2\right] \tag{2.2}$$

Equation 2.2 describes the electronic stopping force in its relativistic form. It is dependent on material specific quantities such as the electron density n, the mean excitation

potential I, as well as particle specific quantities like its charge z and its relative velocity $\beta = \frac{v}{c}$. Additionally m_e is the electron mass and e its charge, ε_0 is the vacuum permittivity and c is the speed of light.

For non-relativistic protons, the dependence $-\frac{dE}{dx} \sim \frac{ln(v^2)}{v^2} \sim \frac{ln(E)}{E}$ can be recognised. It shows that the energy loss of the proton increases with decreasing velocity and energy and therefore also with the penetration depth into the material. The energy transfer of the proton to the medium thus maximises shortly before its standstill. In a therapeutic context, the energy transfer is typically discussed in terms of a dose deposition, where the transfer from energy to dose is given by $E = mD$ with m being the mass in which the energy is deposited. Although the range of the proton and the location of maximum dose deposition can under certain assumptions be analytically calculated from the stopping force [42, 43], it is not straight forward to accurately take into account statistical fluctuations, the so-called range straggling. Range straggling describes the phenomenon that even for identical initial conditions, the proton range fluctuates around a mean value. For water as a stopping medium, this range straggling increases almost linearly with the initial particle energy [44]. These statistical processes can be most accurately modelled by the use of so-called Monte Carlo simulations. Such simulations govern the statistical processes by dividing the proton path into small steps and providing a probability of all possible interactions taking place. The number of interactions that are undergone by a proton thus differ from proton to proton and therefore accurate depth-dose distributions can be simulated. The mean depth dose deposition resulting from the simulation of enough (typically $\sim 10^6$ particles) is called the Bragg curve. The Bragg curve follows a very characteristic course with a pronounced maximum, the Bragg peak, just before the proton comes to a standstill. Simulations of Bragg curves for monoenergetic proton beams of energies between $70\,MeV$ and $250\,MeV$ are shown in Fig. 2.1. For each curve, the dose deposition of 10^5 protons was simulated in water. The dose was scored in slabs of size $5\,cm \times 5\,cm$ with $100\,\mu m$ thickness in beam direction.

It can be seen that with increasing energy and thus range the maximum dose drops and the Bragg peak broadens. The reason is is the range straggling effect, which causes a larger range deviation between the individual protons taken into account for the simulation of the Bragg curve for one particular proton energy.

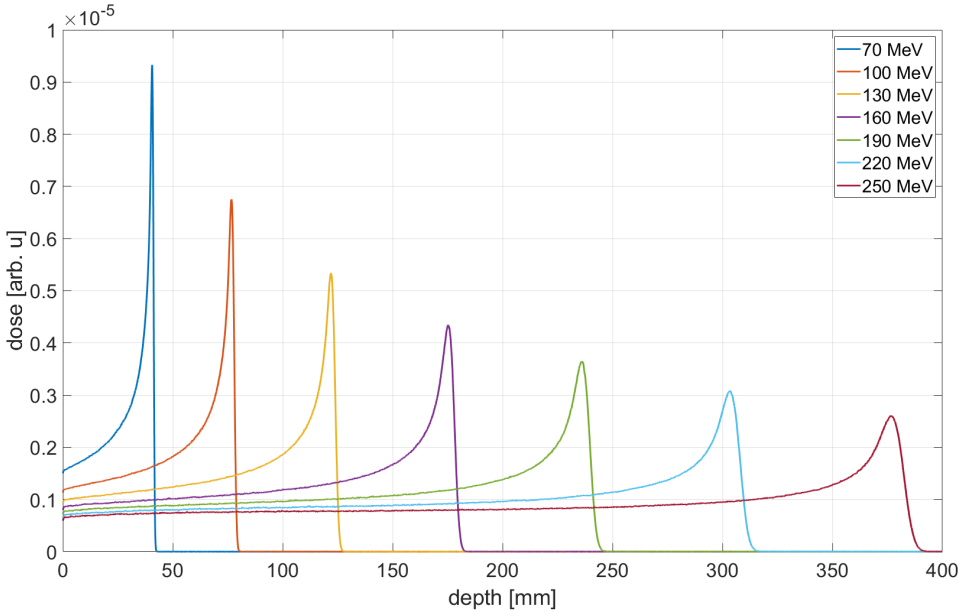

Figure 2.1: Monte Carlo simulation providing the Bragg curves for monoenergetic proton beams in water. With increasing energy, the penetration depth increases, while the Bragg curve flattens.

Lateral beam profile

Apart from interactions with the shell electrons, which are decisive for the proton range, there are interactions between the incident proton and the nuclei of the target material, which exert a repelling force on the positively charged protons according to Coulomb's law. The Coulomb force originates almost exclusively from interaction with the nuclei of the atoms, since the influence of the shell electrons on the trajectory of the protons has practically no effect because of the large mass difference ($\frac{m_p}{m_e} \approx 2 \times 10^3$).
For single scattering events and under the assumption that the scattering potential is exclusively caused by a point-like nucleus, the probability of an incident proton to be scattered by an interaction with a nucleus under the angle θ and to be detected in the solid angle element $d\Omega$ is given by the Rutherford scattering formula.

$$\frac{d\sigma}{d\Omega} = \left(\frac{1}{4\pi\varepsilon_0}\frac{Z_1 Z_2 e^2}{4E_0}\right)^2 \frac{1}{sin^4(\frac{\theta}{2})} = \frac{j_{sec}(\Omega)}{j_{prim}} \tag{2.3}$$

Here, $\frac{d\sigma}{d\Omega}$ is the so-called differential cross section, ε_0 is the electric field constant, $Z_{1,2}$ are the charge number of the projectile and atomic nucleus, respectively and E_0 is the ini-

tial energy of the projectile. The last equals sign shows that the differential cross section can be understood as the the particle current density in the solid angle element $d\Omega$ (in units particles per solid angle and time) divided by the incident particle current density measured in particles per area and unit time for a given scattering angle θ.

The approximation of the Rutherford scattering becomes inaccurate for very small scattering angles as well as for very large scattering angles. For very small scattering angles, the distance between proton and nucleus is so large that a screened potential would have to be used, which takes into account that the effective nuclear charge is reduced by the shell electrons. For very large scattering angles, the finite expansion of the atomic nucleus would have to be taken into account for an accurate description.

In order to describe the lateral distribution of a proton beam as accurately as possible not only small and large angle scattering need to be modelled correctly, but also multiple scattering events need to be taken into account. This is realised be the usage of Monte Carlo simulations. While a certain uncertainty in specific interaction probabilities remains [45], Monte Carlo simulations still provide a very accurate description of the lateral beam distribution. A Monte Carlo simulation of a proton beam of $126\,MeV$ protons and an initial size of its Gaussian envelope of $\sigma = 3.5\,mm$ is shown in Fig. 2.2.

The characteristic trumpet shape in figure 2.2 is produced by several small angle scattering events which is referred to as multiple coulomb scattering (MCS). The distribution of protons occurring from this MCS effect is described for example by Lynch et al. [46] and leads to a near Gaussian distribution of protons in the lateral direction perpendicular to the beam axis assuming small angles. For larger angles the number of protons is higher than what would be expected from a single Gaussian distribution.

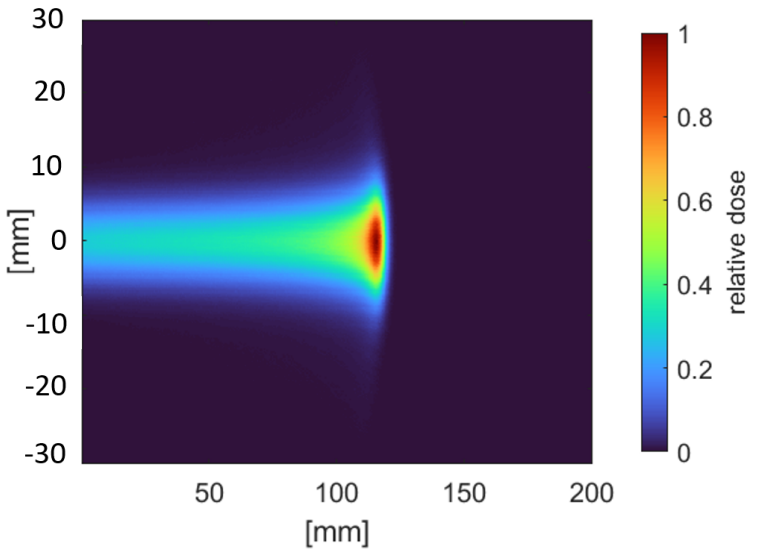

Figure 2.2: Monte Carlo simulation of the dose distribution of a proton beam in water coming from the left. The relative dose is projected onto two dimensions and indicated by the colour bar.

2.2 Ionoacoustic signal generation

Ionoacoustic signal generation and propagation as discussed in this section is limited to a homogeneous signal generation and propagation medium. The influence of more realistic geometries including acoustic heterogeneities are discussed in the proceeding section 2.3 in the context of ultrasonic probes.

The ionoacoustic signal in an homogeneous medium is composed of four fundamental components. The first component is the underlying dose distribution, which is primarily determined by the number and energy of the protons and the media they enter. The second component is the propagation of the initial pressure to the detection sensor. Even if acoustic phenomena like reflections are neglected as homogeneous media are assumed, this propagation can have an influence on the ionoacoustic signal amplitude and shape depending on the relative position between the detector and the source. The third component is the temporal structure of the excitation, given by the shape and duration of the proton pulse. And the fourth component is the recording process including the central frequency of the detector and its spatial extend, but also secondary electronics like amplifiers and filters.

2.2.1 Initial pressure derivation

The relationship between the energy deposition of a proton beam and the resulting pressure can be established with the help of the dimensionless Grüneisen parameter Γ. The Grüneisen parameter describes the change of the pressure dp at a given energy deposition dE related to the volume V in which the energy is deposited [47].

$$\Gamma = V\left(\frac{dp}{dE}\right)_V \tag{2.4}$$

The Grüneisen parameter describes this relationship under the assumption of a constant volume. For the derivation of the initial pressure resulting from a proton beam it must thus be assumed that the energy deposition is isochoric. Under this assumption, the increase in pressure with the deposited energy is:

$$dp = \Gamma\frac{1}{V}dE \tag{2.5}$$

In general, Γ is a temperature dependent factor an thus dependent on the deposited energy. According to Wang and Wu [48], the Grüneisen parameter for water can be estimated to be $\Gamma = 0.0043 + 0.0053T$ with T being the temperature in degree Celsius. This approximation must be taken with caution as there is a lack of systematic research on the Grüneisen parameter and the limits of this temperature dependency are not indicated in the cited book.

The temperature increase ΔT caused by a certain energy deposition ΔE is given by the specific heat capacity C, which can be rewritten in terms of the dose deposition D.

$$\Delta T = \frac{\Delta E}{mC} = \frac{D}{C} \tag{2.6}$$

In the case of a clinical dose of $1\,Gy$ which is applied instantaneously, this results in a temperature increase of about $0.24\,mK$. It can therefore be assumed that the Grüneisen parameter is constant [48, 47] in the range of the energy depositions, which are of interest

and the pressure increase Δp induced by a certain energy deposition can be written as:

$$\Delta p = \Gamma \frac{1}{V} \Delta E \tag{2.7}$$

By extending the right-hand side of the equation with the mass m, the pressure can be described as a function of the deposited dose D and the mass density ρ.

$$p_0 = \Gamma \rho D \tag{2.8}$$

This formulation is consistent with the derivations of Lehrack et al. [49], Jones et al. [50] and Hickling et al. [51]. For a short proton pulse depositing a dose of $1\,Gy$ at the Bragg peak in water at room temperature, this yields an initial pressure of about $150\,Pa$ which corresponds to an acoustic displacement in the order of $100\,pm$.
An alternative description of the Grüneisen parameter, which will be used in the next section, uses the isothermal compressibility β, the specific heat capacities at constant pressure C_p, and the speed of sound v_s [47].

$$\Gamma = \frac{\beta v_s^2}{C_p} \tag{2.9}$$

2.2.2 Pressure propagation to the detector for delta-shaped excitations

Neglecting heat diffusion, the time evolution of the signal is described by the well established general acoustic wave equation with a heat induced source [52, 53, 54].

$$\left(\Delta - \frac{1}{v_s^2}\frac{\partial^2}{\partial t^2}\right) p(\mathbf{r},t) = -\frac{\beta}{C_p}\frac{\partial}{\partial t} H(\mathbf{r},t) \tag{2.10}$$

Here, the left side describes the wave propagation with the Laplace-Operator Δ and the speed of sound v_s and the right side represents the source term. Here, the heating function H is introduced as the heat input per unit volume and unit time in units $[Jm^{-3}s^{-1}]$. From eqn. 2.10 it can already be deduced that a constant heating (CW-beam) will not produce any signal, as the source term is proportional to the temporal derivative of H.
The general solution for this equation can be found with a Greens function approach, as

demonstrated in Wang et al. [55] or can be looked up in the literature [56, 57].

$$p(\mathbf{r},t) = \frac{\partial}{\partial t}\frac{\beta}{4\pi C_p}\iiint \frac{d\mathbf{r'}}{|\mathbf{r}-\mathbf{r'}|}H(\mathbf{r'},t') \quad \Big|_{t'=t-\frac{|\mathbf{r}-\mathbf{r'}|}{v_s}} \tag{2.11}$$

This solution is given in the coordinate system of the origin, as illustrated by figure 2.3.

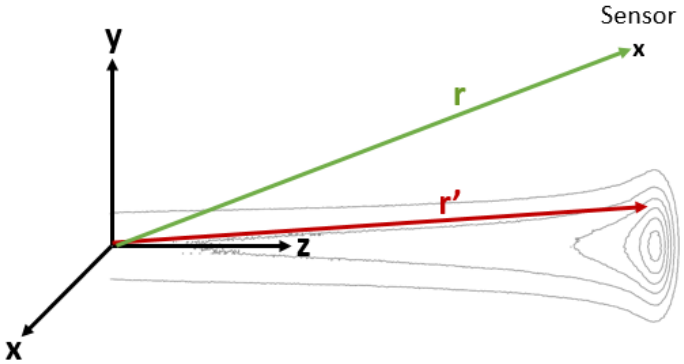

Figure 2.3: The grey contour is displaying the shape of the Bragg curve and the coordinate system is indicated by the black arrows. An arbitrarily positioned point sensor is indicated at **r** (green arrow) and an arbitrary point within the source is marked at **r'** (red arrow).

The acoustic wave generated at point **r'** at time t' propagates to the detector at **r**, where it is detected at time $t = t' + |\mathbf{r}\text{-}\mathbf{r'}|/v_s$. Since $v_{proton} >> v_s$ the dose deposition along the proton path is well approximated as instantaneously at time $t' = 0$ and the pressure wave at its detection point is detected at $t = |\mathbf{r}\text{-}\mathbf{r'}|/v_s$, where $|\mathbf{r}\text{-}\mathbf{r'}|$ is the distance from an arbitrary point of the source to the detector.

The heating function can be divided into a spatial and a temporal part, $H(\mathbf{r'},t') = H_s(\mathbf{r'})H_t(t')$, where, in a first step, the temporal part is assumed to be a delta-excitation $H_t(t') = \delta(t') = \delta\left(t - \frac{|\mathbf{r}-\mathbf{r'}|}{v_s}\right)$:

$$p(\mathbf{r},t) = \underbrace{\frac{\partial}{\partial t}\frac{\beta}{4\pi C_p}\iiint \frac{d\mathbf{r'}}{|\mathbf{r}-\mathbf{r'}|}H_s(\mathbf{r'})\delta\left(t - \frac{|\mathbf{r}-\mathbf{r'}|}{v_s}\right)}_{P_\delta(\mathbf{r},t)} \tag{2.12}$$

The spatial heating function $H_s(\mathbf{r'})$ is the energy density in units $[Jm^{-3}]$ and it is equal to $H_s(\mathbf{r'}) = \rho D(\mathbf{r'})$ and therefore directly proportional to the initial pressure $p_0 = \Gamma H_s(\mathbf{r'})$. $P_\delta(\mathbf{r},t)$ is therefore proportional to a volume integral over the dose, which scales indi-

rectly proportional to the distance from the source to the detector. To simplify $P_\delta(\mathbf{r},t)$ further, it is rewritten switching the coordinate system to the detector and using spherical coordinates, introducing also the coordinate $R = |r - r'|$, which is is just the radial coordinate in this coordinate system.

$$P_\delta(R,t) = \frac{\beta}{4\pi C_p} \int_0^{2\pi} d\phi \int_0^{\pi} d\theta \int_0^{\infty} dR \frac{1}{R} R^2 sin(\theta) \rho D(R,\theta,\phi) \delta\left(t - \frac{R}{v_s}\right) \tag{2.13}$$

Before the integration can be evaluated via the delta function, it must be written as a function of R. Using the translations and scaling property of the delta function, it can be written as $\delta(t - \frac{R}{v_s}) = \delta(\frac{1}{v_s}(v_s t - R)) = v_s \delta(R - v_s t)$. Now the delta function can be evaluated with the radial integration setting $R = v_s t$.

$$P_\delta(t) = \frac{\beta v_s}{4\pi C_p} \frac{1}{v_s t} \int_0^{2\pi} d\phi \int_0^{\pi} d\theta (v_s t)^2 sin(\theta) \rho D(R,\theta,\phi) \tag{2.14}$$

Here, the $1/(v_s t) = 1/R$ dependency denotes the decrease in amplitude with increasing distance to the detector, which is consistent with the inverse square law since the acoustic intensity drops off with the square of the amplitude and thus with $1/R^2$. The $(v_s t)^2 sin(\theta)$ term in the integral is the surface element originating from the change to spherical coordinates and $D(R,\theta,\phi)$ is the dose as seen from the detector where the radial component is described by $R = v_s t$. Equation 2.14 can further be simplified by reducing terms and making use of the initial pressure and the Grüneisen parameter Γ, respectively (cf. eqn. 2.8 and 2.9).

$$P_\delta(t) = \frac{t}{4\pi} \int_0^{2\pi} d\phi \int_0^{\pi} d\theta sin(\theta) p_0(R,\theta,\phi) \tag{2.15}$$

Conceptually, $P_\delta(t)$ can be understood as follows: All pressure contributions arising from the associated dose deposition at a distance $R = v_s t$ propagate to the detector. Pressure contributions, which originally have the same distance to the detector will arrive there simultaneously and overlap. Thus, $P_\delta(t^*)$ for a specific time t^* is given by the sum (integral) of all pressure contributions, which are originally located on a spherical shell with radius $R = v_s t^*$ with the detector being the centre of that sphere.

The location of the detector thus has a major influence on the signal shape as it determines, which pressure contributions arrive at the detector at the same time. Note, that

according to eqn. 2.12 the expected pressure at the detector for a temporal delta-shaped excitation is not given by $P_\delta(t)$ but its temporal derivative $p(t) = \frac{\partial P_\delta(t)}{\partial t}$, which is denoted as small $p_\delta(t)$.

2.2.3 Non-delta excitations in time

If non-delta excitations int time are considered, that is if the beam is turned on for a significant amount of time, the resulting pressure wave is obtained by convolution of the expected pressure for a delta-shaped excitation, $p_\delta(t)$, with the temporal heating function $H_t(t)$ [30, 51, 54, 58]. The temporal heating function $H_t(t) = \frac{I(t)}{\int I(t)dt}$ is the normalised beam current in units of $[s^{-1}]$. The convolution can be conceptually understood as a sum of infinitely many $p_\delta(t)$, which are weighted with the respective beam current given by $H_t(t)$. To obtain realistic results regarding the absolute pressure, the temporal heating function needs to be normalised $\int H_t(t)dt = 1$. Using the property of derivatives of convolutions, a very important identity is obtained:

$$p(t) = \frac{\partial P_\delta(t)}{\partial t} * H_t(t) = P_\delta(t) * \frac{\partial H_t(t)}{\partial t} \tag{2.16}$$

Both of these formulations are equally valid and are suitable for an intuitive understanding of the signal shape depending on the heating function used. For Gaussian proton pulses, the first formulation is helpful where the generic signal $\frac{\partial P_\delta(t)}{\partial t} = p_\delta(t)$ is smeared out in time by convolution with a Gaussian pulse. For rectangular pulses, the second formulation is useful. The derivative of the heating function decomposes into two delta pulses - one positive when the beam is switched on and one negative when it is switched off. The resulting pressure distribution is the sum of a positive $P_\delta(t)$ and a negative $P_\delta(t)$, separated in time by the pulse duration.

2.2.4 Detection sensor

The final component that has an influence on the amplitude and shape of the ionoacoustic signal is the recording sensor itself. These sensors often make use of piezoelectric materials which induce a voltage proportional to the amount of deformation acting on the

piezoelectric material. The ability of the sensor to produce voltage from a given input pressure is called sensitivity $[VPa^{-1}]$. Because of their ability to "transduce" pressure to voltage, the sensors or detectors are sometimes also called transducers.

Several properties of these transducers lead to effects that are responsible for an influence of the sensor on the signal shape. The entirety of these influences are summarised in the so-called total impulse response (TIR). The TIR is what the detector records when excited with a delta pulse. It can therefore by convolved with the result from equation 2.16 leading to the expected pressure to be recorded by the sensor:

$$p(t) = \frac{\partial P_\delta(t)}{\partial t} * H_t(t) * TIR(t) = P_\delta(t) * \frac{\partial H_t(t)}{\partial t} * TIR(t) \tag{2.17}$$

The TIR can be further decomposed into a spatial and an electrical component. The spatial component includes the geometry of the sensor. The non-negligible spatial extend of realistic detectors can be understood as multiple detectors arranged together each recording their individual signal. As their location relative to the source varies, the arrival time and to a lesser extend also the shape of these individual signals alter. When the final output signal is produced these individual signals are averaged leading to a low pass filtering effect on the recorded signal compared to what would be expected for an ideal point-like transducer. To counteract this effect, focused transducers can be used, that are designed for a certain distance from the source. These come with the disadvantage that misalignments lead to similar effects as discussed causing a distortion of the signal. The spatial impulse response therefore also includes setup specific components such as for example the angle between the transducer to the acoustic source.

The electrical impulse response describes the influence of the electrical components on the signal - first and foremost the central frequency and the bandwidth. The pressure sensitive materials used for detection are typically sensitive to a specific frequency range - also to suppress noise outside this frequency range. This electrical impulse response therefore acts as a band-pass filter that suppresses frequencies outside the sensitive band. Additional secondary electronics like amplifiers, filters or data recording systems can also be seen as part of the electrical impulse response of the whole system.

In practice, there is no clear distinction between spatial and electrical impulse response

since they can not be measured independently, and there are components that are difficult to assign to either category. For example, the intrinsic and surrounding materials of a sensor, depending on their composition, can cause reflections that are visible in the signal and therefore must be included in the total impulse response. The total impulse response is therefore an important factor in understanding the detected signal.

2.2.5 Thermo- and optoacoustics

The derivation of the acoustic signal with a heat induced source term and its four major contributions explained above is not limited to the generation by ions. The key formulas 2.10, 2.14 and 2.17 are valid for any kind of local energy and dose deposition. This is used in the photo- or optoacoustic effect. Here, instead of an ion beam, a pulsed laser is absorbed by a target, causing a confined energy deposition in the target. Analogous to the ionoacoustic effect, this energy deposition in turn launches an acoustic wave [54, 59, 60].

Using a suitable laser with a variable pulse structure, the influence of the temporal heating function and the influence of the TIR can be studied in detail using an optoacoustic setup. However, the spatial heating function cannot be reproduced with the optoacoustic setup. While ions release their energy according to the Bragg curve (cf. sec. 2.1.2), the following absorption law applies to the uncharged photons in a homogeneous absorbing medium:

$$I(z) = I_0 e^{-\mu z} \tag{2.18}$$

Here z is the penetration depth and μ is a material and photon energy dependent constant. The exponential decay of the intensity I is thus the biggest difference to ions and prevents a complete imitation of the ionoacoustic signal with a laser.

2.3 Ultrasonic probes

As mentioned in section 1.5, imaging of the irradiated medium is essential for the localisation of the Bragg peak relative to the tumour or surrounding organs. In this work, this relative localisation was achieved by the integration of the range information in an

ultrasound image. An ultrasound image is especially well suited for combination with ionoacoustics, since they are both based on the propagation of sound waves.

2.3.1 Principle of operation

An ultrasound probe typically consists of a planar or convex sensitive surface constructed of up to several hundred piezoelectric sensors [61]. In many respects, these sensors are similar to ionoacoustic sensors as described above in the context of the TIR. The main difference is the central frequency, which for ultrasound is between $2MHz - 20MHz$ and for ionoacoustic sensors, which are suitable for the detection of ionoacoustic signals at clinically used beam energies, is more in the range of $20kHz - 200kHz$. Another difference is that the transducers in the ultrasonic head act not only as receivers but also as transmitters. By applying a voltage, the transducers are excited by the reverse piezoelectric effect to transmit a sound wave. This sound pulse typically comprises 2-3 oscillation periods and thus has a duration that is typically in the range of $0.1\,\mu s - 1.5\,\mu s$ [61]. After the sound pulse has been emitted, it is partially reflected at the interfaces in the medium and detected again by the same transducer. The distance to the interface is determined by the time of flight (ToF), which is the time it takes for the ultrasonic wave to travel twice the distance to the reflective interface.

$$ToF = \frac{2r}{v_{US}} \tag{2.19}$$

Here r is the distance to the interface and v_{US} is the speed of sound. Typically an ultrasound probe is operated in the so-called B-mode or brightness mode, forming a 2D image where one dimension is depth and the other one is lateral extend. The brightness is determined by the amplitude of the reflected signal. For the image generation, ultrasonic probes assume a constant speed of sound which is typically $v_{US} = 1540ms^{-1}$. The image is thus stretched or compressed depending on whether the actual speed of sound in the traversed medium is larger or smaller than the one assumed.

The sequence and timing of the excitation of the various sensors is unique to the used ultrasound probe. For state of the art ultrasound probes, not only one sensor at a time, but several or all sensors are excited simultaneously or slightly delayed [61]. The specific

principle of operation ultimately determines the lateral and axial resolution. Statements about these quantities are therefore difficult. The lateral resolution varies depending on the depth at which it is to be determined and on the focus of the ultrasonic device, which can be set using acoustic lenses. Nonetheless, lateral resolution is typically not better than $2\,mm$. The axial resolution, however, is mostly dependent on the pulse duration, or more precisely, its spatial extend. If the reflections of two close by interfaces overlap significantly, these two interfaces cannot be distinguished anymore. In particular the axial resolution is given in [61] as:

$$\Delta z = \frac{N\lambda}{2} = \frac{N v_s}{2f} \tag{2.20}$$

Here, N is the number of cycles (typically 2-3), v_s the speed, λ the wavelength and f the used frequency of the sound wave. Axial resolution therefore improves with increasing frequency. For a $5\,MHz$ ultrasound system, the axial resolution in water is therefore approximately $400\,\mu m$. However, the increasing axial resolution with frequency is accompanied with a decreasing penetration depth, which will be discussed in more detail in the next section.

2.3.2 Acoustic propagation in heterogeneous media

This section refers to both ultrasound and ionoacoustic signal propagation in inhomogeneous materials since the only difference between the two is the frequency. The main effects which determine the propagation of a sound wave in heterogeneous media are reflection and attenuation which will be discussed below.

Reflections

When a sound wave impinges perpendicularly on a boundary layer, part of the sound wave is reflected and part is transmitted, depending on the media involved. These proportions can be calculated for the far-field approximation by the following formula [62]:

$$R = \frac{Z_2 - Z_1}{Z_2 + Z_1} \quad T = \frac{2Z_2}{Z_2 + Z_1} \tag{2.21}$$

Here, the acoustic wave travels from medium 1 into medium 2, R and T are the reflected and transmitted part of the incoming pressure amplitude and $Z = \rho v_s$ is the acoustic impedance. For example, approximately -2.1% is reflected at the interface between water and fat, -99.9% at the interface between water and air, and 61.1% at the interface between water and bone. The negative sign indicates a phase change of the reflected wave. The transmitted pressure on the interface between water and bone is $T = 161.1\%$ and thus the transmitted pressure is higher than the incident pressure. The conservation of energy is not violated here, because the acoustic energy does not depend exclusively on the pressure, but is also indirectly proportional on the acoustic impedance [62], which is significantly greater in bone.

The approximation in formula 2.21 fails if the incident direction of the boundary layer is not perpendicular, or if the lateral or longitudinal dimensions of the secondary material approach the value of the wavelength, which is approximately $\lambda = 3\,cm$ for ionoacoustic signals with $50\,kHz$ central frequency. For a non-perpendicular incident, refraction effects similar as in optics occur, which influence the direction as well as the reflection and transmission coefficient of the acoustic wave. In the case of a longitudinal expansion of the second material in the range of a few wavelengths, standing waves can form and interferences occur, which can also strongly change the transmission and reflection coefficients. For small lateral expansion of the second material, diffraction or scattering effects occur, deflecting the wave into the geometric shadow area of the obstacle.

Attenuation and dispersion

During the propagation of an acoustic wave, attenuation occurs where acoustic energy is converted into heat [63]. For most visco-elastic materials, such as soft tissues, the total acoustic attenuation can be described by the following equation [64]:

$$p(x) = p_0 e^{-\alpha f^{\eta} x} \tag{2.22}$$

Here α is a material specific quantity ($\alpha = 22 \times 10^{-17} s^2 cm^{-1}$ for water [65]), f is the frequency and x is the propagation distance. For soft tissues, the exponent η is between 0 and 2 [64]. Higher frequencies are therefore stronger attenuated than lower frequencies,

which is the reason why the penetration depth of an ultrasound device reduces with increasing frequency [66].

A topic that is closely related to attenuation is dispersion. Dispersion is well known from optics and describes the phenomenon where the speed, in acoustics the speed of sound, is a function of frequency. For ionoacoustics, dispersion is a crucial quantity, since here a high-frequency ultrasound device ($3\,MHz - 5\,MHz$) is combined with a low-frequency ionoacoustic signal ($20\,kHz - 200\,kHz$). This phenomenon is caused, at least in part, by the frequency-dependent attenuation, whose relationship to dispersion is described by the Kramers-Kronig relationship [67]. For water, dispersion measurements were performed in the frequency range from $500\,kHz$ to $25\,MHz$ and no significant dispersion was detected [68, 69]. As an approximation for soft tissue, dispersion is often measured in haemoglobin solutions. An overview of the different concentrations and frequency ranges investigated is given in Treeby et al. [70]. In none of the cited papers therein frequencies below $200\,kHz$ are investigated, however the paper itself claims measurements of the dispersion between $0\,Hz$ and $70\,MHz$. The measured dispersion is below $1\,ms^{-1}$ in the frequency range between $0\,Hz$ and $5\,MHz$ for all investigated haemoglobin solutions up to $20\,g\,dL^{-1}$ [70]. The speed of sound difference between the low-frequency ionoacoustic signal and the high frequency ultrasound signal is thus $< 1\,ms^{-1}$. As the speed of sound in the human body is approximately $1500 ms^{-1}$ this uncertainty only accounts for less than 1‰. This dispersion is thus negligible for ionoacoustics, since the uncertainty in the speed of sound of 1‰ translates directly to a range uncertainty of 1‰.

2.4 Signal processing

The goal of signal post-processing is to increase the signal-to-noise ratio (*SNR*) in order visualise signals, which would not be detectable due to the high noise level. The *SNR* of a signal is typically defined as the ratio of average signal power to average noise power.

$$SNR = \frac{average\ \ signal\ \ power}{average\ \ noise\ \ power} \tag{2.23}$$

According to Parseval's theorem [71] the average power of a signal $x(t)$ can calculated equally in time domain or in frequency domain using the Fourier transform of the signal $\mathcal{F}(x(t)) = \widetilde{x}(f)$:

$$P = \lim_{T\to\infty} \frac{1}{T} \int_0^T |x(t)|^2 dt = \lim_{T\to\infty} \frac{1}{T} \int_{-\infty}^{\infty} |\widetilde{x}(f)|^2 df \tag{2.24}$$

The right side of the equation contains a very important quantity namely the power spectral density of the signal.

$$\rho_x = \lim_{T\to\infty} \frac{1}{T} |\widetilde{x}(f)|^2 \tag{2.25}$$

The power spectral density describes the power per unit bandwidth in units $[\frac{W}{Hz}]$. The integration over all frequencies thus yields the total power of the signal. For its practical calculation the Wiener–Khinchin theorem [72] can be used, which states that the power spectral density is given by the Fourier transform of the autocorrelation function of the signal. For white noise, for example, the autocorrelation function is a delta-function and the corresponding power spectral density is thus constant.

In contrast to the average power of a signal, where the considered duration T should be as large as possible in order to obtain accurate values, an instantaneous power is more meaningful for signals of short duration. This is defined for a specific time t^* as:

$$P = \lim_{T\to 0} \frac{1}{T} \int_{t^*-\frac{T}{2}}^{t^*+\frac{T}{2}} |x(t^*)|^2 dt = |x(t^*)|^2 \tag{2.26}$$

2.4.1 Filtering

An important component in signal processing in order to increase the *SNR* is the use of analogue or digital filters. In the following, SNR_M describes the *SNR* of the raw, unfiltered measurement, while SNR_C is used to describe the *SNR* of the filtered function. Mathematically, a filter is applied to a measurement by convolution with a filter function $F(t)$.

$$C(\tau) = \int_{-\infty}^{\infty} M(t) F(\tau - t) dt \tag{2.27}$$

Here, $C(\tau)$ is the filtered signal, $M(t)$ is the measurement and $F(t)$ is the filter. Further, τ describes a time shift between the measurement and the filter. Since $C(\tau)$ and $M(t)$

are of the same units, the filter function $F(t)$ is of units $[\frac{1}{s}]$. Such filters are often low, high or band-pass filters, which is why the representation is often chosen in the frequency domain.

$$\widetilde{C}(f) = \widetilde{M}(f)\widetilde{F}(f) \tag{2.28}$$

Where $\widetilde{C}(f)$, $\widetilde{M}(f)$ and $\widetilde{M}(f)$ are the Fourier transforms of $C(\tau)$, $M(t)$ and $F(t)$, respectively.

The following derivation is based on Turin et al. [73] and was adapted to the case of ionoacoustic measurements. Assuming a measurement of duration d was recorded that consists of white noise $N(t)$ and a signal $S(t)$. The goal of the derivation is to find a filter $F(t)$, which maximises the SNR_C (cf. eqn. 2.23). For a filter of arbitrary shape the output of the filter reads:

$$C(\tau) = \int_0^d (N(t)+S(t))F(\tau-t)dt = \underbrace{\int_0^d N(t)F(\tau-t)dt}_{\text{noise part } C_N(\tau)} + \underbrace{\int_0^d S(t)F(\tau-t)dt}_{\text{signal part } C_S(\tau)} \tag{2.29}$$

Equation 2.29 shows that the filtered signal $C(\tau)$ can be described by the filter acting on the noise part ($C_N(\tau)$) and the signal part ($C_S(\tau)$) independently. In the following the power of the signal part and the noise part will be deduced separately and subsequently used to calculate a general expression for the resulting SNR_C of the filtered signal, which can be maximised. Using the convolution theorem, the noise part can be expressed in frequency domain:

$$\widetilde{C}_N(f) = \widetilde{N}(f)\widetilde{F}(f) \tag{2.30}$$

With equation 2.25 the corresponding power spectral density can be expressed as:

$$\rho_{C_N} = \lim_{T\to\infty} \frac{1}{T}|\widetilde{C}(f)|^2 = \underbrace{\lim_{T\to\infty} \frac{1}{T}|\widetilde{N}(f)|^2}_{N_0} |\widetilde{F}(f)|^2 \tag{2.31}$$

The right hand side contains the power spectral density of white noise, which is known to be constant and is defined to be N_0. The total power contained the noise part of the

filtered signal is given by the integration over all frequencies:

$$P_{C_N} = N_0 \int_{-\infty}^{\infty} |\widetilde{F}(f)|^2 df \tag{2.32}$$

Note that $P_{C_N} < \infty$ holds as long as the frequency spectrum of the filter function is limited. Regarding the signal part of equation 2.29 a different approach is pursued, since the power spectral density can not be used as there is no information on the frequency content of the filter function or the signal. Instead, the signal is transformed to the frequency domain and subsequently back transformed to time domain. The goal is to achieve a description in time domain in dependency of the signal and the filter function in frequency domain.

$$\begin{aligned} \widetilde{C}_S(f) &= \widetilde{S}(f)\widetilde{F}(f) \\ C_S(\tau') &= \int_{-\infty}^{\infty} \widetilde{S}(f)\widetilde{F}(f)e^{i\omega\tau'} df \end{aligned}$$

Here, the back transformation in the second line is performed for a particular but arbitrary time τ' and $\omega = 2\pi f$ is used. The instantaneous power at this particular time τ' is given according to eqn. 2.26.

$$P_{C_S} = |C_S(\tau')|^2 = \left(\int_{-\infty}^{\infty} \widetilde{S}(f)\widetilde{F}(f)e^{i\omega\tau'} df \right)^2 \tag{2.33}$$

The reduction of the average power to the instantaneous power means conceptually that a filter is searched, which for a certain time τ' maximises the ratio between the maximum power in the filtered signal P_{C_S} and the its average noise power P_{C_N}. This reduction to the instantaneous power can be justified, since for short time intervals the average power converges to the instantaneous power. Combining equation 2.33 and 2.32 the SNR_C of the filtered signal can be written as:

$$SNR_C = \frac{P_{C_S}}{P_{C_N}} = \frac{\left(\int_{-\infty}^{\infty} \widetilde{S}(f)\widetilde{F}(f)e^{i\omega\tau'} df \right)^2}{N_0 \int_{-\infty}^{\infty} |\widetilde{F}(f)|^2 df} \tag{2.34}$$

The expression for the SNR_C is subsequently is maximised using the Schwarz inequality, where the bar denotes the complex conjugate:

$$\left|\int f(x)\overline{g(x)}dx\right|^2 \leq \int |f(x)|^2 dx \int |g(x)|^2 dx \tag{2.35}$$

Applying eqn. 2.35 to the numerator of eqn. 2.34, where $f(x)$ is associated with $\widetilde{S}(f)e^{i\omega\tau'}$ and $\overline{g(x)}$ with $\widetilde{F}(f)$ the SNR_C can be simplified to:

$$SNR_C \leq \frac{1}{N_0}\int_{-\infty}^{\infty} |\widetilde{S}(f)|^2 df \equiv \frac{E}{N_0} \tag{2.36}$$

The integrand in equation 2.36 is called the energy density of the signal. The integration over all frequencies thus yields the total energy contained in the signal which determines the maximum possible SNR_C of the filtered signal. Note, that this equation does not make any statement about the SNR enhancement enhancement by the filter. Depending on how the energy is distributed within the signal, the SNR_M of the original signal can vary drastically, while the SNR_C is only dependent on the total signal energy.
Inspecting eqn. 2.35 in more detail it can be seen that the equality sign only holds if $f(x) = kg(x)$ with an arbitrary constant k. The SNR_C is thus maximised if:

$$\widetilde{F}(f) = \overline{k\widetilde{S}(f)e^{i\omega\tau'}} = k\overline{\widetilde{S}(f)}e^{-i\omega\tau'} \tag{2.37}$$

Inserting the Fourier transform of $\widetilde{S}(f)$ and using that $S(t)$ is real:

$$\widetilde{F}(f) = ke^{-i\omega\tau'}\overline{\int_{-\infty}^{\infty} S(t)e^{-i\omega t}dt} = k\int_{-\infty}^{\infty} S(t)e^{i\omega(t-\tau')}dt \tag{2.38}$$

Now a new shifted time is introduced as $t_s = \tau' - t$. The integration can be carried out over t_s instead of t since the additional constant can be incorporated into k.

$$\widetilde{F}(f) = k\int_{-\infty}^{\infty} S(\tau' - t_s)e^{-i\omega t_s}dt_s = \mathcal{F}\underbrace{(kS(\tau' - t_s))}_{F(t_s)} \tag{2.39}$$

where now the shape of the filter can be determined as:

$$F(t_s) = kS(\tau' - t_s) \tag{2.40}$$

A back transformation to restore the dependence on t shows the final form of the filter:

$$F(\tau' - t) = kS(t) \Leftrightarrow F(t) = kS(\tau' - t) \tag{2.41}$$

This is the filter, which maximises the SNR_C. The two formulations are equivalent, stating that the filter takes the shape of the time inverted signal (formulation 2) or vice versa (formulation 1). The arbitrary constants state that the filter can be scaled in amplitude (k) and shifted in time (τ'). Note that τ' was introduced as the particular time at which the filtered function maximises it instantaneous power. This means that shifting the filter in time will correspondingly shift the filtered function in time. The time inversion states that the filter is mirrored in time relative to the signal. However, if this filter is subsequently applied by convolution (cf. eqn. 2.27), the time component is flipped again and filter and signal are of equal shape.

Applying such a filter by convolution works, however it seems unnecessary to find a filter which is mirrored relative to the signal just so that it can be mirrored again, when applied by convolution. Instead, a correlation filter can be used yielding the same result. For a correlation filter the filter takes the form $F(t) = kS(t + \tau')$ and is applied not by convolution but by correlation:

$$C(\tau) = \int_{-\infty}^{\infty} M(t)F(t + \tau)dt \tag{2.42}$$

For a correlation the filter is thus not flipped neither before nor during application. The filter ideally mimics the shape of the signal as accurately as possible. The resulting function of a correlation filter is call a correlation function and is often called a measure of similarity as it maximises when the maximum similarity between the measurement and the filter is reached indicating the signal position in the measurement.

2.4.2 Averaging

In addition to filtering, signal averaging is used in almost all experimental investigations to increase the *SNR*. Under the assumption of white noise, coherent averaging of n signals increases the ratio of signal amplitude to average noise amplitude by a factor of $\sqrt{n}$. Averaging thus causes a linear increase of the *SNR* with the number of measurements taken into account.

The factor $\sqrt{n}$ can be understood by considering signal averaging and noise averaging separately. When n signals are averaged, the signal amplitude remains unchanged provided that each signal has the same amplitude and that the signal position is the same in each of the measurements. When averaging the noise, stochastic processes must be taken into account, since the noise values are randomly distributed. The addition of random numbers symmetrically distributed around 0 is described by the symmetric random walk [74]. The average distance (average noise floor) from 0 after n additions is proportional to $\sqrt{n}$. The n-fold averaging of noise therefore leads to a reduction of the noise amplitude by the factor $\sqrt{n}/n$. Since the noise is reduced by that factor the relative amplitude between the unchanged signal and the noise is increasing with the reciprocal of that factor and is therefore proportional to $\sqrt{n}$.

Chapter 3

SNR optimisation of ionoacoustic signals

The content of this chapter is largely based on the publication by the author of the thesis [75], which was published in Frontiers in Oncology. The experiments with regard to ionoacoustic *SNR* optimisation were performed at the pre-clinical tandem accelerator installed at the MLL using $20\,MeV$ protons impinging on a water phantom. The experiments primarily served to gain a better understanding of the signal structure and quality. The main task was to optimise the signal quality by clever choice of beam parameters and post-processing tools so that it could be used at clinical doses for range evaluation. The results obtained could then be extrapolated to the application on clinical accelerators.

3.1 Materials and Methods

3.1.1 Experimental setup

A sketch of the setup for the measurement of ionoacoustic signals as performed at the tandem accelerator at the MLL is shown in figure 3.1 After the generation and pre-acceleration of negatively charged hydrogen ions H^-, they pass a chopper. Here, the original CW beam can be arbitrarily chopped with a lower limit for the pulse duration being $40\,ns$. The chopper was externally controlled by a function generator (Agilent 33220A) to generate pulse durations between $40\,ns - 1\,\mu s$ at a repetition frequency of $10\,kHz$. In the tandem accelerator, the negatively charged hydrogen ions are converted to protons when passing a stripper foil at a terminal voltage of $10\,MV$ (cf. sec. 2.1.1). Thus the protons have gained a total of $20\,MeV$ at the output of the accelerator. In the 90° magnet, the protons are deflected and energy-selected. The total energy spread of the beam is about $\frac{\Delta E}{E} \approx 10^{-5}$. Before the beam leaves the vacuum tube through a $11.4\,\mu m$ thick titanium foil, the beam size was reduced by a slit system to a nearly rectangular

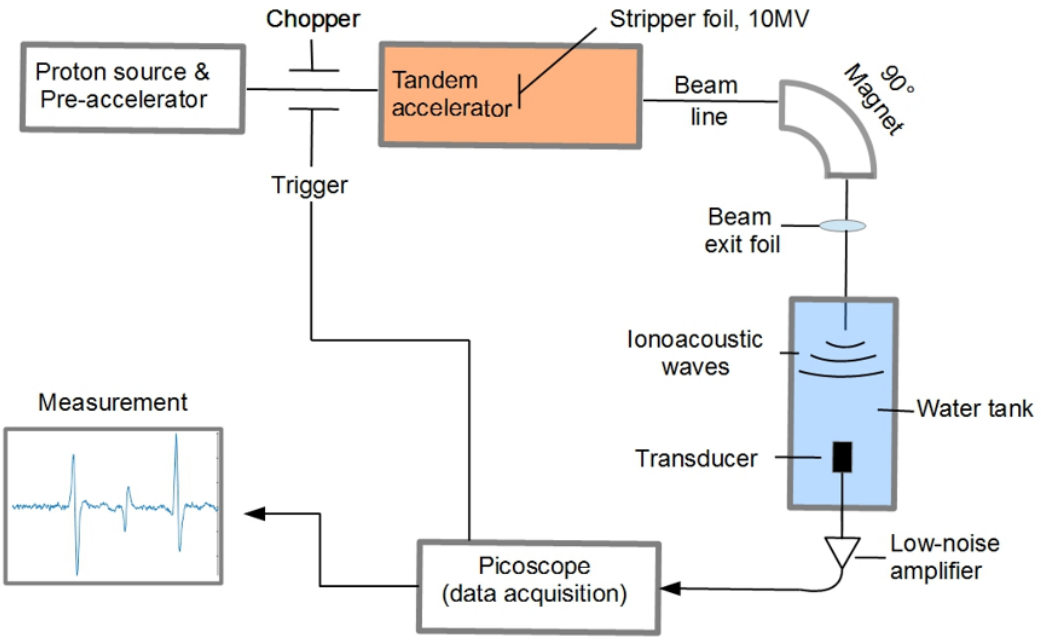

Figure 3.1: Experimental setup at the tandem accelerator in Garching for detection of ionoacoustic waves using $20\,MeV$ protons in a water tank phantom. Figure based on Schauer et al. [75].

lateral beam profile with dimensions $2.5\,mm \times 3.0\,mm$. The beam current could be freely chosen by the operators and in particular was adjusted between $0.65\,\mu A$ and $4.50\,\mu A$. Here, the instantaneous beam current is given, i.e. the average beam current in the pulse, which is independent of the repetition frequency or pulse duration. Since the pulses from the chopper are generated by a deflection of the beam, the resulting pulses are close to rectangular in shape. The pulse shape at the exit window was measured using a fast silicon detector [76] using a nominal pulse duration of $200\,ns$. The result is shown in figure 3.2. The measurement in the beam current profile shows small deviations from an ideal rectangular pulse shape in the rise and fall times (from 10% to 90% $\approx 15\,ns$) and in the plateau region. The total deviation of the actual pulse duration ($FWHM \approx 193\,ns$) from the nominal pulse duration is small and the approximation of a rectangular pulse is justified.

The ionoacoustic signals were generated in a water tank ($33 \times 18 \times 19\,cm^3$) filled with

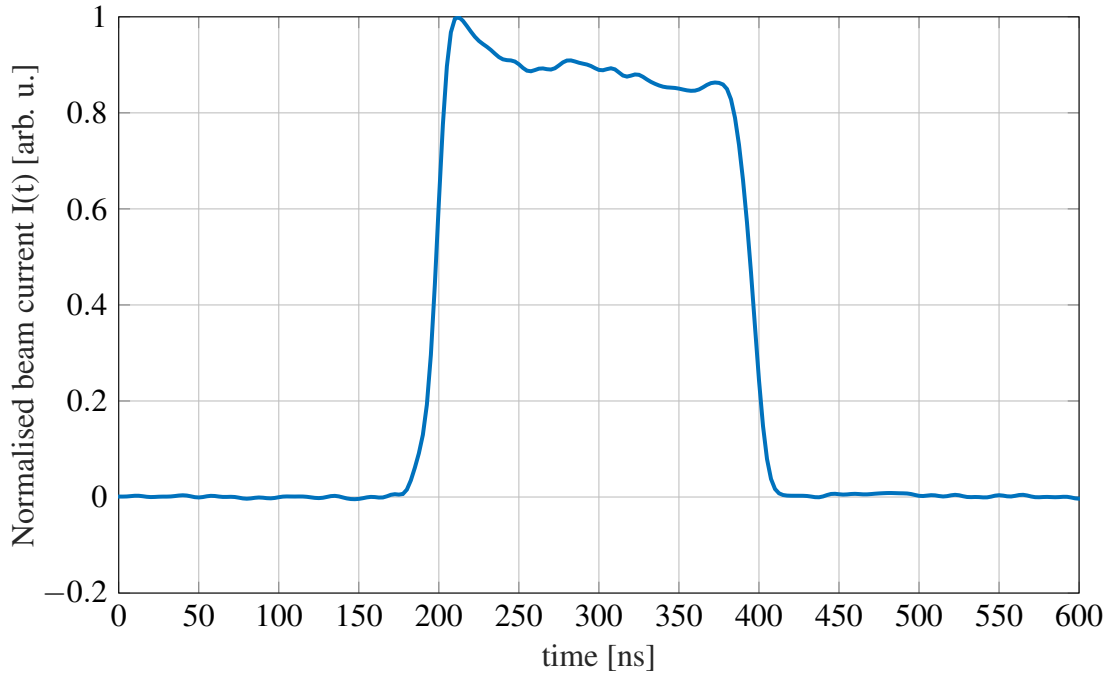

Figure 3.2: Beam current measured at the exit window at the location of the experimental setup for a nominal pulse duration of 200 ns. Figure adopted from Schauer et al. [75].

deionised water at room temperature. The water temperature was recorded with each measurement to accurately determine the speed of sound of the water retrospectively. The expected range of the 20 MeV protons in water according to Monte Carlo simulations (cf Sec. 3.1.2) is 4.21 mm. The ionoacoustic signals were recorded with an Olympus immersion transducer (V382-SU) mounted on a motorised x-y-z-stage. The transducer was positioned in axial configuration distal to the Bragg peak. It has a diameter of 12.7 mm and is spherically focused to one inch (25.4 mm), which ideally corresponds to its axial distance to the Bragg peak. It has a central frequency of 3.5 MHz with a $-6\,dB$ bandwidth of 72% between 2.2 MHz and 4.7 MHz. The transducer was iteratively aligned in both lateral and axial positions. For this purpose, ionoacoustic signals were recorded in scans along the three spatial axes in 1 mm steps and the position of maximum amplitude was selected.

The ionoacoustic signals were first amplified with using a 60 dB low-noise amplifier (LNA, type: HVA-10M-60-B, FEMTO), before being digitised in a 6404D Picoscope

at a sampling rate of $156\,MS/s$. The Picoscope was triggered with the same signal that was sent to the chopper for pulse generation. The $10\,kHz$ repetition frequency of the chopper allowed a consecutive measurement of 1000 ionoacoustic signals within $100\,ms$. These individual signals could be used in post-processing for averaging, which ultimately determined the dose which was applied to the water phantom.

3.1.2 Correlation filter

To increase the *SNR* of the ionoacoustic signals, multiple signals were averaged and subsequently filtered with a correlation filter (cf. sec. 2.4.1) using MATLAB [77]. The correlation filter takes as input the measurement $M(t)$ and a template $F(t)$, which ideally corresponds to the noise-free ionoacoustic signal. The correlation filter is mathematically designed to maximise the *SNR* of the input signal. The filtered signal $C(M,T)$, also called correlation function states for discretised input signals:

$$C_{M,F}(\tau) = \frac{\Sigma_t M(t) \cdot F(t+\tau)}{\sqrt{AC_{M,M}(0) \cdot AC_{F,F}(0)}} \tag{3.1}$$

The denominator in equation 3.1 is composed of the autocorrelation function *AC* of measurement and template at zero lag, respectively. It acts as a normalisation ensure correlation coefficients between -1 to 1. The correlation function depends on the variable τ, which describes the time shift between measurement and template. The relative position of the template to the measurement is changed incrementally and for each relative position, a correlation value (also correlation coefficient) is calculated. This correlation coefficient maximises at the correlation peak when the template perfectly overlaps with the signal in the measurement. The position of the correlation peak provides the information where in the measurement the signal is located.

The templates were simulated using the theoretical description of signal generation (cf. sec. 2.2) and can in particular be expressed as:

$$F(t) = P_\delta(t) * \frac{\partial H_t(t)}{\partial t} * TIR \tag{3.2}$$

. Here $P_\delta(t)$ is proportional to a spherical integral over the dose deposition as seen from the coordinate system of the detector, $H_t(t)$ is the pulse shape (normalised beam current) provided by the accelerator and TIR is the impulse response of the detector. The generation of the templates can be divided into three steps, namely the initial pressure derivation, its propagation and its detection.

Initial pressure derivation

In order to derive the initial pressure $p_0 = \Gamma\rho D$, the Grüneisen parameter Γ, describing the conversion from heat to pressure, the mass density ρ and the dose deposited by the proton beam D must be determined. The 3D dose distributions of the proton beams were generated using FLUKA [78], a Monte Carlo simulation program. Using the beam parameters of the $20\,MeV$ proton beam, FLUKA allows for an accurate simulation of its 3D dose distribution. The dose was scored using a cartesian scoring of $20\,\mu m$ voxel size. The number of particles used in the simulation was calculated from the beam current and the repetition frequency and is 1.6×10^6. However, for the use of dose distributions in the context of template generation, the number of particles plays a subordinate role. As long as enough particles are used to produce a smooth dose distribution, the exact number of particles only affects the amplitude of the template, which has no influence on the SNR_C of the resulting correlation function.

From this 3D dose distribution, the initial pressure distribution can be calculated by voxel-wise multiplication with the Grüneisen parameter and the mass density (cf. sec. 2.2.1). An overview of the most commonly used material properties are shown in table 3.1. The

	Water ($20°C$)	Air	PMMA	Kapton
Grüneisen parameter Γ	0.11	0.6	0.3	1.5
Mass density $\rho[kgm^{-3}]$	998	1.2	1170	1420
Speed of sound $v_s[ms^{-1}]$	1482	342	2757	2400

Table 3.1: Material specific parameters needed for the calculation of the initial pressure.

Grüneisen parameters shown in table 3.1 are values from the literature (water [48], air [79], PMMA [80], Kapton [81]). It is important to state that these values are temperature dependent and there is a lack of systematic studies regarding the Grüneisen parameter. However, in the context of the generation of the templates the actual value of the

Grüneisen parameter is not of great importance as long as it is constant in the region of interest at the Bragg peak. Again, it only affects the amplitude of the template, which does not contribute to the SNR_C of the correlation function. Note that despite the relatively high Grüneisen parameter in air, the pressure generation there is practically negligible due to the low mass density.

Pressure propagation using k-wave

In the next step, the initial pressure is processed further with the help of k-wave [31, 82]. K-wave is a MATLAB toolbox for the propagation and detection of acoustic waves. In k-wave, a 3D grid is defined, which matches the grid from the dose simulation or which is matched by interpolation. In addition, for each voxel in k-wave, a speed of sound and a mass density are given (cf. table 3.1).
One or more voxels in the k-wave grid can be defined as a sensor. For the templates used in this work, the sensor implemented in k-wave was assumed to be ideal (broadband) and point-like positioned in the axial direction at the distal end of the Bragg peak. The detector characteristics were then taken into account in a proceeding step. The distance from the sensor to the Bragg peak was adapted to the experimental conditions ($25.4\,mm$). This distance determines the curvature of the spherical shell over which the pressure is integrated and can thus (especially at small distances) change the signal shape. The resulting pressure assuming a delta-shaped contribution from the heating function and an ideal point transducer yields $P_\delta(t)$. It was subsequently convolved with the derivative of the temporal heating function (cf. eqn. 2.16), which is rectangular and of variable duration to create a generic signal, which does not take into account the detector response.

Detector characteristics

To generate the final expected pressure distribution and thus the templates (cf. eqn. 3.2), the transfer function of the detector (TIR) is considered in the last step. For the Olympus immersion transducer, the transfer function was approximated by a band-pass filter (Butterworth filter of first order). This band-pass filter accounts for both spatial and electrical impulse response and its boundaries ($800\,kHz - 3.0\,MHz$) were iteratively determined such that the simulation best matches the measured signals.

Generalisation

In some simulations, simplifications have been made to make more general statements that do not depend on the sensor or measurement setup used. In particular, in some simulations the influence of the detector response function (TIR) was neglected, which corresponds to a detector with infinite bandwidth and frequency-independent, constant sensitivity. In addition, the distance between the Bragg peak and the sensor was chosen to be 'large', which means that the spherical shell in the integration from equation 2.14 is flat in the region of the dose distribution. Finally, in some simulations, monoenergetic proton beams were used instead of proton beams with a realistic energy spread. These changes will be explicitly mentioned, when the corresponding simulations are shown.

3.1.3 SNR assignment

To quantify the quality of a measurement, each measurement was assigned an *SNR*. The *SNR* is defined as the average signal power divided by the average noise power.

$$SNR = \frac{\bar{P}_s}{\bar{P}_n} = \frac{\frac{1}{N}\sum_{n=1}^{N} A_s^2(n)}{\frac{1}{M}\sum_{m=1}^{M} A_n^2(m)} \tag{3.3}$$

Where $A_s(n)$ and $A_n(m)$ are the amplitudes of the signal and noise respectively, $n = 1 \cdots N$ are all samples considered for the calculation of the signal power and $m = 1 \cdots M$ are all samples considered for the calculation of the noise power. To exclude reflections or secondary signals from the calculation of the noise power, the range of the noise was defined before the arrival of the first signal.

In the cases where it is not about the absolute *SNR* of a measurement or a correlation function, but about a relative *SNR* comparison between two measurements, an independent noise measurement was used as the noise power basis for both measurements in comparison, to exclude external noise sources which might be different for two different measurements. In the following, SNR_M is used when referring to the *SNR* of the raw measurements while SNR_C is used when referring to the *SNR* of the correlation functions.

3.2 Results

3.2.1 Signal shape derivation

In the following, the expected signal shape for the experiments on the preclinical tandem accelerator is derived. The composition of the signal is divided into a spatial component, a temporal component and a detector component.

Measurement position

All measurements shown and evaluated in this thesis were conducted with a single detector in axial measurement position distal to the Bragg peak. This measurement position is advantageous compared to a lateral or otherwise located measuring position regarding a range verification of the proton beam. In an axial measurement position, a change in the arrival time of the acoustic signal corresponds directly to a change in the range of the proton beam. In a lateral measurement configuration, a change of the range will in contrast not change the arrival time but alter the shape of the signal, which is significantly more difficult to associate with the range of the protons.
Another advantage in an axial measurement configuration is the fact that the first arriving signal is predominantly generated from the Bragg peak which is the region of interest. In contrast to signals measured in other measurement locations, a signal measured in axial position is expected to be free from interferences of secondary signals or echoes, which makes it most easily predictable and interpretable. The time of flight of the signal generated at the Bragg peak is also very robust against misalignments of the detector in the lateral direction. A simple consideration using the Pythagorean theorem shows that a lateral misalignment of the detector of $2\,mm$ at a distance of $5\,cm$ between the Bragg peak and the detector will only increase the time of flight by $27\,ns$, changing the associated range by $40\,\mu m$.

Spatial component

The understanding of the spatial component $P_\delta(t)$ contributing to the signal shape in the axial measurement configuration is essential for the further course of this thesis. $P_\delta(t)$

is the pressure that would be detected if the temporal derivative of the temporal heating function and the TIR would be delta-distributions. Fig. 3.3 illustrates a conceptional understanding of the origin of $P_\delta(t)$ for the described measurement setup at the tandem accelerator.

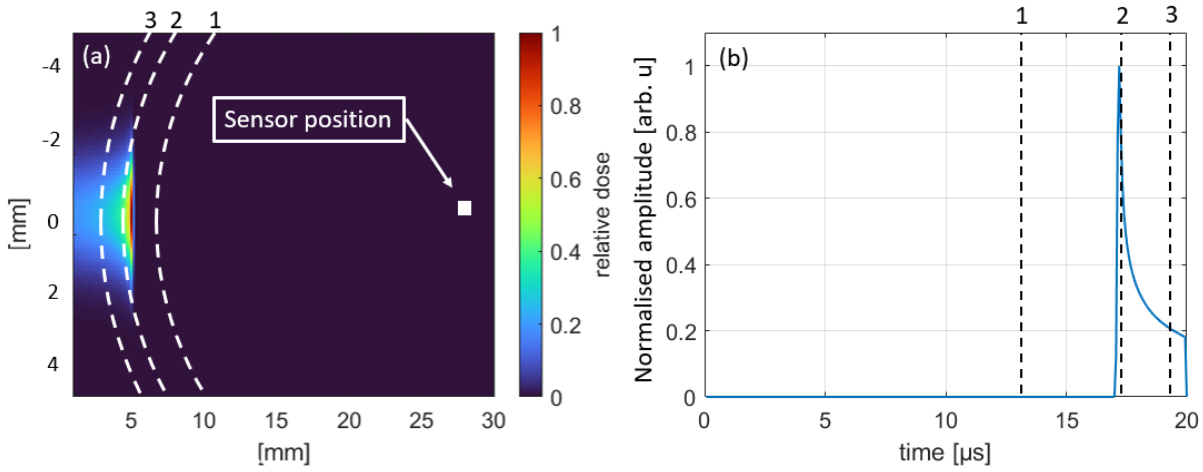

Figure 3.3: A two dimensional projection of the dose distribution of a $20\,MeV$ proton beam in water (colour coded) and a sensor position indicated by the white square mimicking the setup used at the preclinical tandem accelerator (a). The white dotted lines (1,2,3) indicate dose and thus pressure contributions that have an equal distance to the sensor and will thus arrive at the detector at the same time. The resulting time points (1,2,3) are marked in the time dependent pressure curve $P_\delta(t)$ in (b).

Panel (a) shows a two dimensional projection of the 3D dose simulation of the $20\,MeV$ proton beam in water. The relative dose is indicated by the colour bar on the right. In addition, the sensor position is indicated by the white square at approximately $25.4\,mm$ distal to the Bragg peak, which mimics the experimental setup with a point-like sensor. All dose contributions which lie on the surface of a particular sphere centred at the detector (white dashed lines) contribute to the initial pressure (according to $p_0 = \Gamma\rho D$), which is arriving at the detector at one particular time $t = \frac{R}{v_s}$, where R is the radius of that respective sphere and v_s the speed of sound of the medium (here $1.50\,mm\mu s^{-1}$). The three indicated spheres in panel (a) thus correspond to the pressure recorded at three different times marked in $P_\delta(t)$ in panel (b). The sphere with the smallest distance to the detector (1) includes all pressure contributions which arrive at the detector at $t = \frac{20\,mm}{1.5\,mm\mu s^{-1}} = 13.3\,\mu s$. As this sphere does not include any dose values, the corresponding pressure is zero which is shown in panel (b) since $P_\delta(13.3\,\mu s) = 0$. For the second closest sphere (2), the asso-

ciated pressure arrives at approximately 17.5 μs which is shortly behind the maximum of $P_\delta(t)$ and the last sphere (3) is responsible for the pressure arriving at 19 μs.
Depending on the lateral extend of the beam and the distance to the sensor, the shape of $P_\delta(t)$ can vary. For large distances between the beam and the detector and a small lateral extend of the beam, the sphere is essentially flat in the region of the dose distribution. In this approximation, $P_\delta(t)$ is just a flipped one dimensional Bragg curve, where the spatial axis of depth is transcribed to a time axis via $t = \frac{R}{v_s}$. In contrast, for short distances to the detector and a large beam diameter, the curvature of the spheres has a significant impact on the shape of $P_\delta(t)$.

Temporal component

The implementation of the temporal component in the signal structure is achieved by the convolution of $P_\delta(t)$ with the temporal derivative of the temporal heating function $\frac{\partial H_t}{\partial t}$: $p(t) = P_\delta(t) * \frac{\partial H_t(t)}{\partial t}$.
The temporal heating function is given by the normalised beam current $H_t(t) = \frac{I(t)}{\int I(t)dt}$, i.e. the pulse shape of the proton pulse. At the tandem accelerator, a chopper is used to cut the original CW proton beam into quasi-rectangular pulses of arbitrary duration (cf. Fig. 3.2). Simulations of the ionoacoustic signals expected according to equation 2.17 are shown in Fig. 3.4. For the simulations shown here, pulse durations between 50 ns and 1 μs were assumed and the total impulse response (TIR) of the sensor was neglected (i.e. delta-shaped). For rectangular pulses as shown in the simulations in Fig. 3.4, the derivative of the temporal heating function collapses into two delta-shaped peaks. A positive peak when the beam is switched on (compression) and a negative peak when the beam is switched off (rarefaction). The compression curve is identical with $P_\delta(t)$ discussed in Fig. 3.3 (b). The convolution of these two delta-peaks with $P_\delta(t)$ is illustrated as the sum of a positive $P_\delta(t)$ (blue) with a negative copy of $P_\delta(t)$ (red) shifted in time by the pulse duration. The resulting black curves represent ionoacoustic signals as they would be recorded for ideal detectors, i.e. by a point sensor with infinite bandwidth located 25.4 mm distal to the Bragg peak.
The signals follow the shape of the compression pulse until switching off the beam leads to destructive interference of the rarefaction curve with the compression curve. For short

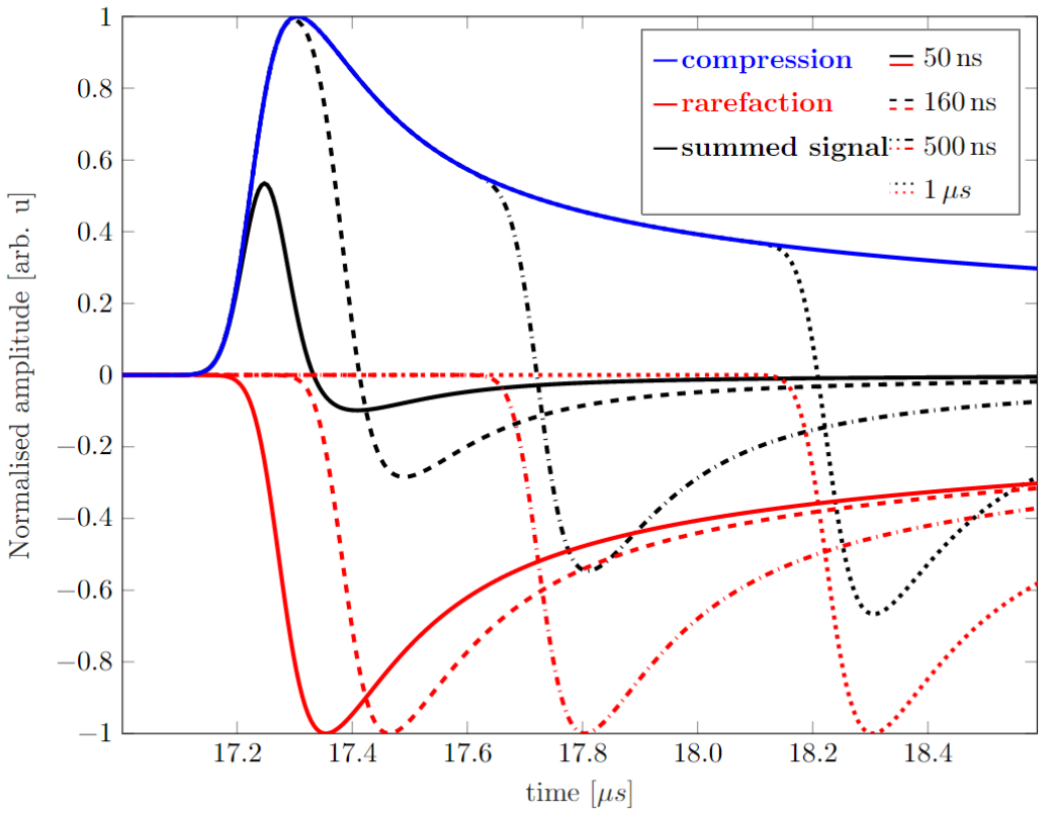

Figure 3.4: Ionoacoustic signals (black curves) as expected to be detected by an ideal point sensor located 25.4 *mm* distal to the Bragg peak for pulse durations of 50 *ns* (solid), 160 *ns* (dashed), 500 *ns* (dash-dotted) and 1 μs (dotted). All signals share the same compression curve (blue) and have individual rarefaction curves (red). The time difference between the compression and rarefaction curve is given by the pulse duration. Figure based on Schauer et al. [75].

pulse durations (50 *ns*, solid), the consequence is that this destructive interference reduces the maximum possible amplitude of the signal. For the next longer pulse duration (160 *ns*, dashed), the maximum pulse duration is just reached before the destructive interference reduces the signal amplitude. This characteristic duration is often referred to as stress-confinement [29, 49] and is dependent on the spatial extend of the Bragg peak in longitudinal direction, which is in turn dependent on the proton energy. Stress confinement is therefore longer, the higher the proton energy. For even longer pulse durations (500 *ns*, dash-dotted and 1 μs, dotted), the deposited dose continues to increase linearly with pulse duration, but the maximum signal amplitude no longer increases.

Detector component

In order to finalise the simulations in Fig. 3.4, the influence of the detector itself has to be taken into account. The detector characteristics were approximated here with a first-order Butterworth band-pass filter between $800\,kHz$ and $3\,MHz$. The filter limits were determined iteratively to maximise the similarity between measurement and simulation. The filter boundaries best describe the influence of the sensor on the acoustic signal and incorporate not only influences from the detector itself but also its position relative to the Bragg peak. The result after accounting for the detector characteristics is a simulated signal which approximates as best as possible the expected pressure recorded by the sensor. This simulation of best conformity will be called template. The template alongside the original simulation, where no detector characteristics were accounted for, are shown in Fig. 3.5 (a) and their corresponding frequency spectra in (b).

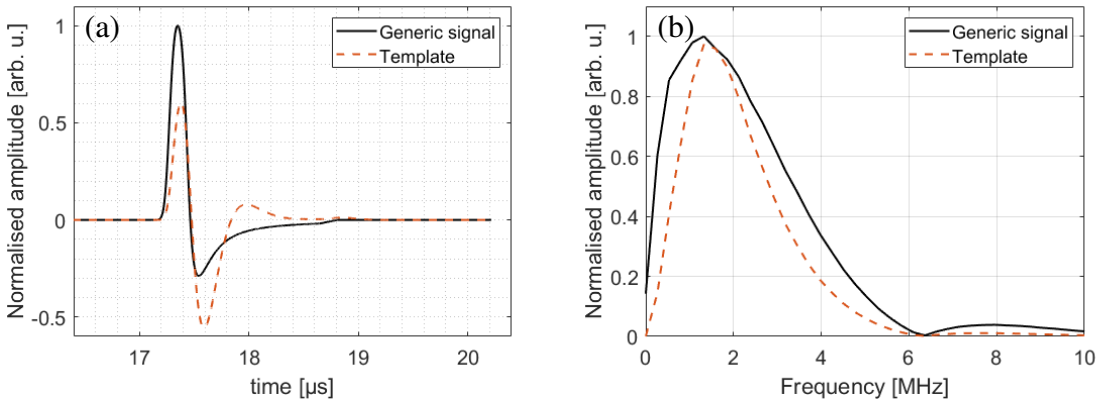

Figure 3.5: The difference between the generic signal (black) and the template (orange), which is a simulation of best conformity to the measurement in (a). The detector characteristics have been taken into account by a band-pass filter. Fourier transforms of the two signals with the same colour scheme are shown in (b).

Panel (a) shows the generic signal (black) whose structure was explained in Fig. 3.4 and the template (orange). The filtering process reduces the amplitude of the signal and distorts the frequency content of the signal, as can be seen from the Fourier transforms in panel (b). The detector clips the signal at both the high and low frequency ends. Frequency components of the signal that lie outside the sensitive range of the detector are suppressed, which causes the significant change in the signal shape (a). The template was later used for the correlation filter in order to denoise the measurements.

Complete signal description

Using the setup shown in Fig. 3.1, ionoacoustic signals were recorded using $20\,MeV$ protons and varying pulse durations. As single measurements typically don't provide the desired signal *SNR* it is quite common in ionoacoustic to average multiple individually recorded measurements to improve the *SNR*. One such measurement using a pulse duration of $160\,ns$ is shown in Fig. 3.6, which is composed of 200 individually recorded measurements that have been averaged in post-processing. The total integral dose of the measurement at the Bragg peak is $126\,Gy$. In addition to the measurement the template is overlaid to demonstrate the similarity between the two.

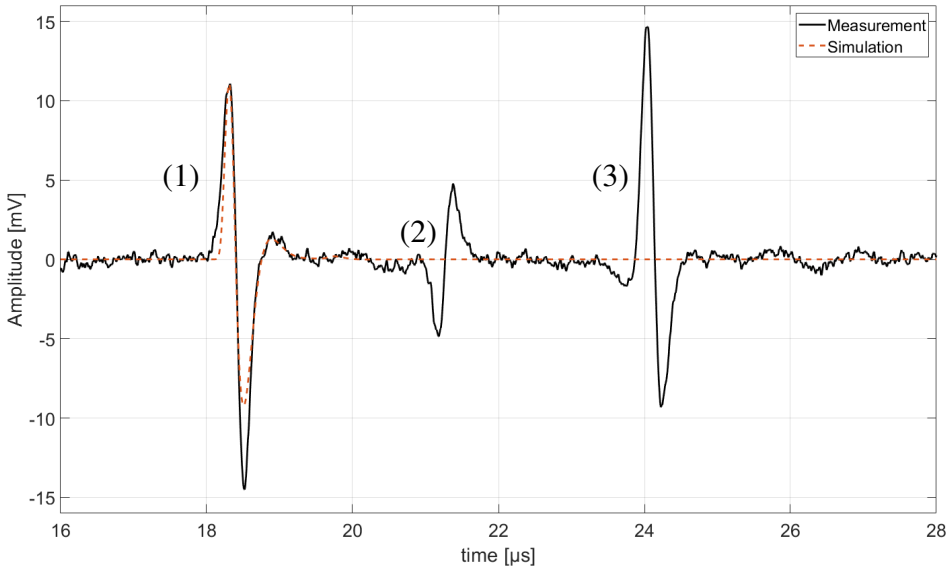

Figure 3.6: Ionoacoustic signal generated by $20\,MeV$ protons and $160\,ns$ pulse duration in water (black). The signal triplett consists of the direct signal (1), the window signal (2) and the reflected signal (3). Additionally to the signal there is a simulation for the direct signal shown in orange. Figure based on Schauer et al. [75].

The ionoacoustic signal (black solid line) shows a triplet structure. It consists of the direct signal (1) followed by the so-called window signal (2) and the reflected signal (3). The direct signal (1) is generated by the pressure wave of the Bragg peak which travels directly to the sensor. It is the most relevant of the three signals, as it is least likely to be overlaid by echoes or secondary signals. It is the only signal, which was simulated in detail as explained in connection with Fig. 3.3, Fig. 3.4 and Fig. 3.5. To demonstrate

the similarity between the measurement and the simulated template (cf. Fig. 3.5 (a)), the template is superimposed with the measurement. To do so, a temporal shift of approximately 1 *mus* was applied to the template, which originates either from a underestimation of the distance between the Bragg peak and the sensor in the simulations or electronic delays caused by the amplifier or the data acquisition. The window signal (2) is generated at the entry window of the proton beam into the water tank. The dose gradient at the window causes an acoustic signal whose difference in time of flight compared to the direct signal is a direct measure of the range of the protons. For a more heterogeneous phantom a window signal is expected at every interface of two different materials, where a dose gradient occurs. The reflected signal (3) is a phase-inverted copy of the direct signal. It is generated by the acoustic wave which, starting from the Bragg peak, travels backwards towards the entrance window and is almost completely reflected there. The time of flight difference between the reflected signal and the direct signal is therefore a measure of twice the range of the protons.

3.2.2 Signal processing

This section deals with the signal processing of the ionoacoustic measurements recorded at the preclinical tandem accelerator. In the following 'measurement' refers to the entire measurement including noise and signal, while 'signal' only refers to the signal within the measurement. In particular, the effect of the correlation filter used on the measurements is discussed and how each measurement is assigned an *SNR* that is used to qualify the measurements. This is demonstrated in connection with Fig. 3.7, which gives an overview of the measurement results at the tandem accelerator. Row (a) shows measurements of ionoacoustic signals with a pulse duration of $50\,ns$, $160\,ns$, $500\,ns$ and $1\,\mu s$ at a beam current of $4.5\,\mu A$. Shown are 5 averages each resulting in a dose between $1\,Gy$ for a pulse duration of $50\,ns$ up to a dose of $20\,Gy$ for a pulse duration of $1\,\mu s$. Row (b) shows the 'Moving Average Power Spectra' (MAPS) belonging to (a), which are used for the SNR_M calculation. Row (c) shows the templates simulated for the respective pulse durations that were used to filter the raw measurements from (a) and thus generate the corresponding correlation functions in row (d). Row (e) shows the MAPS of the correlation functions

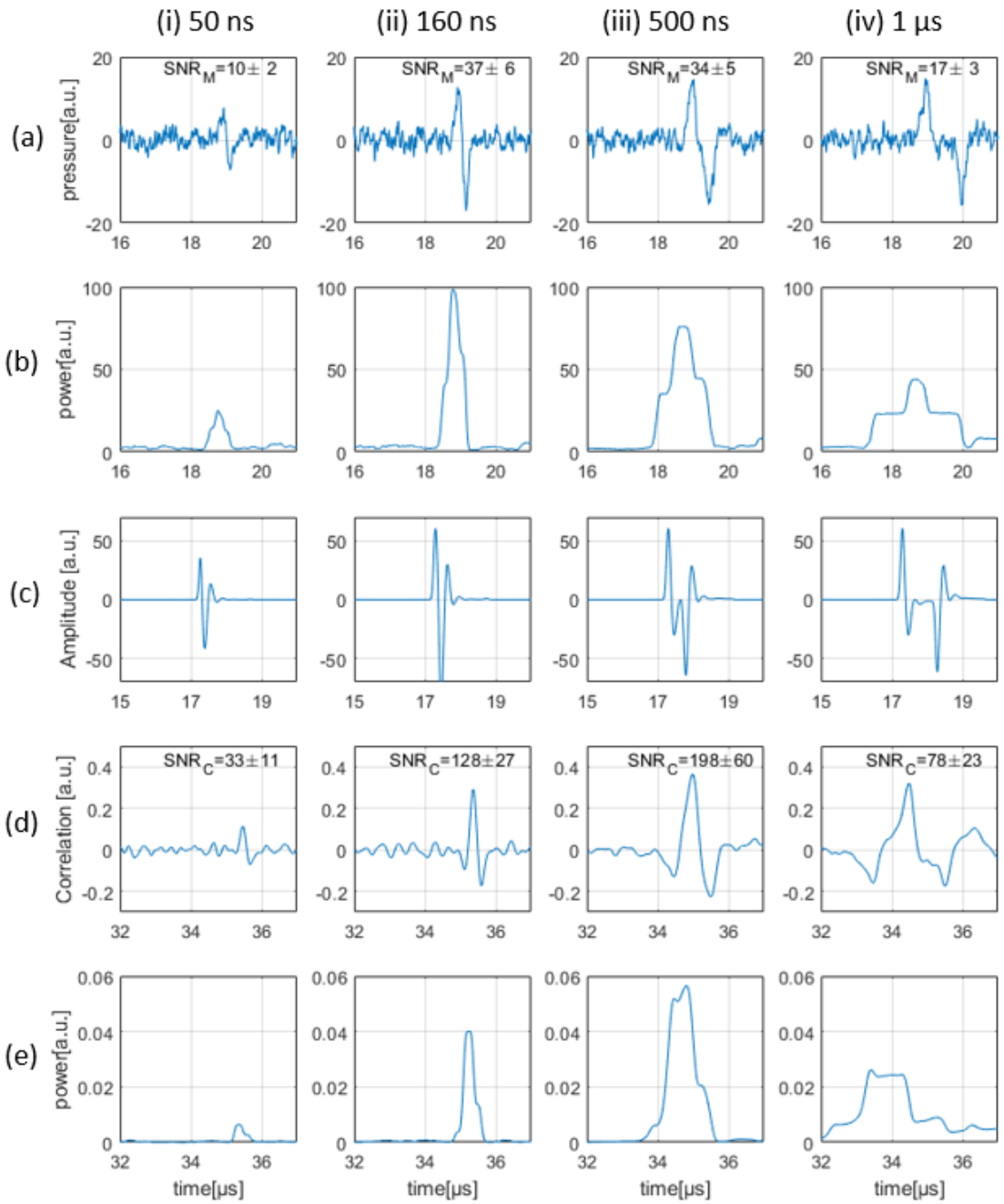

Figure 3.7: Measured signals with 5 averages each are shown in row (a). The deposited dose is between 1 Gy and 20 Gy depending on the pulse duration. The SNR_M values given in row (a) were calculated using the moving average power spectra in row (b). The templates used for the correlation filter process are shown in row (c) resulting in the filtered signals in row (d). The SNR_C values given here were determined by the moving average power spectra in row (e). Figure based on Schauer et al. [75].

used for the SNR_C calculation.

Focusing on the raw measurements in line (a), it can be seen that the maximum signal amplitude increases strongly between the signal corresponding to the $50\,ns$ and the $160\,ns$ pulse duration. For even longer pulse durations ($500\,nsand1\,\mu s$) the signal amplitude stagnates, as it is expected from the simulations shown in Fig. 3.4. For the longest pulse duration of $1\,\mu s$, it can be seen that the signal splits in time into one signal generated at switch-on (at about $19\,\mu s$) and one generated at switch-off (at about $20\,\mu s$). The temporal shift of the two signals corresponds to the pulse duration used. A similar structure is obtained in the simulated templates (iv,c) as the band-pass filtering effect of the included TIR causes the low frequency part of the signal to be attenuated in contrast to the $1\,\mu s$ signal shown in Fig. 3.4.

Correlation function

Panel (d) in Fig 3.7 shows the raw measurements from panel (a) after applying the correlation filter using the templates provided in panel (c). In this case, the templates differ only in the pulse duration adapted to the respective measurement. The correlation function can be understood as a quantification of the similarity between measurement and template for different template positions. This is illustrated in Fig. 3.8.

Three arbitrary template positions in the time frame of a measurement are shown to illustrate the function of a correlation filter. For the first template position (purple), the noise of the measurement and the template show small similarities by chance, which is reflected in a slightly increased correlation coefficient. For the second template position (yellow), no commonality can be found, which results in a correlation coefficient of approximately zero. The third template position (orange) perfectly matches the position of the direct signal in the measurement and is responsible for the correlation peak. Compared to the raw signal, the correlation function shows a linearly shifted time axis. This shift is determined by the signal position in the template and its numerical size, that is how many zeros are included before and after the signal in the template.

Signal-to-noise ratio of the correlation function (SNR_C) is increased compared to that of the input measurement (SNR_M). In fact, the correlation filter is the ideal linear filter, i.e. no other linear filter would result in an even higher SNR_C (cf. sec. 2.4.1). Linear in this

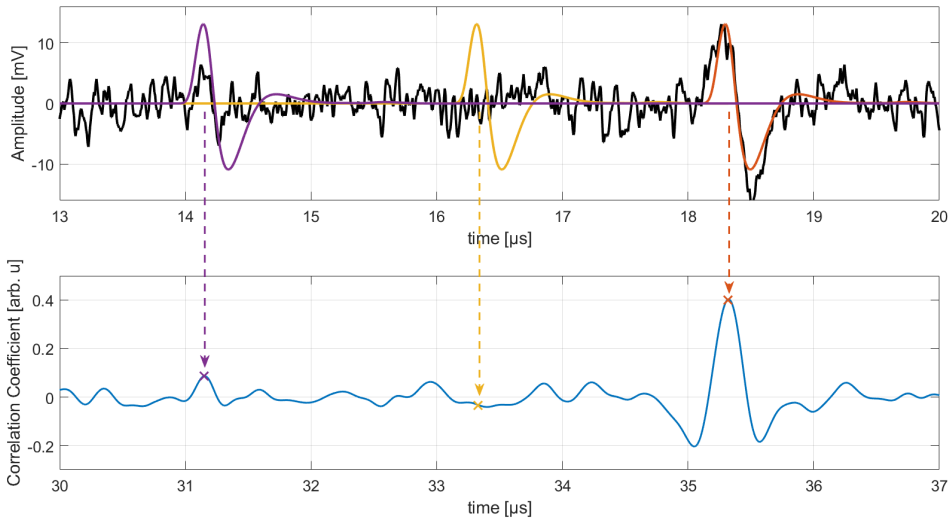

Figure 3.8: Visual illustration of the correlation process. For each template position indicated by different colours, a point in the correlation function is calculated. For each possible template position, the correlation function provides a correlation coefficient that quantifies the similarity between the measurement and the template at the respective position.

context means that the filter does not depend on the measurement itself. Otherwise, the *SNR* could be further increased, for example, by point-wise squaring of the measurement or the correlation function. From Fig. 3.7 (a) and (d) it can be seen that the correlation increases the SNR_M of the raw measurements from a factor 3 for the $50\,ns$ pulse up to a factor of almost 6 for the $500\,ns$ pulse. The reason for this increased *SNR*-enhancement for longer pulse durations is the fact that the *SNR* enhancement is dependent on the total contained signal energy (cf. eqn. 2.36), which increases with increasing duration. For the $1\,\mu s$ pulse, the enhancement decreases again, since the correlation peak is smeared out over a longer duration, diminishing its average power.

Apart from the contained signal energy, the *SNR*-enhancement by a correlation filter depends on two other factors one of which is the frequency content of the noise. The more the frequency content of the noise within the measurement matches that of the template, the worse the SNR_M can be improved by a correlation. This is also the reason why a new correlation of the correlation function would not achieve any new *SNR* improvement. Another crucial point is the quality of the template. The better the template matches the signal shape, the more the *SNR* will be increased by a correlation. The template used

here is not optimal. An optimal template could be extracted, for example, from a measurement of very high integral dose making it close to noise-free and perfectly fitting to the signal shape. Such a template would further increase the SNR_C shown in Fig. 3.7 (d) by approximately 10% .

SNR determination

The signal-to-noise ratio of the raw measurements (SNR_M) displayed in Fig. 3.7 (a) were calculated as the average signal power divided by the average noise power. The same holds true for the SNR_C calculation of the correlation functions in Fig. 3.7 (c). Displayed is the mean value $\pm$ standard deviation as the $SNR_{M,C}$ evaluation was performed for 40 different measurements, containing 5 averages each. An illustration of what is considered signal, what is considered noise and what is excluded from the $SNR_{M,C}$ calculation is given in Fig. 3.9.

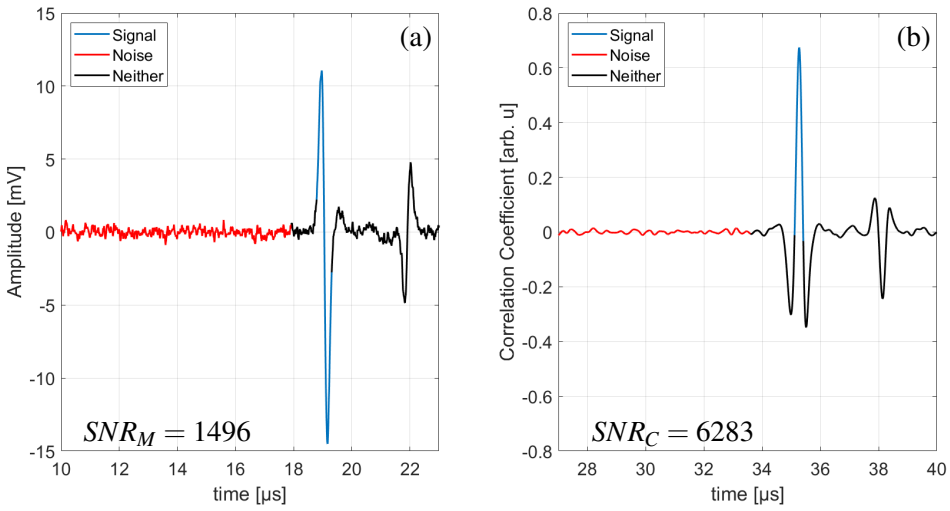

Figure 3.9: A 200-fold averaged ionoacoustic measurement (a) and the corresponding correlation function (b). The colour coding shows what parts from the signal are used for the calculation of the noise power (red), signal power (blue) and which parts are excluded from the *SNR* calculation.

The SNR_M of the measurement (a) and correlation function (b) can be calculated by dividing the average power from the signal part (blue) by the average power contained in the noise part (red) and ignoring secondary signals and unambiguous parts (black).

To determine an accurate signal duration that is independent of noise fluctuations, tem-

plates were used. For the raw measurements, 20% of the maximum signal amplitude of the template was chosen as the starting point and correspondingly 20% of the minimum as the ending point. The duration of the signal could then be determined by the time difference of these two instances. A similar approach was used to determine the duration of the signal in the correlation function. An autocorrelation function of the template was used to obtain a noise free simulation of the correlation function. The duration of the signal in the correlation function (correlation peak) was determined as the temporal difference between the first zero crossing after the main peak and the last zero crossing before the main peak.

To further determine the signal position in the measurement, the MAPS ($\bar{P}(t_j)$) were used, which are displayed in Fig. 3.7 in row (b) and (e), respectively. The MAPS are the average power of the measurement within a duration, which is equal to the signal duration obtained from the corresponding template. Mathematically, it can be expressed as:

$$\bar{P}(t_j) = \frac{1}{d} \sum_{t_i=t_j}^{t_j+d} A_s^2(t_i) \tag{3.4}$$

Where $\bar{P}(t_j)$ is the MAPS, d is the duration of the signal extracted from the thresholds of the templates or autocorrelation function, respectively and t_j is the starting point in samples. When the signal duration is perfectly matched with the signal position, $\bar{P}(t_j)$ peaks at a value equal to the average signal power. The $SNR_{M,C}$ are determined as the maximum value of the $\bar{P}(t_j)$ divided by the average noise power obtained from the raw measurements or correlations, respectively. The noise interval can be chosen arbitrarily as its duration should not alter the average noise power. However, a long noise interval ensures an accurate estimation of the average noise power. Care was taken to ensure that reflections or secondary signals were excluded from the noise power calculation.

The definition and calculation of the *SNRs* shown here has so far only been used to compare different measurements. To give the *SNR* a deeper meaning, a detection probability can be assigned to an *SNR*. This has been empirically investigated and the results are presented in Fig. 3.10. Plotted is the detection probability of a signal depending on its $SNR_{M,C}$ as described above. With increasing *SNR*, the detection probability increases and approaches 100% for *SNRs* larger than 15. 95% detection probability is reached at

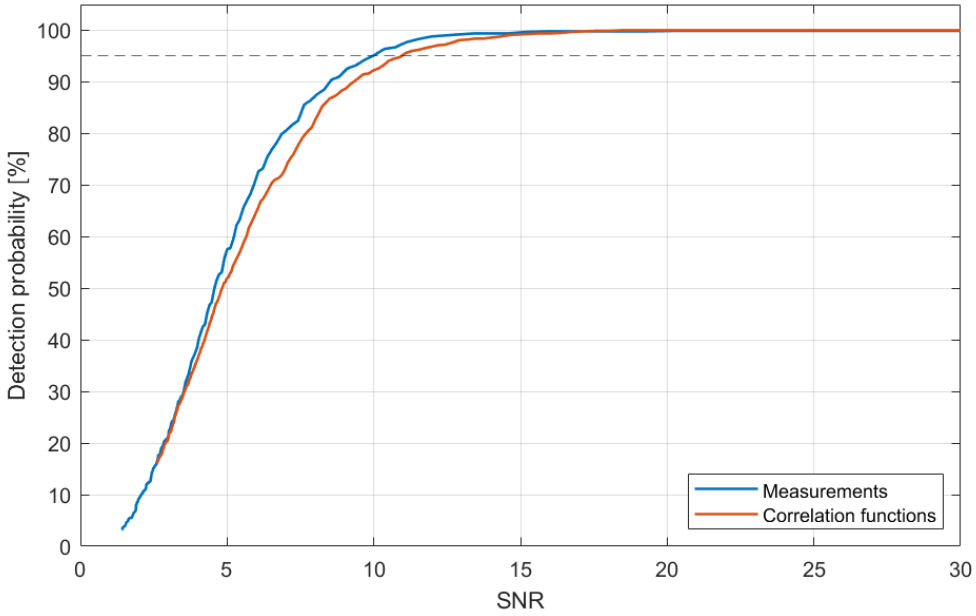

Figure 3.10: *SNR* dependent detection probability for the raw measurements (blue) and the correlation functions (orange). A 95% detection probability (dashed line) is reached at an *SNR* of 10-11.

an *SNR* of 10-11. This detection probability was evaluated by simulating templates with increasing amplitudes (230 templates with 230 amplitudes in total). Subsequently, each template was summed with 1000 different noise measurements containing only noise and no signal. For each template amplitude, 1000 different noisy signals were generated in this way. For all 1000 noisy measurements per amplitude, an SNR_M was calculated and the resulting 1000 *SNRs* were averaged. For the *SNR* found in this way, the detection probability was determined as follows: If the position of the highest peak in the generated noisy simulation matches the position of the highest peak in the noise-free simulation more accurately than $\pm 64\,ns$ (this accounts for approx. $\pm 0.1\,mm$ assuming a speed of sound of $1.5\,mm/\mu s$), the measurement was considered to be correctly detected. This procedure was performed in the same way after correlating the measurements with the template resulting in a detection probability for the SNR_C

It should be stated that the *SNR* as it is defined here and its link to a detection probability comes with limitations that can be summarised in two categories. The first category comes with the statistical nature of noise. It was found that the *SNR* is subject to fluctuations under otherwise identical conditions. One reason for this is that the signal can

randomly overlap with the noise, either constructively or destructively. Another reason is that in some measurements there are (visible and/or invisible) artefacts in the noise that can change the noise power for otherwise identical measurement scenarios. Additionally, the link to a detection probability is dependent on the noise duration. The longer the noise interval, the higher is the probability that by chance a noise peak exceeds the maximum signal amplitude.

Given these uncertainties, which can only be reduced to a certain extend, there are additional uncertainties originating from the chosen parameters going into the *SNR* calculation. Fig. 3.10 is only valid if these parameters such as the definition of the signal duration and the permitted jitter of the peak are strictly adhered. Since the sensor itself also shapes the signal and the noise, it is certain that the detection probability must also be adapted to a specific sensor.

In a clinical context, however, these parameters need to be fixed in order to assign the quality of a measurement to an action. For the remainder of this thesis, however, the uncertainties will be taken into account by giving, if available, an average $SNR_{M,C}$ calculated from multiple independent measurements and an uncertainty given by the standard deviation. Additionally, the evaluated *SNRs* will only be used to compare measurements relative to each other and draw conclusions about ideal measurement parameters.

3.2.3 Ideal beam parameters

In this section, the choice of ideal beam parameters to obtain an ideal *SNR* at constant doses is discussed. For this purpose the $SNR_D = \frac{SNR}{D}$ is introduced as the *SNR* of the raw measurements or correlation functions, respectively, normalised by the dose D. This SNR_D can be used to compare measurement of different beam parameters, since it takes into account the necessity to work with a limited dose, which is, in a clinical context, defined by the treatment planning process. First, the dependency of the SNR_D on the number of pulses is discussed, followed by the dependency on the pulse duration and shape, the beam current and lastly the lateral beam extend and sensor shape. If relevant, the findings are extrapolated to higher clinical energies.

Number of pulses

As a first step, the number of pulses and their effects on the ionoacoustic signal and its SNR_D were investigated. For this purpose, up to four pulses with 200 ns pulse duration and 200 ns pulse-to-pulse distance were recorded. These parameters were chosen to ensure to record every signal fully and avoid destructive interferences, which can reduce the signal amplitude. Care was taken to leave other beam parameters such as beam current or beam geometry unchanged. These measurements are shown in Fig. 3.11.

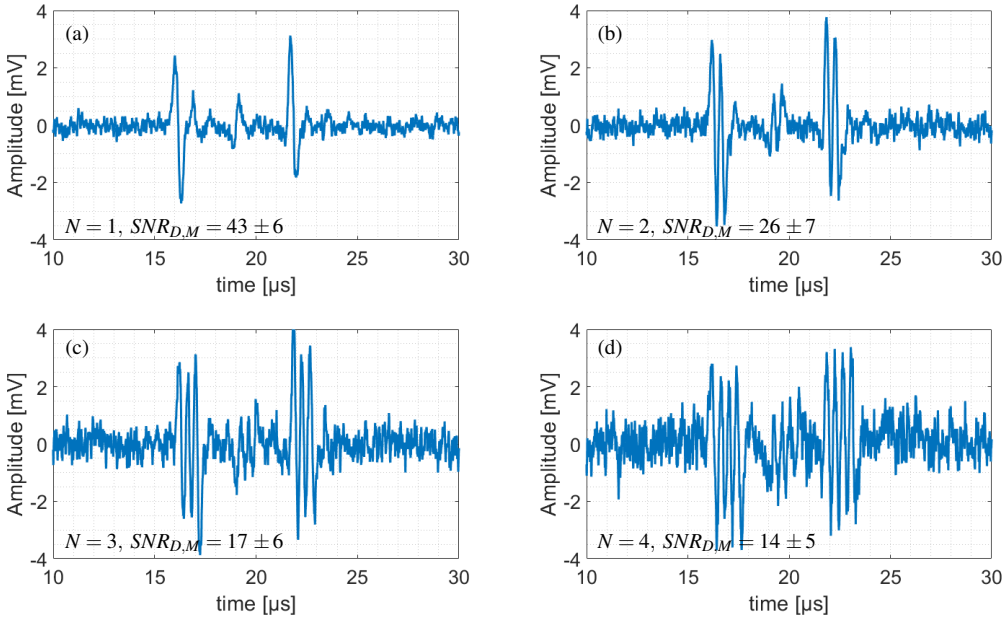

Figure 3.11: Raw ionoacoustic signals with different number of pulses N but same pulse duration (200 ns) and same pulse to pulse distance (200 ns). The $SNR_{D,M}$ compares 120 averages of the single pulse (a) with 60 averages of the double pulse, 40 averages of the triple pulse, and 30 averages of the quadruple pulse (d). Due to the decreasing number of averages, the dose of each measurement is constant (60 Gy).

In order to keep the dose constant despite the increasing number of pulses N, fewer averages were taken into account as the number of pulses increased. Specifically, in Fig. 3.11, 120 averages of a single pulse (a) up to 30 averages of a quadruple pulse (d) are compared. The $SNR_{D,M}$ given for comparison shows that the best $SNR_{D,M}$ can be achieved for the single pulse. The reason for this is the fact that higher averaging numbers reduce the noise level of the measurement. With the application of several pulses in one measurement, only fewer measurements can be averaged, while ensuring identical dose

levels. The noise floor therefore increases with increasing pulse number, as can be seen in Fig. 3.11. The correlation functions associated with the measurements in Fig. 3.11 are shown in Fig. 3.12.

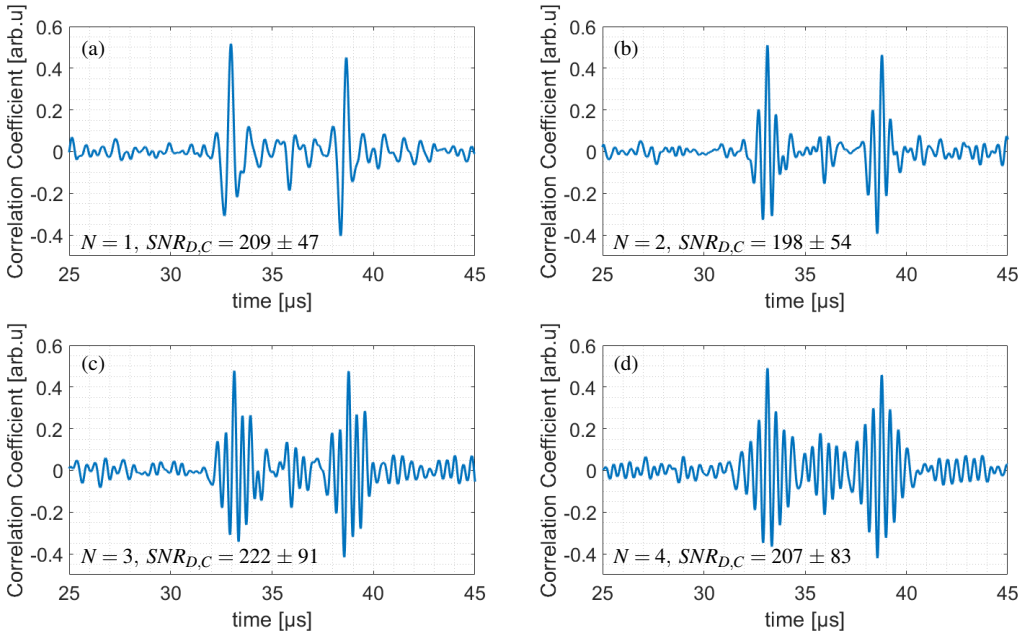

Figure 3.12: Correlation functions corresponding to the raw signals of Fig. 3.11. For an increasing number of pulses within a single measurement N, the averaging number is reduced to ensure a constant dose for all compared correlation functions ($60\,Gy$).

For each signal in Fig. 3.11, a template was created, taking into account the different number of pulses by corresponding heating functions. The filtered signals (correlation functions) are shown in Fig. 3.12. All $SNR_{D,C}$-values coincide within the given measurement uncertainty. This is expected, since the SNR_C of a correlation function is directly proportional to the contained signal energy within the raw measurements (cf. eqn. 2.36). Since the total number of pulses considered does not change between the compared measurements, the total energy is also expected to be identical. The relatively large standard deviations are primarily caused by beam current fluctuations.

When observing the correlation functions, it is noticeable that with an increasing number of pulses, the signal in the correlation function starts to oscillate. These smaller peaks to the left and to the right of the main peak are called sidelobes. In the $SNR_{D,C}$ calculation, these sidelobes were neither attributed to the noise nor to the signal. If the sidelobes were considered as noise or signal, the $SNR_{D,C}$ would be reduced. With more noisy signals,

these sidelobes can become a problem, since it is conceivable that one of the sidelobes could by chance exceed the actual central peak. Since the peak position of the correlation function indicates the signal position in the measurement, it is of great importance that the sidelobes do not exceed the central peak. It was therefore decided to perform future experiments with single pulses which, thanks to a precise trigger, do not show any disadvantages compared to the multiple pulses with regard to their $SNR_{D,C}$.

Ideal pulse duration and shape

The pulse duration of the proton beam used for the generation of the ionoacoustic signal influences the $SNR_{M,C}$ of the signal and the applied dose. Using the SNR_D, signals of different pulse durations can be compared and an ideal pulse duration can be determined. For a fair comparison of the different pulse durations, it is necessary to ensure a constant instantaneous beam current for all pulse durations ($4.5\,\mu A$ for the tandem accelerator). This means that the applied dose increases linearly with increasing pulse duration. To find the ideal pulse duration for the experimental parameters used at the tandem accelerator, an SNR_D was calculated for ionoacoustic signals caused by proton pulses of durations between $30\,ns$ and $1\,\mu s$. The results are shown in Fig. 3.13.

Shown are SNR_D values of the raw measurements (blue) and the correlation functions (orange). The data points are based on 20 measurements for each pulse duration, with each measurement containing 200 averages. To determine the SNR_D, these 20 measurements were evaluated separately and the resulting 20 *SNRs* were averaged and then divided by the total dose included. The dose is the product of the number of averages, the pulse duration and the dose rate ($4\,MGy/s$ in CW). The error bars are given as the standard error of the mean ($SEM = \frac{\sigma}{\sqrt{N}}$) of each of the 20 individual measurements. For a fair comparison of the SNR_D values, an external noise measurement was used to determine the noise power for all measurements. The error bars are mainly due to beam current instabilities from the accelerator side. For the simulations (black dashed lines), templates with varying pulse duration were simulated and used to calculate the signal power. The noise power for the simulations of $SNR_{D,M}$ was assumed to be constant. For the $SNR_{D,C}$ simulation of the correlation function, the templates were correlated with the external noise measurement, since the noise power of the correlation function increases with in-

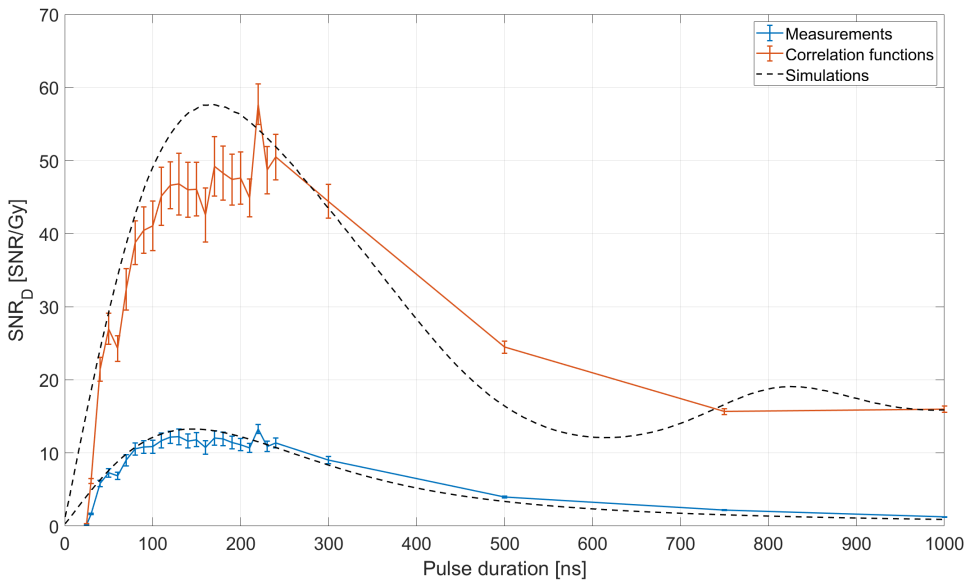

Figure 3.13: Dose normalised SNR_D for ionoacoustic measurements at the tandem accelerator given in units of SNR/Gy. The ideal pulse duration can be extracted as the maximum position of the curves and is approximately $140\,ns$ for the raw measurements (blue) and $170\,ns$ for the correlation functions (orange). The measurements are given as mean value $\pm$ SEM and are backed up by simulations (dashed black lines). Figure adopted from Schauer et al. [75].

creasing pulse duration. Both simulations were scaled to best match the measured data.

The ideal pulse duration can be extracted from Fig. 3.13 as the maximum position of the plots and is about $140\,ns$ for the measurements and $170\,ns$ for the correlation functions. These pulse durations describe the ideal tradeoff between maximising ionoacoustic amplitude and minimising dose deposition. However, both plots show a flat maximum, which means that small deviations from the ideal pulse duration do not lead to large deviations in the obtained SNR_D. The increase in ideal pulse duration between the raw measurements and the correlation function is explained by the fact that the SNR_C of the correlation functions is dependent on the total energy of the original signal, which increases as the pulse duration increases.

The plots shown in Fig. 3.13 are only valid for the setup used at the tandem accelerator and shall additionally show that the SNR_D values can also be accurately described by simulations. In particular, the ideal pulse duration depends on a number of factors such as the detector, detector position, pulse shape, proton energy and proton energy spread, to name the most prominent ones. However, the ideal pulse duration is independent of the

instantaneous beam current as a different instantaneous beam current would only scale the whole curves but the maximum position would remain unaltered.

In the following, the simulations from Fig. 3.13 are extrapolated to clinical conditions to show how the SNR_D and the corresponding ideal pulse duration depend on some of these factors. Figure 3.14 shows an extrapolation to a clinically relevant energy of $220\,MeV$ and the more typical Gaussian pulse shapes in comparison with rectangular ones.

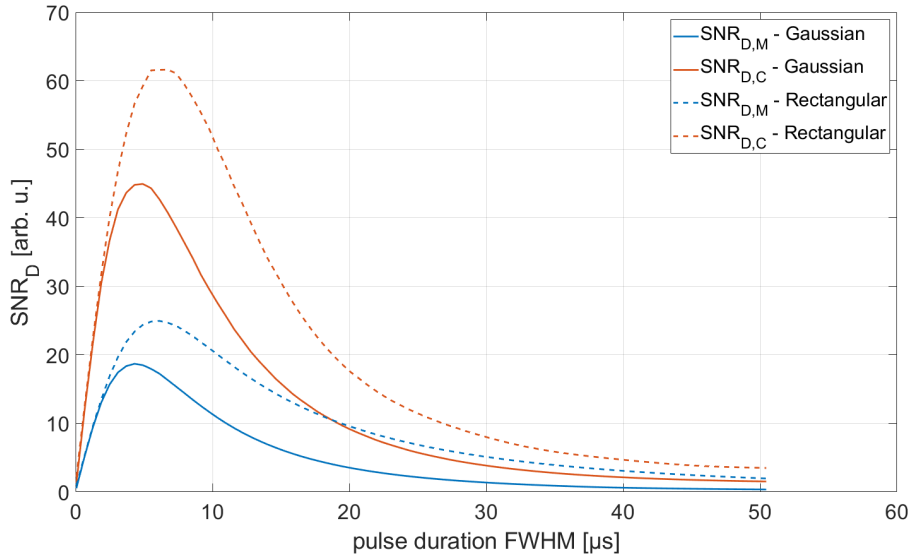

Figure 3.14: Simulations for SNR_D-values of ionoacoustic signals generated by monoenergetic $220\,MeV$ protons. A distinction is made between Gaussian (solid) and rectangular (dashed) pulses for the evaluation of the raw measurements (blue) and the correlation functions (orange), respectively. Ideal pulse durations range from $4\,\mu s$ to $7\,\mu s$ and are larger for rectangular pulses than for Gaussian ones and larger for the evaluation of the correlations than for the raw measurements. Figure based on Schauer et al. [75].

Plotted are pulse duration dependent SNR_D values for a proton energy of $220\,MeV$. The plot is divided into the evaluations of the raw measurements (blue) and correlation functions (orange). In addition, a distinction is made between rectangular (dashed) and Gaussian pulses (solid). For the Gaussian pulses, the pulse duration is represented by the FWHM.

Analogous to Fig. 3.13, templates with varying pulse duration were simulated. The simulation was designed to fit data measured in 2017 by Lehrack et al. [32]. The noise power was determined from a noise measurement of the Cetacean C305X hydrophone used in this study, which has a flat frequency response between $10\,kHz$ and $250\,kHz$. The beam

parameters were adapted to reproduce measurements shown in the work of Lehrack et al., namely a fixed instantaneous beam current within the FWHM of $432\,nA$ and an integral dose of $10\,Gy$ at the Bragg peak. For the evaluation of $SNR_{D,M}$, the noise power was assumed to be constant. The noise power for the calculation of the $SNR_{D,C}$ was determined after correlating the template with the external noise measurement. The resulting *SNRs* were then divided by the contained dose to determine the SNR_D. The dose is solely dependent on the pulse duration, since all other parameters (beam current, beam geometry) were kept constant.

The increase of the ideal pulse duration for the simulations of $220\,MeV$ protons ($4\,\mu s - 7\,\mu s$) compared to $20\,MeV$ protons ($140\,ns - 170\,ns$) originates from the longitudinally broader dose distribution of the Bragg peak. The reason for this broadening of the dose distributions is the increased range straggling (cf. sec. 2.1.2), which increases linearly with the proton energy [44]. The dose distribution contributes directly to the signal structure in the form of $P_\delta(t)$ (cf. Fig. 3.3) and thus determines the ideal pulse duration (cf. Fig. 3.4) on the one hand, and the central frequency of the signal on the other. The central frequency is thus significantly lower for the $220\,MeV$ protons ($< 100\,kHz$) compared to the $20\,MeV$ protons ($1.3\,MHz$).

Fig. 3.14 also illustrates that rectangular pulses lead to a higher SNR_D than Gaussian ones. This is explained by the steeper gradients of the temporal heating function (cf. eqn. 2.16), which enable a more efficient signal generation. Rectangular pulse shapes should thus be preferred for ionoacoustic signal generation if available. Furthermore, rectangular pulses require slightly longer pulse durations to reach the maximum SNR_D. This result must be interpreted with caution, since it depends on how the duration of a Gaussian pulse (here: FWHM) is defined. An important point to emphasise is that there is some freedom in choosing the pulse duration without significantly reducing the SNR_D. For the plotted curves, a deviation of 30%-40% from the ideal pulse duration results in an SNR_D loss of only about 10%.

The simulations were further extrapolated and ideal pulse durations for ionoacoustic signal generation under the premise of a correlation based evaluation were derived for monoenergetic proton energies between $20\,MeV$ and $260\,MeV$. The results are shown in Fig. 3.15.

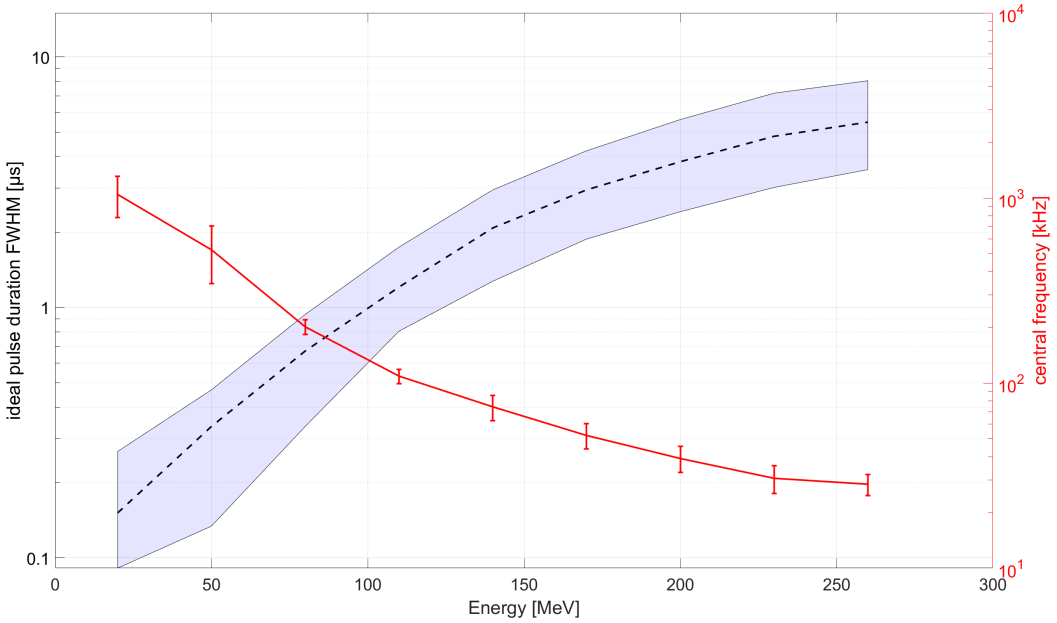

Figure 3.15: Ideal pulse duration for monoenergetic proton energies and Gaussian pulse shape (dashed black line). The shaded region shows pulse durations for which at least 90% of the maximum possible SNR_D can be achieved. For each proton energy, the central frequency of the corresponding signal is plotted on the right y-axis. Figure adopted from Schauer et al. [75].

The ideal pulse duration (black dashed line) increases from about $150\,ns$ for $20\,MeV$ protons to about $6\,\mu s$ for the highest considered energy of $260\,MeV$. The shaded area shows pulse durations for which at least 90% of the maximum possible SNR_D can be achieved. The central frequency of the signal of each energy (red line) is plotted in an additional y-axis. The frequency decreases continuously with increasing energy from about $1.3\,MHz$ to about $30\,kHz$. The specified bandwidth of pulse durations in turn causes a bandwidth of the central frequencies of the signals, which are indicated as error bars.

The simulations are based on the use of monoenergetic Bragg curves and Gaussian pulse shapes. Analogous to Fig. 3.14, measured noise was used as an accurate noise estimate. Care was taken to ensure that the used noise measurements contained all frequencies, which are present in the ionoacoustic signal. Furthermore, a point sensor with infinite bandwidth and a large distance to the Bragg peak was assumed. In this context, large means that the spherical integration over the dose distribution (cf. Fig. 3.3) in the region of the Bragg curve can be locally regarded as flat. This choice ensures reproducible

results that are not dependent on setup or beam specific parameters. However, it is important to emphasise that the data shown can change when more realistic conditions are taken into account. Most prominently, taking into account a non-negligible energy spread leads to an increase of the ideal pulse duration as it broadens the longitudinal extend of the dose distribution. It is also important to emphasise that frequencies outside the error bars shown are also relevant for the detection of ionoacoustic signals.
In summary, efficient signal generation requires pulse durations ranging from $1\,\mu s - 8\,\mu s$ for clinically used energies ($70\,MeV$-$260\,MeV$). The ideal duration is most dominantly determined by the used proton energy and the corresponding longitudinal extend of the dose distribution around the Bragg peak. Other beam or setup specific parameters, such as the pulse shape, the energy spread of the protons or the used detector also influence the ideal pulse duration and impact the highest possible SNR at a given dose (SNR_D). However, the requirement of the ideal pulse duration must not be met perfectly in order to achieve reasonable SNR_D. Pulse durations close to the ideal pulse duration will deliver comparable SNR_D.

Ideal beam current

Another important parameter in the context of ionoacoustic signal generation is the beam current. Only the instantaneous beam current, that is the beam current in the proton pulse, is decisive for signal generation. The average beam current can be chosen almost arbitrarily by adjusting the pulse repetition frequency without changing the ionoacoustic signal. The only requirement on the pulse repetition frequency is that it has to be low enough so that signals of consecutive pulses do not interfere. To ensure a fair comparison of two signals with different beam currents, the applied dose is kept constant (SNR_D). This can be achieved by reducing the number of measurements taken into account with high beam current compared to measurements with lower beam current. Fig. 3.16 shows such a comparison.
While keeping all other beam parameters constant, two measurements with different instantaneous beam currents were recorded and summed with respect to an upper dose limit of $12\,Gy$. Fig. 3.16 (a) shows the sum of 80 signals generated by $20\,MeV$ protons at an instantaneous beam current of $0.65\,\mu A$ and a dose of $0.15\,Gy$ per pulse. The signal yields

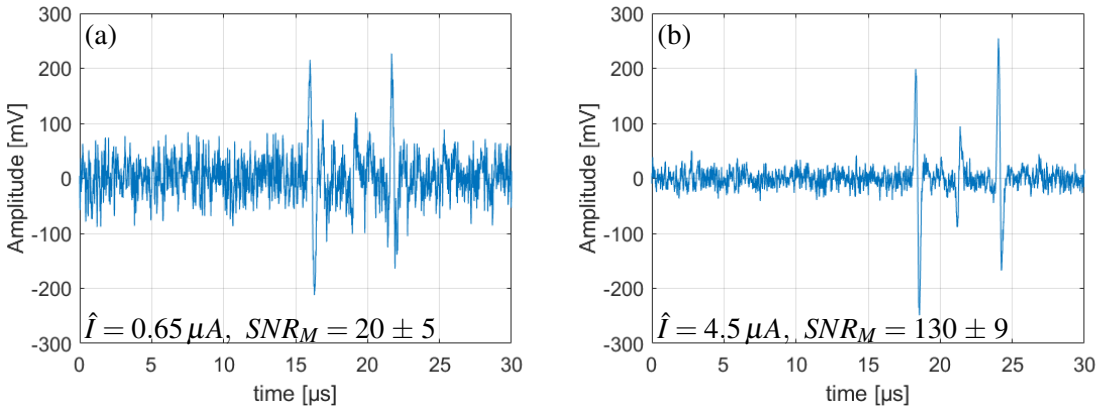

Figure 3.16: A measurement with low instantaneous beam current (a) is compared with a measurement of high instantaneous beam current (b). The dose at the Bragg peak ($12\,Gy$) is kept constant for both measurements by reducing the number of measurements taken into account from 80 (a) to only 15 (b). Figure based on Schauer et al. [75].

an SNR_M of 20 ± 5. In Fig. 3.16 (b), the same dose was applied using the same pulse duration ($200\,ns$) with an increased dose of $0.8\,Gy$ per pulse. The summed signal shows an SNR_M of 130 ± 9. The signals were summed rather than averaged to demonstrate the similar amplitudes of the signals which is only dependent on the total number of particles, which is equal in both cases. Summing rather than averaging multiple measurements does not affect the indicated SNR_M. The evaluation here is limited to the raw measurements since an increased beam current does not change the performance of the correlation. The corresponding SNR_C are thus expected to increase the shown SNR_M by a factor of approximately four in both cases.

The reason for the significantly higher SNR_M for an increased beam current can best be explained by considering the signal and the noise separately. Under otherwise identical setup conditions, the signal amplitude is independent of the beam current and depends only on the total dose and thus the number of protons. This is shown by the similar signal amplitudes in Fig. 3.16 (a) and (b). Due to the significantly higher number of measurements in the case of the low beam current, however, the noise floor is higher compared to the measurement with higher current. For the addition of n measurements, the noise floor increases by the factor $\sqrt{n}$ (cf. sec. 2.4.2). Thus, the mean amplitude of the noise floor of the measurement with 15 signals is lower than that of the measurement with 80 signals by the factor $\sqrt{15/80}$ assuming ideal white noise. Since the calculation of the

SNR_M involves squaring, the expected SNR_M ratio can be calculated directly from the ratio of beam currents. Here, the ratio of the SNR_M values ($\frac{SNR_M(4.5nA)}{SNR_M(0.65nA)} = 6.5$) is close to the value expected from the ratio of beam currents ($\frac{4.5nA}{0.65nA} = 6.9$). The advantage of high instantaneous beam currents for ionoacoustic signal generation can be scaled up to the limiting case in which the entire dose is deposited in a single pulse of ideal duration. Even for a single pulse of ideal duration, which contains the whole dose, the SNR_M can further be increased. For this purpose, the current must be increased even further so that a single pulse of ideal duration would exceed the dose limit. To maintain a constant dose, the duration of the single pulse can then be shortened. This relationship is shown in Fig. 3.17.

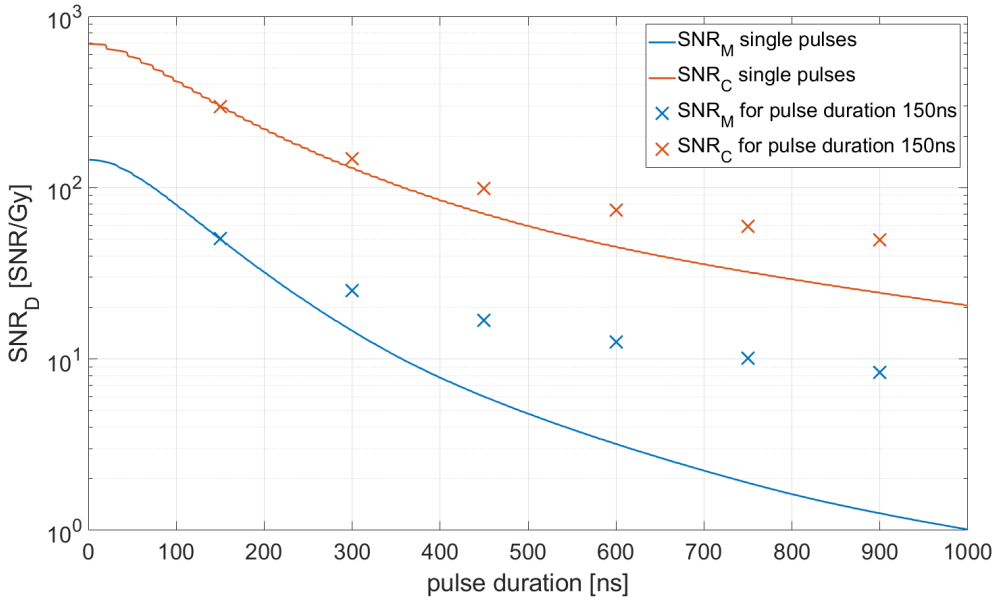

Figure 3.17: Simulations for the SNR_D of single unaveraged pulses at $20\,MeV$ proton energy with variable pulse duration for the raw measurements (blue, solid) and the associated correlations (orange, solid). The beam current decreases for longer pulse durations to ensure a constant dose of $1\,Gy$. In addition, the crosses indicate how the $SNR_{D,M}$ (blue) and $SNR_{D,C}$ (orange) would behave if several pulses with ideal pulse duration $150\,ns$ were averaged. Figure adopted from Schauer et al. [75].

The simulation shows the the SNR_D for single, unaveraged measurements in dependency of the pulse duration. This is plotted for the raw measurements (solid blue line) and the corresponding correlation (solid orange line). For a given pulse duration, the SNR_D of these single shot simulations is compared to averaging multiple measurements using the

ideal pulse duration in each pulse (blue and orange crosses respectively). The beam current along a vertical line in Fig. 3.17 is always constant and decreases for increasing pulse durations in order to maintain a constant dose. At a pulse duration of 150 ns, the total dose (1 Gy) is applied just in one pulse of ideal duration, which is why the marker is positioned on the solid lines. To the left of 150 ns, the beam current is so high that a pulse duration of 150 ns, would exceed the dose limit, which is why the pulse duration is shortened. The SNR_D continues to increase for this extreme case, i.e. for arbitrarily high beam currents it is advantageous to abandon the condition of the ideal pulse duration in order to achieve maximum SNR_D. To the right of 150 ns the beam current becomes progressively lower, allowing either a long pulse (solid lines) or several pulses of ideal duration (crosses) to be applied. In this case, it is advantageous to chop a long pulse into several pulses of ideal duration and then to average the signals of these pulses.
In summary, high instantaneous currents are unreservedly advantageous for ionoacoustic signal generation. At the highest possible beam current, a total 'beam-on' time can be calculated for the desired dose. If this beam-on time is less than the ideal pulse duration for this energy, the entire dose should be applied in a single pulse of this beam-on time. If the beam-on time is longer than the ideal pulse duration, the irradiation should be applied in several pulses of ideal duration to achieve a maximum SNR of the ionoacoustic signals.

Beam and sensor geometry

The dependence of the ionoacoustic signal on the lateral size of the beam or the area of the detector has not been investigated experimentally. However, simulations using 20 MeV-protons at a pulse duration of 160 ns were used to compare a narrow beam with a broad beam for a small and a large sensor, respectively. The narrow beam has a FWHM at the Bragg peak in the lateral dimension of 2.3 mm while the broad beam has a FWHM at the Bragg peak of 6.8 mm. The ratio of the beam areas at the Bragg peak is therefore approximately a factor of 9. The sensor was positioned distal to the beam with a distance of 25.4 mm to the Bragg peak. The small sensor is quadratic with a surface area of 4 mm^2 and the large sensor is also quadratic with a surface area of 36 mm^2 yielding the same ratio of area as the beams. For the simulation of a finite detector surface area multiple point sensors are homogeneously distributed over the desired area and the signals recorded by

these individual point sensors are averaged. For all sensors an infinite bandwidth was assumed. The signals resulting from the simulations for all four possible configurations are shown in Fig. 3.18.

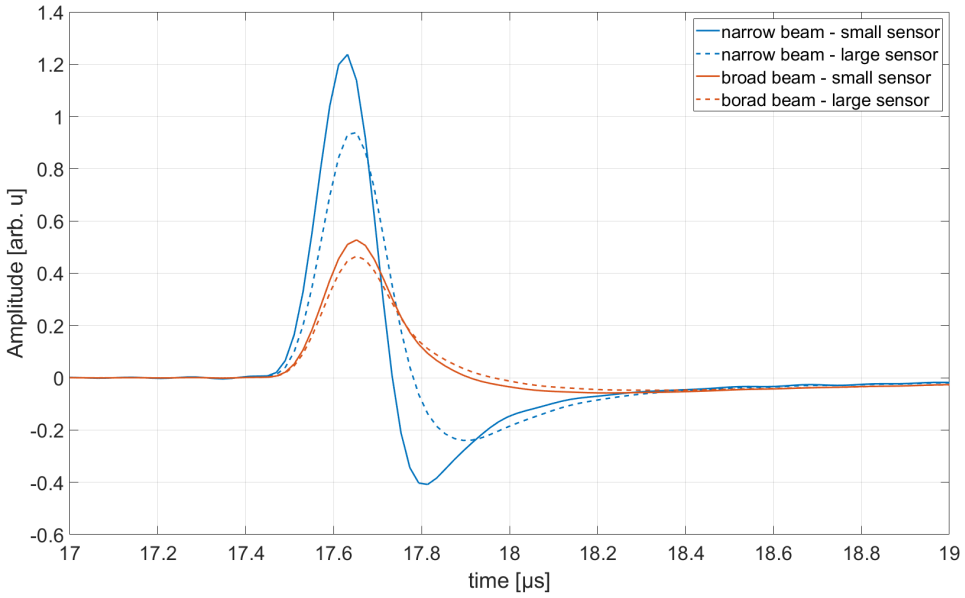

Figure 3.18: Simulated ionoacoustic signals of 20 MeV protons and 160 ns pulse duration for narrow (solid) and broad (dashed) beams for a small sensor (blue) and a large one (red), respectively. Both sensors are modelled as multiple point sensors arranged together to cover the desired area whose individual signals are subsequently averaged. In both cases square sensors with infinite bandwidth at a distance of 25.4 mm to the Bragg peak were assumed.

The signal with a narrow beam and a small sensor (blue, solid) shows the largest signal amplitude and the highest frequency content. In comparison, signals with increased beam diameter (blue, dashed) or a larger sensor (orange, solid) show a lower frequency content and a reduced amplitude. Due to the spatial extend of the beam or the sensor respectively, the time of flight of the individual pressure contributions from the Bragg peak to the sensor is no longer precisely defined as the Bragg peak itself and the sensor have no precise location but are extended in space. This causes different arrival times for different pressure contributions and thus the individual pressure contributions are not perfectly in phase resulting in reduced amplitude and a lower frequency content. This effect is maximised for a wide beam and a large sensor (red, dashed), however the effect no longer increases much once either the sensor or the beam is large. The degree of

the phase shift between the individual pressure contributions is not only defined by the sensor or beam size, respectively, but has to be seen in relation to the distance between the Bragg peak and the sensor. It is ultimately the angle between the Bragg peak and the sensor that defines how coherently the individual pressure contributions are averaged. The most coherent averaging can be achieved for small sensors and beam diameters and a large distance between the Bragg peak and the sensor.

Care must be taken to interpret Fig. 3.18 correctly as both, the broad beam and the large sensor, come with an advantage, which is not directly evident from the figure. On the one hand, the maximum dose deposited at the Bragg peak reduces for larger beam diameters even though the number of protons was kept constant for each configuration. As the protons cover a larger area and thus volume the maximum dose reduced in this case from $0.45\,Gy$ for the narrow beam diameter by a factor 6.4 to $0.07\,Gy$ for the broad beam diameter. Regarding an SNR_D comparison the signal originating from the broad beam would thus be higher than the one from the narrow beam. On the other hand, the advantage of the larger sensor is reflected in the expected noise level of the respective configuration. It is not straight forward to determine how much of a noise level reduction could be achieved using a larger sensor, since it is not known how exactly the noise level scales with the area. However, assuming that the large sensor is perfectly modelled by multiple point-like sensors covering the same area whose individual signals are subsequently averaged, more signals can be averaged when a larger sensor is used. Under this assumption, the noise floor would reduce with the square root of the number of point-like sensors, which is directly proportional to the square root of the ratio of the areas.

Both these advantages can also be exploited using narrow beams and small sensors. To reduce the maximum dose at the Bragg peak with a narrow beam, the beam can be scanned laterally over a larger area. This is called pencil beam scanning (PBS) and is the current state of the art of delivering the beam in clinical proton therapy, scanning the beam laterally over the tumour volume. For small scanning distances, it is possible to measure ionoacoustic signals with a stationary sensor, while for larger scanning distances it is conceivable to move the sensor alongside with the lateral beam position. A reduction of the noise floor as it is achieved by a large sensor can be realised by measuring ionoacoustic signals with multiple small sensors arranged together in a so-called array. In contrast to a

large sensor, this comes with the additional advantage that the phase of the individual signals could be corrected in signal-processing and thus coherent averaging of the individual signals can be ensured.

3.2.4 Range estimation

The experiments at the preclinical tandem accelerator were primarily designed to gather fundamental knowledge about the dependencies of the ionoacoustic signal on beam and recording parameters. Nevertheless, the measurements were evaluated with respect to the range of the protons. For this evaluation, the beam parameters were set as ideal as possible. For robust range verification at minimum dose deposition, it was sufficient to evaluate unaveraged signals with a pulse duration of 130 ns, which is shorter than the ideal pulse duration (cf. Fig. 3.17). An example of such a signal with the corresponding correlation function is shown in Fig. 3.19.

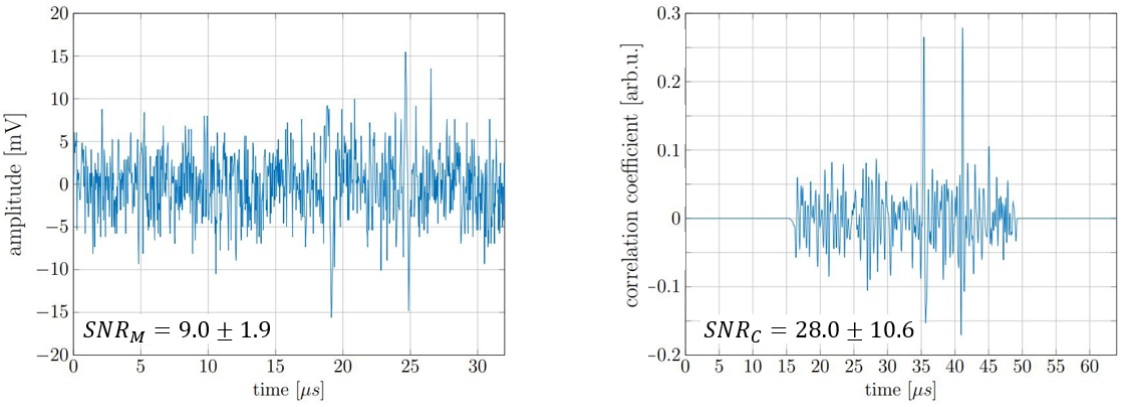

Figure 3.19: Unaveraged ionoacoustic signal recorded from a pulse duration of 130 ns containing 0.5 Gy dose at the Bragg peak (a). The corresponding correlation function is plotted in (b). Figure based on Schauer et al. [75].

The single measurement shown as an example was recorded with an instantaneous current of 4.5 μA and a total number of 3.7×10^6 particles. The peak dose could thus be limited to 0.5 Gy. The correlation function in (b) reveals the signal position of the direct and reflected signal. The SNR_M and SNR_C values displayed are average values determined after evaluating 200 independent measurements.

The time of flight difference between the direct signal and the reflected signal was used to evaluate the range. Since the pressure wave of the reflected signal travels a longer dis-

tance, which corresponds to twice the range of the protons, the time of flight difference can be used to approximate the range of the protons.

$$R = \frac{v_s \times ToF}{2} \tag{3.5}$$

Here v_s is the speed of sound ($1482\,m/s$) at the measured temperature ($22.4\,^\circ$) of the water. The time of flight (ToF) is the difference in time between the maximum position of the correlation peak of the direct signal and the reflected signal and R is the range of the protons.

The range was evaluated from 200 individual measurements to be $R = 4.25\,mm \pm 0.01\,mm$. The indicated error is the standard deviation of the range evaluations of the 200 individual measurements. This shows that the range can be determined with a very high precision of approximately $2\,‰$ using only $0.5\,Gy$ peak dose. Compared to the range of the protons determined from FLUKA simulations ($4.21\,mm$) there is a systematic offset of $40\,\mu m$ or about 1% of the range, which can not be explained from the statistical uncertainty.

The systematic deviation can originate from the accuracy of the FLUKA simulation, in which assumptions about the materials used (water and Kapton as entry windows) can lead to range uncertainties. However, it is likely that the majority of the systematic deviation is caused in the range evaluation methodology. Although it is common to use the ToF difference between direct signal and secondary signals as a measure of range [29], this is an assumption that can lead to systematic errors. Even without taking into account geometric uncertainties of the entrance window where the reflection happens, it is not straight forward to show that exactly the maxima of the signals mark twice the range. Additionally, it must be mentioned that correlating both signals (direct and reflected) with the same template could cause an additional error in the filtering process. Since the template was generated for the filtering of the direct signal, a sub-optimal fit to the reflected signal is likely, which can cause a shift of the correlation peak. However, in a clinical scenario with a heterogeneous irradiation medium no or at least not such a pronounced reflected signal is to be expected. This topic is therefore not further explored. Instead, the next chapter will discuss how the Bragg peak position information can be extracted exclusively from the direct signal.

3.3 Summary and discussion

In this chapter, experiments exploring the dependency of the ionoacoustic signal on beam and setup specific parameters were carried out on a preclinical $20\,MeV$ proton research beam. From the results of these experiments, ideal beam parameters for the generation of ionoacoustic signals were derived. For optimal signal generation, a maximum possible instantaneous beam current (particles per pulse) is required, which ensures efficient signal generation without having to average many ionoacoustic signals to increase the *SNR* of the signal. In addition, the ideal pulse duration for generating ionoacoustic signals was evaluated. This ideal duration increases with the energy and is between $1\,\mu s - 8\,\mu s$ FWHM for clinically relevant energies ($70\,MeV - 260\,MeV$). It has been shown that signal generation is more efficient if a long pulse is divided into several short pulses of ideal pulse duration, which are subsequently averaged for *SNR* improvement.
To further increase the *SNR* of the ionoacoustic signals, a correlation filter with simulated filter templates was used. This filter is mathematically designed to maximise the *SNR* of signals of known shape [73]. While extensive research was undertaken to detect ionoacoustic signals in the frequency domain [83], the correlation filter approach in time domain shows more robust results since the well known information about the signal shape can be fully exploited. Using the correlation filter, it is possible to visualise ionoacoustic signals at clinically relevant doses and perform range verification with a statistical uncertainty of 1‰ of the total range at only $0.5\,Gy$ dose at the Bragg peak. The deviation between the the measured range and FLUKA Monte Carlo simulations is $40\,\mu m$ or 1% of the range. In this chapter, the filter templates have been created exclusively on the basis of simulations. For a future application of the correlation filter in a clinical setting, it is conceivable that the templates will be based entirely or partly on measurements. Using high integral doses templates in human-like phantoms or water phantoms allows for the generation of templates of high accuracy, which can further increase the *SNR* of the filtered ionoacoustic signals.
Regarding a potential clinical usage of ionoacoustic signals for range verification, the conditions on the beam current and the pulse duration must be met as good as possible. While the demand of a close to ideal pulse duration clearly limits the applicability

of ionoacoustic range verification, more and more proton therapy centres make use of compact superconducting synchrocyclotrons as accelerators, which deliver pulsed beams with pulse durations in the microsecond range, which is close to the ideal pulse duration for ionoacoustics. In Europe alone, there is a synchrocyclotron for proton therapy in Belgium, Italy, Spain and two in France. Additionally, linear accelerators gain increasing interest for proton therapy and are under construction, for example, by AVO/ADAM at CERN [84] providing suitable pulse durations. However, most proton clinics still use isochronous cyclotrons or synchrotrons as proton accelerators [38]. These accelerators deliver quasi-CW beams that are unsuitable for the generation of ionoacoustic signals. Although it is technically feasible to convert a quasi-CW beam into a pulsed beam by means of a chopper, this would mean in practice a serious interference in the beam guidance of running proton centres. Additionally, chopping the beam would reduce the average beam current resulting in substantially longer treatment times.

One possible compensation of the reduced beam current is given by FLASH irradiations, which rapidly gain attention and are extensively investigated as they provide promising results for the reduction of normal tissue reactions in radiation therapy [85]. FLASH irradiation is characterised by a high dose rate ($> 40 Gy/s$) leading to very short irradiation times. Pre-clinical experiments in mice show promising results that normal tissue reactions can be substantially reduced with FLASH irradiation compared to conventional irradiation, while tumour control remains unchanged [85]. The exact biological mechanisms of the FLASH effect are not fully understood at the time of this thesis. It is thus also not clear whether FLASH primarily requires a high average beam current or a high instantaneous beam current to realise the high dose rate. In case of the latter, FLASH and ionoacoustics could be perfectly combined through efficient signal generation for ionoacoustics with simultaneously reduced side effects through the FLASH effect.

Chapter 4

Proton beam range verification under clinical conditions

The content of this chapter is largely based on the publication by the author of the thesis [86], which was published in Physics in Medicine and Biology. Ionoacoustic measurements and the associated range verification were performed at the proton therapy centre 'Centre Antoine Lacassagne' (CAL) in Nice, France. The accelerator in this therapy centre is a synchrocyclotron, which provides nearly ideal pulse durations for ionoacoustic signal generation. The detectors used for the experiments were characterised and calibrated before this experiment was carried out using an optoacoustic setup.

4.1 Materials and Methods

4.1.1 Experimental setup

Experiments under clinical conditions regarding proton beam energy, dose and irradiation phantom were conducted using the Proteus ONE system from IBA (S2C2) [87] installed at the Centre Antoine Lacassagne (CAL). The Proteus ONE uses a synchrocyclotron for the acceleration of protons and has a movable gantry for beam delivery. The synchrocyclotron was operated in service mode, which allows fixed energies and currents to be selected and no clinical irradiation plan needs to be applied.
The accelerator delivers proton energies between $70\,MeV$ and $250\,MeV$ and the beam was characterised at $126\,MeV$, which was the energy most prominently used within the experiments. The accelerator delivers a pulsed proton beam with a repetition frequency of $1\,kHz$ and a Gaussian pulse shape. The duration of the pulse was measured within the experiments to be $FWHM = 3.1\,\mu s \pm 0.4\,mus$. Using an average beam current of $\bar{I} = 1.5\,nA$, the number of particles per pulse was estimated to be 9.4×10^6. According to Monte Carlo simulations the corresponding maximum dose at the Bragg peak in wa-

ter is $2.56\,nGy$ per proton and thus $2.40\,cGy$ per pulse for an energy of $126\,MeV$. For lower energies the number of particles does not change while the dose at the Bragg peak increases slightly due to a sharper Bragg peak caused by reduced range straggling. The shape of the beam in the lateral dimension at the Bragg peak is approximately Gaussian with $FWHM = 12.0\,mm$ in both dimensions.

Trigger

The temporal profile of the beam was measured in real time to be used as a trigger in order to start a ionoacoustic measurement. It was measured with a plastic scintillator (Model: SPD.150.90.50) in combination with a photomultiplier tube (PMT) (Model: 9266KB50) with an operating voltage of $500\,V$. This detector was electromagnetically shielded using aluminium foil and positioned perpendicular to the beam axis at the entrance of the beam to the target. The protons arriving on the target produce practically instantaneous ($< ns$) photons, so-called prompt-gammas, in nuclear reactions. For the position of the scintillator (approx. $5\,cm$) lateral to the beam and its volume ($150\,mm \times 90\,mm \times 50\,mm$), approximately 10^5 prompt-gammas were expected to hit the scintillator according to simulations using TOPAS [45], a Geant 4 based Monte Carlo particle transport simulation program. In the scintillator material, the prompt-gammas are converted into photons of visible wavelength, which in turn trigger electrons at the entrance to the photomultiplier tube by the photoelectric effect. These electrons are amplified by several dynodes in an electron avalanche before a voltage is read out. This PMT-signal is plotted in Fig. 4.1.
The signal of the PMT from a single pulse is plotted in blue and is fitted using a one dimensional Gaussian (red). The trigger threshold was set to $25\,mV$ in order to start a ionoacoustic measurement. For every ionoacoustic measurement its corresponding trigger signal was recorded. To minimise the influence of a possible jitter of the trigger, each trigger signal was fitted retrospectively with a Gaussian (red) and the corresponding ionoacoustic signal was shifted so that the 50% mark of the maximum amplitude within the rising flank of the Gaussian fit marks $t = 0\,s$ of each corresponding ionoacoustic signal.

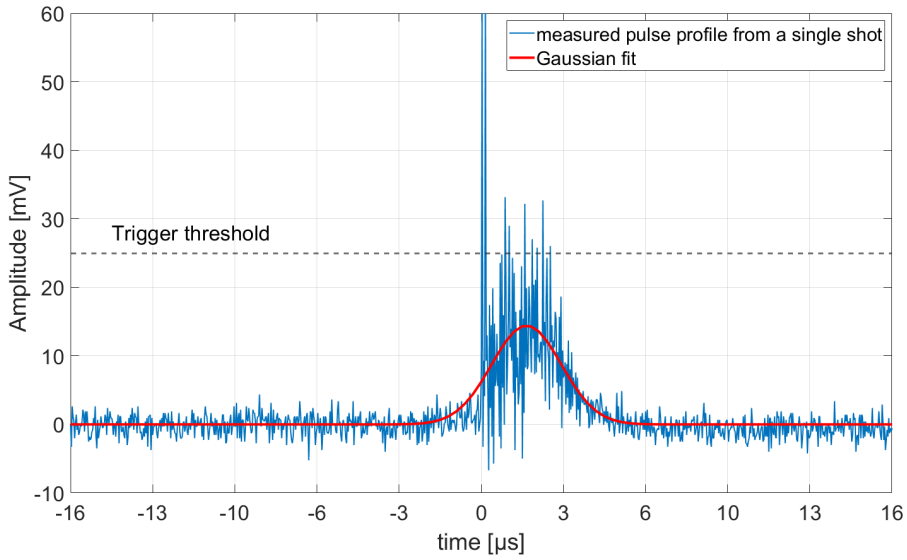

Figure 4.1: Signal obtained from the PMT for a single pulse of the accelerator (blue). The trigger threshold was set to $25\,mV$ in order to start a measurement but was retrospectively shifted so that 50% of the maximum within the rising flank of the Gaussian fit (red) determines $t = 0\,s$. Figure based on Schauer et al. [86].

Measurements using a water phantom

In the first measurement configuration a water tank filled with deionised water was irradiated using single pencil beams of a specific proton energy, which could be arbitrarily adjusted. The ionoacoustic signals were recorded with the Cetacean C305X hydrophone, which has a flat frequency response between $10\,kHz - 250\,kHz$ and a nominal sensitivity (incl. built in pre-amp) of $5.6\,mV/Pa$. The hydrophone was rigidly connected to an Interson GP-C01 ultrasound (US) probe in a custom made holder. The US probe has a variable frequency between $3.5\,MHz - 7.5\,MHz$ and was used at $3.5\,MHz$ to maximise view depth. For image generation, the probe assumes a constant speed of sound of $1.54\,mm/\mu s$. The holder fixes the relative position of the two devices to each other. As the holder was attached to a motorised x-y-z-stage (Nanotec ST4018L), the two devices could be remotely moved, such that both devices could measure in an axial position distal to the Bragg peak. A sketch of the setup is shown in Fig. 4.2 (a) while Fig. 4.2 (b) shows a photo of the custom made holder with the two devices.

The water tank (a) consists of $1.0\,cm$ thick PMMA walls and internal dimensions of $39\,cm \times 39\,cm \times 20.5\,cm$. The water phantom was positioned at a distance of approx.

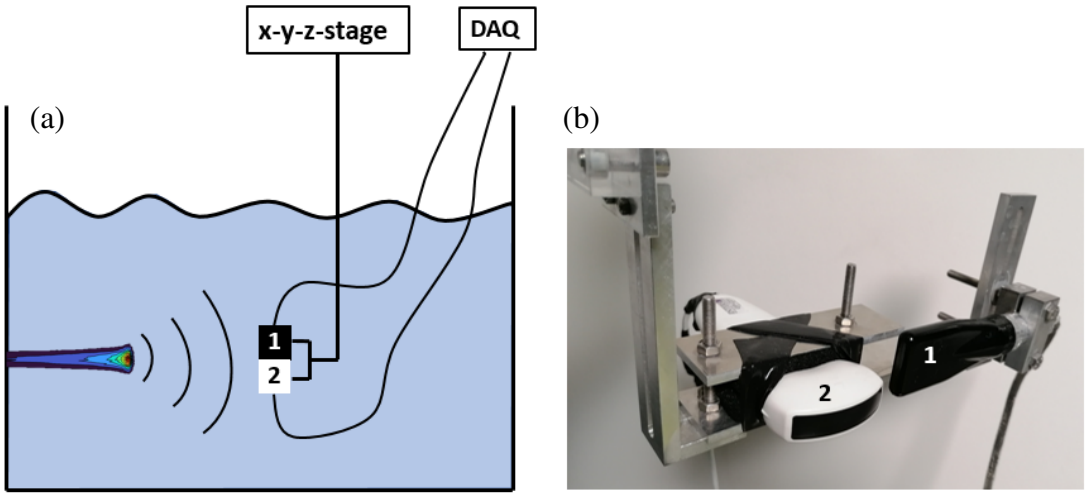

Figure 4.2: A sketch of the setup (a) shows the water phantom, which was irradiated horizontally as indicated by the 2D dose distribution (colour coded). The detection apparatus consists of a sensor to detect the ionoacoustic signals (1), which was rigidly installed with an ultrasound probe (2), which were connected to the data acquisition system (DAQ). The holder for the two devices (b) fixes the relative position of the two devices to each other and can be moved using an x-y-z-stage.

30 cm from the beam nozzle. With the help of the system's integrated laser positioning system, the water phantom was aligned so that the proton beam penetrates the PMMA wall perpendicularly. The holder (b) was also positioned with the integrated laser system axially to the beam path and at a variable distance between $19 - 21\,cm$ from the PMMA wall. Since the relative position of these devices in the holder is known from a calibration measurement (cf. sec. 4.2.4), the two devices could be moved into an axial measurement position alternately.

Within the data acquisition (DAQ), the acoustic signals were first amplified with a $40\,dB$ low-noise-amplifier (HVA-10M-60-B, FEMTO) and then band-pass filtered between $5\,kHz$ - $240\,kHz$ using the Thorlabs EF115 and the Thorlabs EF504. The data was subsequently stored using a 5444D Picoscope with a sampling time of $32\,ns$. The data from the ultrasound probe was acquired using the provided software SimpliVue. In order to combine the data of the two devices retrospectively in the evaluation process an US-image (showing only the PMMA wall) was recorded for every measurement position.

Measurements using an abdominal phantom

In a second configuration, an abdominal phantom from CIRS [88] (Model 057A) was irradiated. It was imaged using X-ray computed tomography (CT), MRI and US and mimics organs (liver, skin, bone, etc.) by different polymers. It also includes several lesions one of which was planned to be irradiated. A sketch of the abdominal phantom provided by the manufacturer showing its internal structure and external dimensions is shown in Fig. 4.3 (a). Additionally the CT image of the abdominal phantom is shown in Fig. 4.3 (b), where, additionally to the target lesion, the planned beam direction and the measurement location are indicated.

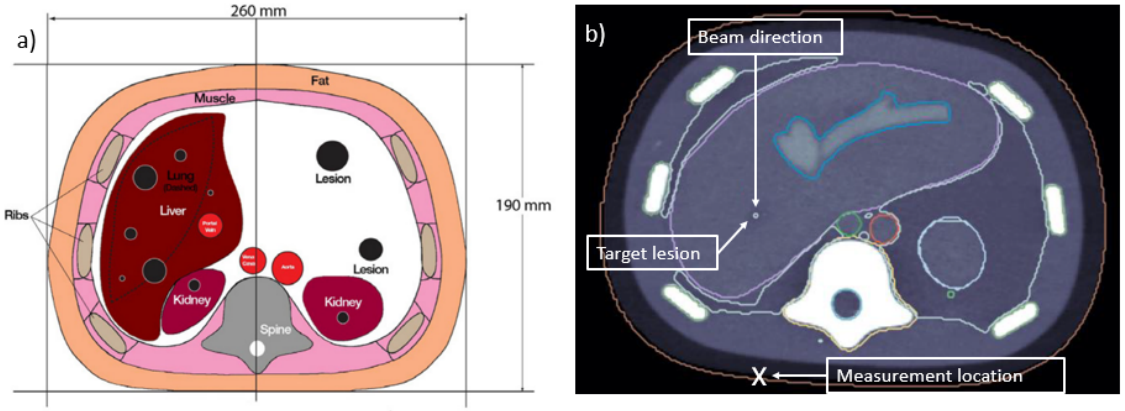

Figure 4.3: A scheme of the CIRS abdominal phantom (a) from its data sheet shows the anatomy and the dimensions of the phantom. The CT-image (b) indicates the planned beam direction, the target lesion and the measurement position. Figure adopted from Schauer et al. [86].

To irradiate the lesion in the liver as planned, the proton energy as well as the positioning of the abdominal phantom relative to the beam were adjusted. To determine the proton energy, the CT image of the abdominal phantom (cf. Fig. 4.3 (b)) was imported into FLUKA [78]. Analogous to a patient's treatment planning, the CT values (Hounsfield units, HU) were converted into the relevant material properties like atomic composition and mass density. Subsequently, the proton beam energy was adjusted to position the Bragg peak in the lesion.

To position the abdominal phantom and the ultrasound probe, the ultrasound device was first acoustically coupled to the abdominal phantom using ultrasonic gel, such that the

planned irradiation lesion was visible in the centre of the ultrasound image. The abdominal phantom and the holder were then aligned distal to the beam using the built in laser alignment system and the movable patient couch, so that the beam enters the phantom at a point, which was previously marked on its skin. Despite this alignment process, small tilts and inaccuracies (as with patient positioning) cannot be completely ruled out. A photo of the setup is shown in Fig. 4.4.

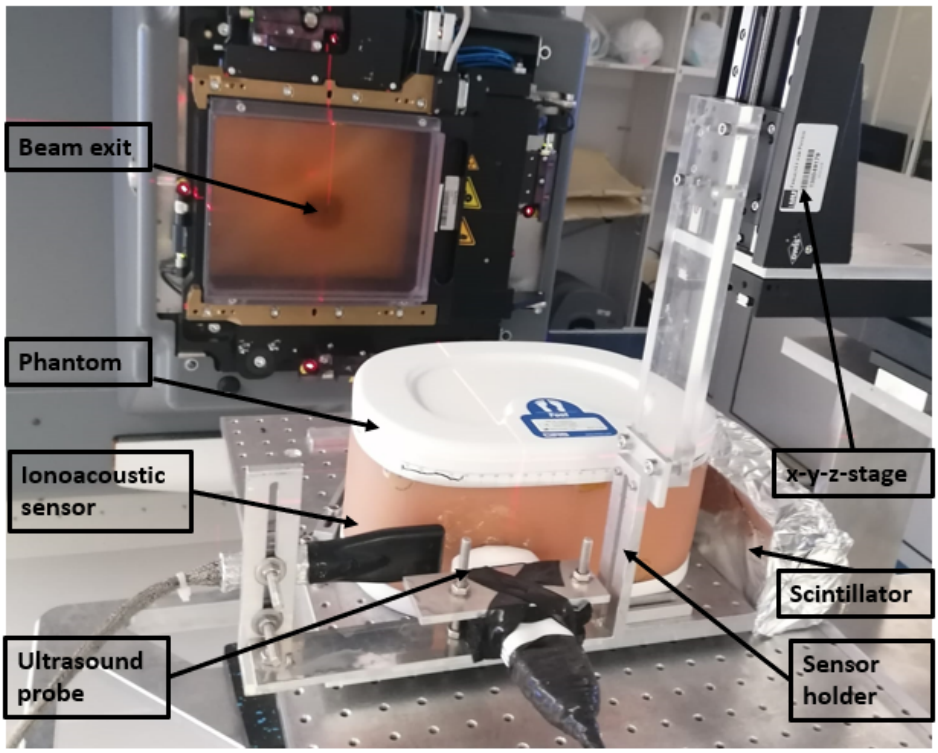

Figure 4.4: An image of the measurement setup shows the realisation of the planned irradiation and measurement setup. The custom made holder is acoustically coupled to the abdominal phantom using ultrasonic gel and mechanically attached to the x-y-z-stage. The scintillator and PMT used for triggering are located on the right of the abdominal phantom and electromagnetically shielded using aluminium foil. Figure adopted from Schauer et al. [86].

The signals were recorded with the exact same data acquisition process (amplifier, filters, digitisation) as in the water phantom configuration (cf. sec. 4.1.1). Since the evaluation of the ionoacoustic signals should be combined with an US image retrospectively, an US-image was taken for every measurement position. To do so the US probe was moved into the axial measurement position using the x-y-z-stage.

The manufacturer of the abdominal phantom additionally provided cylindrical samples with the same materials, which were used within the abdominal phantom. These cylindrical samples have a diameter of $4.0\,cm$ and a thickness of $2.0\,cm$. The speed of sound of the materials was also provided by the manufacturer. In particular the provided fat layer, serves as well characterised heterogeneity and was used in the water phantom measurements.

Additionally, these samples were used to characterise the materials in the phantom with a higher accuracy. A multilayer ionisation chamber (zebra, IBA) was used to determine the stopping power ratio (SPR) relative to water of the heterogeneities. These experimentally determined SPR-values were used post-irradiation to finely tune the Monte Carlo model, which was initially used for the irradiation planning. Additionally to the irradiation planning as described above, it was thus possible to determine a more accurate expected Bragg peak position post-irradiation using the measured SPR-values. This expected Bragg peak position will be used later in this thesis to assess the experimental uncertainties.

4.1.2 Signal processing

The measurements for both configurations (water phantom and abdominal phantom) were evaluated analogously to the method described for the preclinical tandem accelerator (cf. sec. 3). This includes the averaging of several measurements to meet a certain dose limit, the post-processing of the measurements using a correlation filter [75, 89] and associated filter templates (cf. sec. 3.1.2), and the assignment of an *SNR* (cf. sec. 3.1.3). The filter templates should reflect as best as possible the expected signal structure recorded by the sensor and can be described by $F(t) = P_\delta(t) * \frac{\partial H_t(t)}{\partial_t} * TIR(t)$ (cf. eqn. 2.17), where $P_\delta(t)$ is proportional to a spherical surface integration over the dose as seen from the coordinate system of the detector (R, θ, ϕ). $H_t(t)$ is the temporal heating function given by the pulse shape of the accelerator (Gaussian with FWHM = $3.1\,\mu s$) and the TIR is the total impulse response of the hydrophone, which has been measured (cf. 4.1.3).

The 3D dose deposition needed for the calculation of $P_\delta(t)$ was calculated using TOPAS [45]. The number of particles was calculated from the repetition frequency ($1\,kHz$) and

the selected beam current ($1.5\,nA$) and estimated to be 9.4×10^6 particles per pulse. However, for the usage of the dose distribution in the context of the template generation, the number of particles only affects the amplitude of the template, which has no effect on the performance of the correlation filter. The dose was scored in water using a cartesian scoring of $200\,\mu m$. The 3D dose deposition was transferred into MATLAB where it was multiplied with the Grüneisenparameter ($\Gamma = 0.11$ at $20°C$) and the density ($\rho = 998 kgm^{-3}$) of water. Again these parameters do not change the shape but only the amplitude of the template, which does not affect the quality of the correlation filter. The spherical shell integration over the initial pressure $p_0 = \Gamma(R,\theta,\phi)\rho(R,\theta,\phi)D(R,\theta,\phi)$ was evaluated numerically using cubic interpolation in a self written MATLAB script. The sensor position was chosen to match the expected distance from the Bragg peak to the sensor in the experiments ($65\,mm$). The calculation of $P_\delta(t)$ is illustrated in Fig. 4.5 using a simplified (2D) case compared to the actual calculation in 3D.

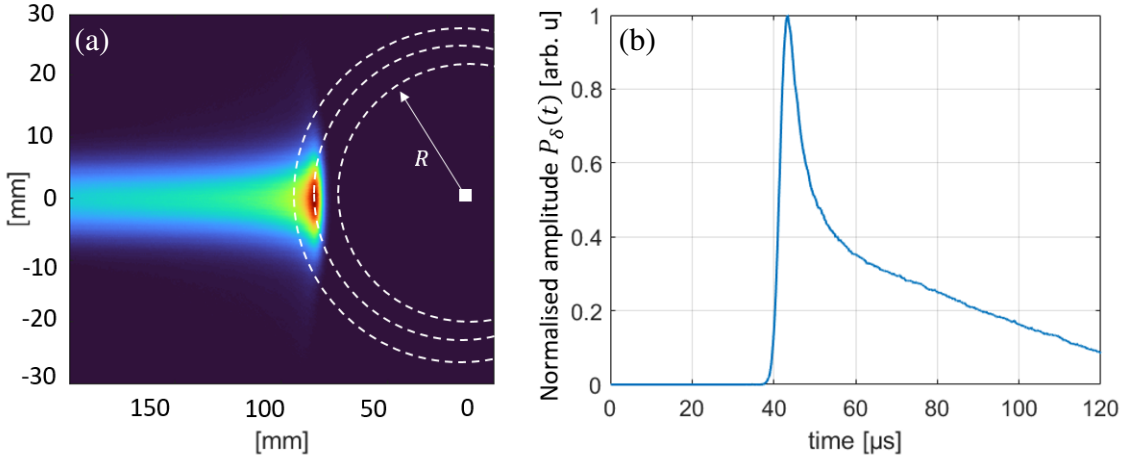

Figure 4.5: The 2D dose distribution (colour coded) and a sensor position (white square) approximating the measurement geometry are given in (a). All pressure contributions $p_0 = \Gamma(R,\theta,\phi)\rho(R,\theta,\phi)D(R,\theta,\phi)$ located on a sphere (white dashed lines) arrive at the detector at the same time where they sum up to form $P_\delta(t)$ (b). Figure adopted from Schauer et al. [86].

The 2D dose distribution as expected in the measurements is colour coded in (a), which specifies additionally the expected measurement location indicated by the sensor position (white square). All pressure contributions associated with the corresponding dose, which is located on a sphere (white dashed lines) at a distance $d = v_s \times t$ arrive at the detector at the same time t where v_s is the speed of sound of the propagation medium ($1.5\,mm\mu s^{-1}$).

Here, they sum up to form $P_\delta(t)$ (b).

The simulation of $P_\delta(t)$ thus maps points within the dose distribution (e.g. peak position or 80% fall-off) to a time point in $P_\delta(t)$. In this particular geometry it was found that the time of flight between the Bragg peak and the sensor ($t = 65\,mm/1.5\,mm\mu s^{-1} = 43.3\,\mu s$) extracted from (a) corresponds to the maximum position of $P_\delta(t)$. It is important to note that as long as an axial measurement configuration is ensured, this mapping is not sensitive to the initial conditions (e.g. distance between Bragg peak and sensor or speed of sound). Only for small distances between the Bragg peak and the sensor relative the the lateral beam extend these two values can deviate.

The resulting $P_\delta(t)$ was subsequently convolved with the derivative of the temporal heating function and the TIR. The TIR changes depending on whether the hydrophone was used in water (measurement configuration I) or with air as backing material (measurement configuration II). Both TIRs were measured using a pre-experiment described in section 4.1.3. The resulting templates only differ in the used TIR and are shown in Fig. 4.6 (a) and (b), respectively.

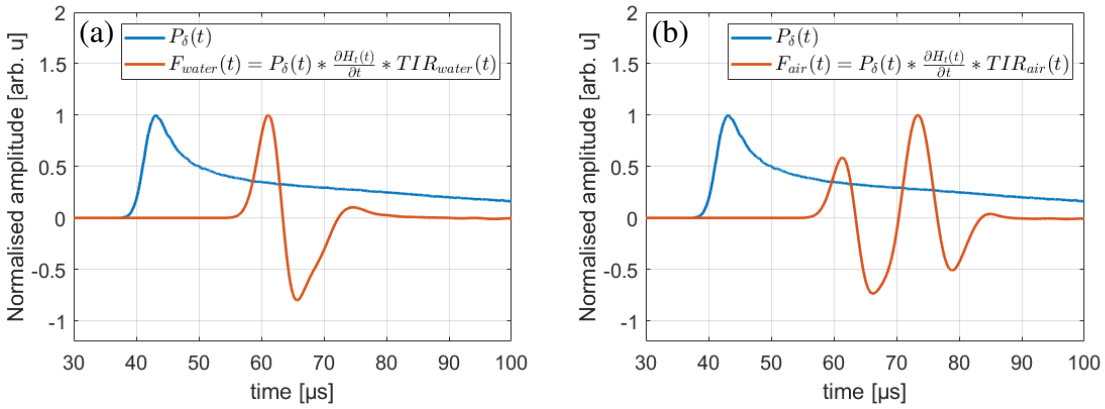

Figure 4.6: The templates (orange) best represent the expected signals for the water phantom measurement (a) and for the abdominal phantom measurement (b). They are calculated by the convolution of $P_\delta(t)$ (blue) with the derivative of the temporal heating function $H_t(t)$ and the total impulse response of the hydrophone $TIR(t)$ in water and air, respectively. Figure based on Schauer et al. [86].

The templates (orange) best represent the expected signal shape to be recorded with the hydrophone and were used for the correlation filter to denoise the measurements recorded in the water phantom (a) and the abdominal phantom (b). The generation of the templates by convolution determines a temporal offset between $P_\delta(t)$ (blue) and the templates. This

offset is fixed by the temporal heating function and the TIR. As the temporal heating function is Gaussian, it is impossible to determine a non-arbitrary starting point or an ending point. A similar argument can be made for the TIR. The temporal offset between $P_\delta(t)$ and the templates is thus no direct physical quantity but depends on these numerical cut-off points. However, for the further course of this thesis, it is just important that the offset is fixed to be able to compare two measurements relative to each other.

4.1.3 Characterisation of the Cetacean C305X hydrophone

The hydrophone used to record the ionoacoustic measurements at CAL was characterised beforehand using an optoacoustic setup. Optoacoustics is similar to ionoacoustics in the sense that a spatially confined energy deposition causes an acoustic wave that can be measured. In contrast to ionoacoustics this energy deposition is caused by photons, typically in the form of a laser, that are absorbed on a target and thereby generate an acoustic wave. However, the expected optoacoustic signal can still be described by $F(t) = P_\delta(t) * \frac{\partial H_t(t)}{\partial t} * TIR(t)$ (cf.eqn. 3.2).

Optoacoustic setup

In order to generate optoacoustic signals, a pulsed laser was absorbed on an aluminium foil target, which was installed inside a water phantom. Two different configurations were used, mimicking the usage of the hydrophone with water and air as backing material, respectively. Sketches of the two setups are shown in Fig. 4.7 (a) and (b) respectively.
For both configurations, a fibre coupled laser diode from Coherent DILAS [90] with a central wavelength of $808\,nm$ (1) was installed. The output power of the laser can be adjusted into pulses of arbitrary pulse shape, duration and repetition frequency with a Fast Modulator FM 45-25 from MPC [91] and a function generator (Rigol DG 1022). In CW operation the laser diode reaches an output power of $30\,W$. The laser was focused with a converging lens ($f = 10\,cm$), before entering the water tank (2) ($39\,cm \times 39\,cm \times 20.5\,cm$) through a $1.0\,cm$ thick PMMA wall. Inside the water tank the beam is focused on an aluminium foil target (3), which was positioned at the focal point of the lens approximately $4\,cm$ behind the PMMA wall. The focus of the laser was approximately $2\,mm - 3\,mm$ in

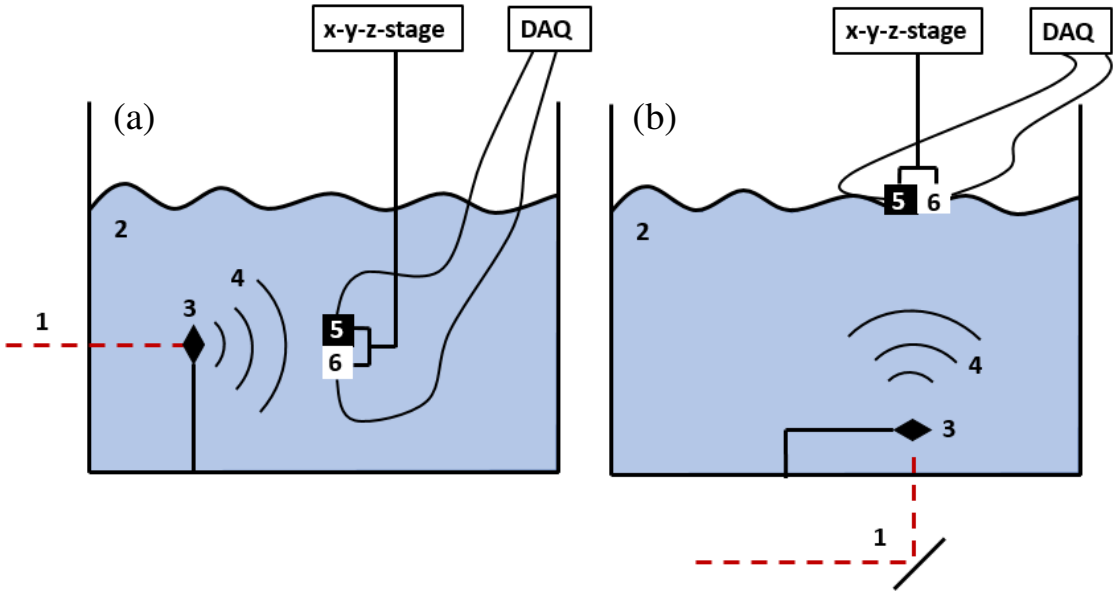

Figure 4.7: Optoacoustic setup used for the generation of optoacoustic signals for two different configurations (a) and (b). A pulsed laser (1) enters the water tank (2) through a 1 *cm* thick PMMA wall before being absorbed on an aluminium foil target (3). The optoacoustic wave is launched (4) and detected by the hydrophone (5), which is permanently installed with the ultrasound probe (6). In (a) the combined holder is operated inside the water tank while in (b) the laser is reflected on a mirror to be directed upwards so that the combined holder can be operated on the water surface.

diameter. A close up photo of the aluminium foil target and the approximate size of the laser spot is shown in Fig. 4.8.

The optoacoustic signals (4) were detected by the Cetacean C305X hydrophone (5), which was rigidly installed with the ultrasound probe (Interson GP-C01) (6) in the metal holding frame as described in Fig. 4.2 (b). The detectors were positioned approximately 65 *mm* from the target on the laser beam axis to mimic the measurement setup using the abdominal phantom (cf. Fig. 4.3).

To ensure an axial measurement location, optoacoustic measurements with fixed pulse duration and laser power were measured in scans, moving the hydrophone in 1 *mm* steps in the directions perpendicular to the beam axis to determine the position where the optoacoustic signal amplitude is maximised. The axial location was determined with millimetre accuracy after fitting the amplitudes of the optoacoustic signals obtained from the scan with a quadratic polynomial. The determination of an axial measurement position using the minimum of the time of flight of the optoacoustic signal is not suitable in this

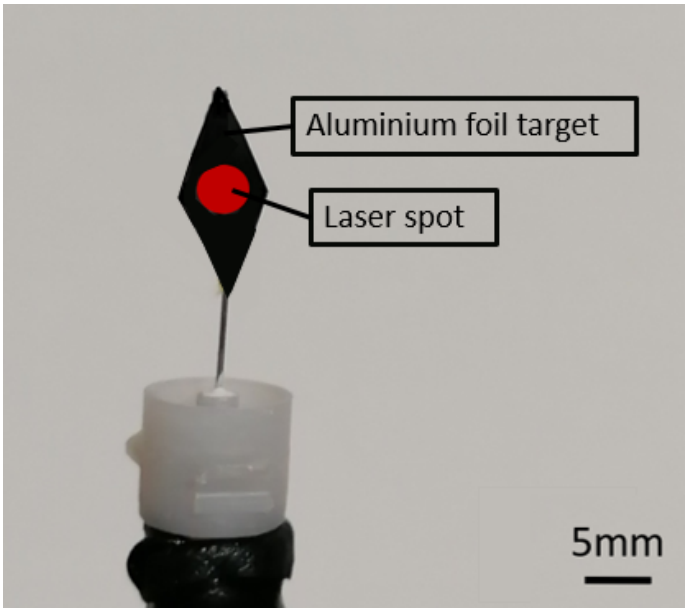

Figure 4.8: Close up of the aluminium foil target with a scale bar and the approximate size of the laser spot focus.

context, since a lateral shift of the ionoacoustic sensor of $1\,mm$ would account for a time of flight difference of only $4\,ns$ which is far below the resolution of the data acquisition ($32\,ns$).

To align the ultrasound device on the beam axis, it was driven with the motor stage to iteratively find the axial measurement position. The height (y-axis) was determined as the point, where the aluminium foil target was displayed as wide as possible, indicating a direct view on its maximum lateral extend (cf. Fig. 4.8). The axial measurement location along the x-axis was determined such that the aluminium foil target was displayed symmetrically along the central line of the ultrasound image (cf. Fig. 4.17).

Care was taken to ensure that the data acquisition in the optoacoustic setups was equal to the data acquisition in the ionoacoustic setups. For the ultrasound probe this includes most importantly the equal central frequency but also settings like contrast or power. The signals recorded with the hydrophone are digitised identically to the ionoacoustic measurements at CAL. This includes the amplification using the $40\,dB$ LNA (HVA-10M-60-B, FEMTO) and subsequent filtering between $5\,kHz - 240\,kHz$ using the Thorlabs EF115 and EF504. The digitisation was achieved using a 5444D Picoscope at a sampling rate of $32\,ns$. Data acquisition was triggered by the function generator that specifies the pulse structure of the laser. The trigger signal was recorded alongside every measurement.

Measurement of the total impulse response of the Cetacean hydrophone

The TIR measurement of the hydrophone was performed for both configurations (cf. Fig. 4.7 (a), (b)) and served to characterise the Cetacean C305X hydrophone. In particular, the measured TIRs were used to generate templates for the ionoacoustic signals, which are used in the data evaluation process (cf. Fig. 4.6).

For the TIR measurements, a long ($30\,\mu s$) rectangular laser pulse was absorbed on the thin aluminium foil target ($50\,\mu m$). As the thickness of the target is small compared to the wavelength of the expected acoustic signal ($> 1\,cm$), it was assumed that $P_\delta(t) = \delta(t)$. If only the turn-on process of the laser is considered, the temporal heating function mimics a Heavyside step function and $\frac{\partial H_t(t)}{\partial t} = \delta(t)$ is also valid and the expected signal results in:

$$p(t) = \delta(t) * \delta(t) * TIR(t) = TIR(t) \tag{4.1}$$

The TIR was directly measured using this technique and the result is shown in Fig. 4.9.

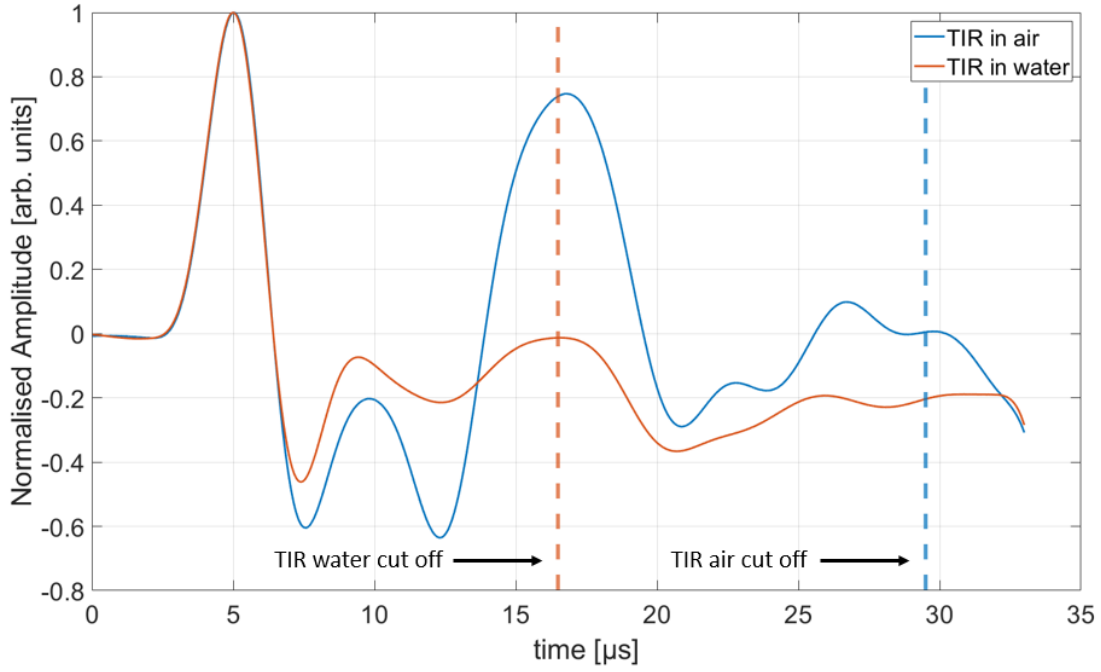

Figure 4.9: The measurement of the TIR with the hydrophone completely submerged in water (cf. Fig. 4.7 (a)) plotted in orange. The measurement of the TIR is plotted in blue (cf. Fig. 4.7 (b)). The TIRs were cut so that only the relevant part, between $0\,\mu s$ and $17\,\mu s$ or $29\,\mu s$, respectively, is taken for further use (dashed lines). Figure based on Schauer et al. [86].

The two TIRs are almost identical at the beginning. For the first peak at about $5\,\mu s$, the hydrophone reacts almost independently of the backing material. However, a pressure wave arriving at the hydrophone is propagating through it, passing the sensitive material, and being reflected on its backside. The amplitude of the reflection is dependent on the difference in impedance between the hydrophone material and the backing material. The large difference in impedance at the back of the hydrophone when used with air as a backing material causes a large part of the acoustic signal to be reflected and recorded a second time by the sensitive material of the hydrophone. This causes the deviations of the signals after the first $5\,\mu s$ and in particular the very pronounced second maximum for the TIR in air at $17\,\mu s$.
In order to use the measured TIRs for template generation for the ionoacoustic signals cut-off points were decided. The cut-off points ($17\,\mu s$ for the TIR in water and $29\,\mu s$ for the TIR in air) were chosen to include the relevant information of the TIRs, but exclude possible acoustic reflections from the PMMA walls. In addition, the points were chosen so that the TIRs smoothly transits to 0 avoiding non-physical jumps in the template.

4.2 Results

The results of the measurements at the CAL synchrocyclotron are divided into three sections. First, the principle of the evaluation is explained before it is used to perform range variation measurements between proton beam of different energies for both measurement configurations (water phantom and abdominal phantom). In the last section, it is shown how a calibration measurement enables the localisation of the Bragg peak. It is demonstrated, how the time of flight of a ionoacoustic signal is used to visualise the Bragg peak position in an ultrasound image of the irradiated region, showing its relative position to anatomical characteristics.

4.2.1 Principle of evaluation

All ionoacoustic measurements were evaluated according to the same principle, which is exemplified by measurements on the CIRS abdominal phantom. Up to 1200 measure-

ments from consecutive proton pulses were averaged to improve the signal to noise ratio of the measurements. As the signal from each pulse was digitised individually with a stable trigger provided by the prompt-gamma-detector (cf. Fig. 4.1), the number of averages and thus the dose contained in a measurement could be chosen retrospectively. For the measurement containing all 1200 averages a total dose of 29 Gy was deposited at the Bragg peak while 50 averages corresponds to a peak dose of 1.2 Gy. The measurement containing 1200 averages and one exemplary signal containing 50 averages are shown in Fig. 4.10 (a) and (b), respectively.

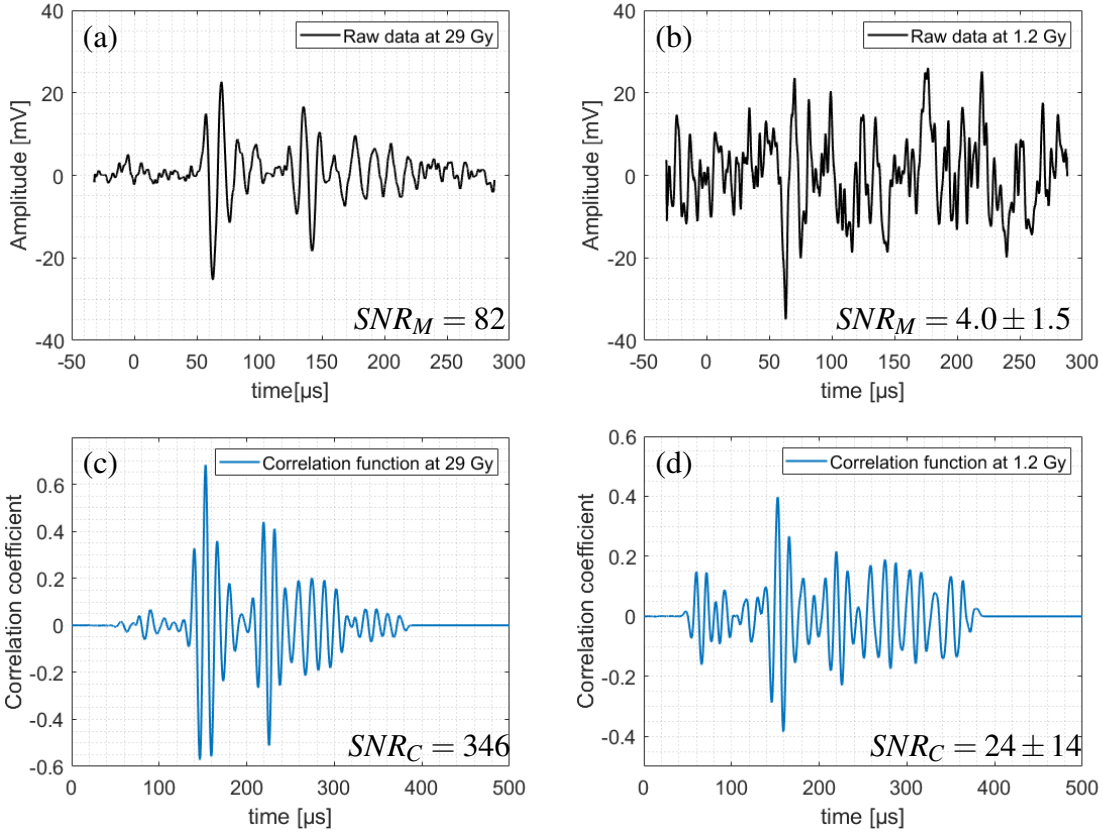

Figure 4.10: 1200-fold averaged ionoacoustic signal measured at the CIRS abdominal phantom (a), containing a total of 1.1×10^{10} protons or a peak dose of 29 Gy. One example showing only 50 averages and therefore reducing the protons and the dose by a factor of 24 is plotted in (b). Both signals were filtered with a correlation filter using filter templates (cf. Fig. 4.6(b)). The results are plotted in (c) and (d), respectively. Figure adopted from Schauer et al. [86].

Fig. 4.10 (a) shows two signals separated from each other in time. The first signal (at approx. 60 μs) is the direct signal. It corresponds to the pressure wave caused by the initial dose distribution after its propagation to the hydrophone. The time of flight of the

direct signal is a measure of the distance between the Bragg peak and the sensor. The second signal (at approx. $130\,\mu s$) is the window signal, which is generated when the protons enter the abdominal phantom. For the evaluation presented here, the window signal is irrelevant. The window signal is difficult to interpret because the waveform is likely overlaid by echoes and reflections. In Fig. 4.10 (b) both these signals are hardly discernible from the noise in the raw data, because of the low averaging number.

The correlation functions in Fig. 4.10 (c) and (d) are obtained after filtering the raw measurements (a) and (b) using the simulated filter templates (cf. Fig. 4.6 (b)). The used templates are designed to represent as best as possible the expected signal shape and are comprised of a combination of simulation and measurement (cf. sec. 4.1.2). The efficiency of the correlation function is particularly evident, when looking at the signals containing only 50 averages (cf. Fig 4.10 (d) versus (b)). Here, at least the direct signal (at $160\,\mu s$) but also the window signal (at $230\,\mu s$) becomes visible. The quality of the signals is quantified in the $SNR_{M,C}$, which has been assigned to the measurements and correlations according to section 3.2.2. For 50 averages, $SNR_C = 24 \pm 14$ gives the mean value of 24 independent evaluations which jitter with the indicated standard deviation. For 1200 averages no uncertainty can be provided, since all averages are included and no statistic is possible.

The systematic shift of the signal position between the raw measurement ($60\,\mu s$) to the signal position in the correlation function ($160\,\mu s$) is determined by the signal position in the template. Correspondingly, the peak position of the correlation function ($160\,\mu s$) can be used to match the original template to the measurement. While the original signal position in the template can be arbitrary, the temporal shift that has to be applied to this original template in order to match it to the signal position in the measurement can be calculated by subtracting the numeric duration of the template (in samples) from the correlation peak position (in samples). While this relationship only holds true for templates that are of same numerical duration as the measurements (as used here), a similar relationship can be found for arbitrary template and measurement durations. The template can therefore be matched to the measurement with the help of the correlation function. This is demonstrated in Fig. 4.11 for the raw signal recorded at the abdominal phantom using all 1200 averages.

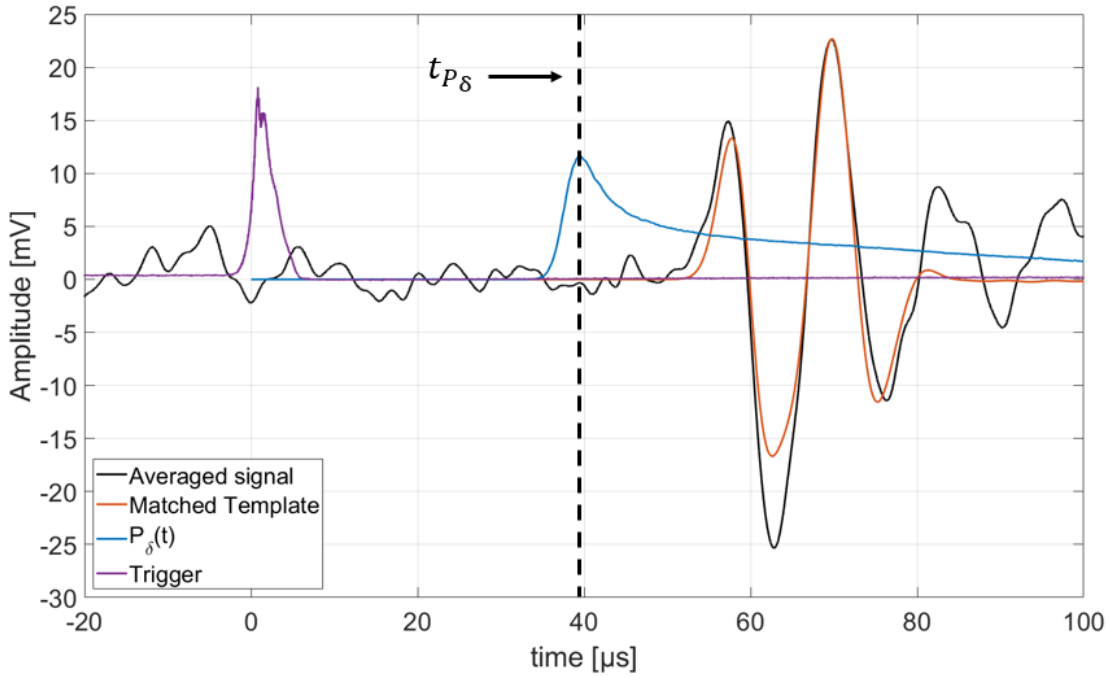

Figure 4.11: The template (orange) is matched to the raw signal (black) with the help of the correlation function. From the template generation the relative position between $P_\delta(t)$ (blue) and the template is known. Its maximum position in time is defined as t_{P_δ}. Additionally the trigger signal is indicated in purple. Figure based on Schauer et al. [86].

The template (orange), was matched to the signal position in the measurement (black) using the peak position of the corresponding correlation function (cf. Fig. 4.10 (c)). From the creation of the template (cf. Fig. 4.6 (b)), the relative position between $P_\delta(t)$ and the template is known and also plotted (blue). Its maximum position in time is defined to be t_{P_δ}. Using the matching procedure, a relative position between the signal and $P_\delta(t)$ can thus be determined. In addition, the trigger signal (purple) is shown, which marks the start of the measurement.

For the matching procedure, the correlation peak of the window signal was excluded from the correlation function as its amplitude can sometimes exceed the correlation peak of the direct signal. This can be justified, since the temporal offset between the direct and the window signal ($70\,\mu s$) accounts for a spatial displacement of approximately $10\,cm$. In a clinical context, the position of the Bragg peak is in any case known better than this from the treatment planning.

It should be reemphasised that the absolute time position of $P_\delta(t)$ has no direct physical

meaning. In particular, the distance between the Bragg peak and the sensor cannot be read as the difference in time of flight between the trigger and $P_\delta(t)$, because the relative position between $P_\delta(t)$ and the template is based on arbitrary cuts of the temporal heating function and the TIR, used for the generation of the template. However, $P_\delta(t)$, or more precisely t_{P_δ}, will be used to perform range variation measurements as demonstrated in the next section and will be calibrated in order to perform Bragg peak localisation (cf. sec. 4.2.4).

4.2.2 Range variation measurements

Range variation measurements were realised by evaluating range differences of beams with different proton energies using ionoacoustic measurements. These measurements are evaluated following the process described in section 4.2.1 for the water phantom (cf. Fig. 4.2) as well as for the abdominal phantom setup (cf. Fig. 4.4). For both setups, the statistical uncertainties are discussed.

Measurements in the water phantom

In the water phantom, ionoacoustic signals for proton energies of $110\,MeV$ and $120\,MeV$ are evaluated and compared with each other. Individual templates with the respective energies were prepared and correlated with the two signals (cf. sec. 4.1.2). Subsequently, according to section 4.2.1, the location of $P_\delta(t)$ was inferred, which serves as the reference time for the evaluation (t_{P_δ}). The signals and the corresponding position of $P_\delta(t)$ are shown in Fig. 4.12. The dose at the Bragg peak indicated in the legend of Fig. 4.12 is obtained from TOPAS simulations using the known number of particles per pulse (9.4×10^6). The dose for the $110\,MeV$ protons ($31\,Gy$ for 1200 averages) is higher than the dose for $120\,MeV$ protons ($30\,Gy$) because of the increased range straggling for higher energies. The raw signals are plotted as solid lines for $E = 110\,MeV$ (black) and $E = 120\,MeV$ (green). The corresponding $P_\delta(t)$ is plotted in the same colour using dashed lines. Its position is determined by the correlation and matching procedure. The arrival time of the signal from the $120\,MeV$ protons reduces relative to the $110\,MeV$ one. Since an axial measurement position was used, the distance between the detector and the Bragg

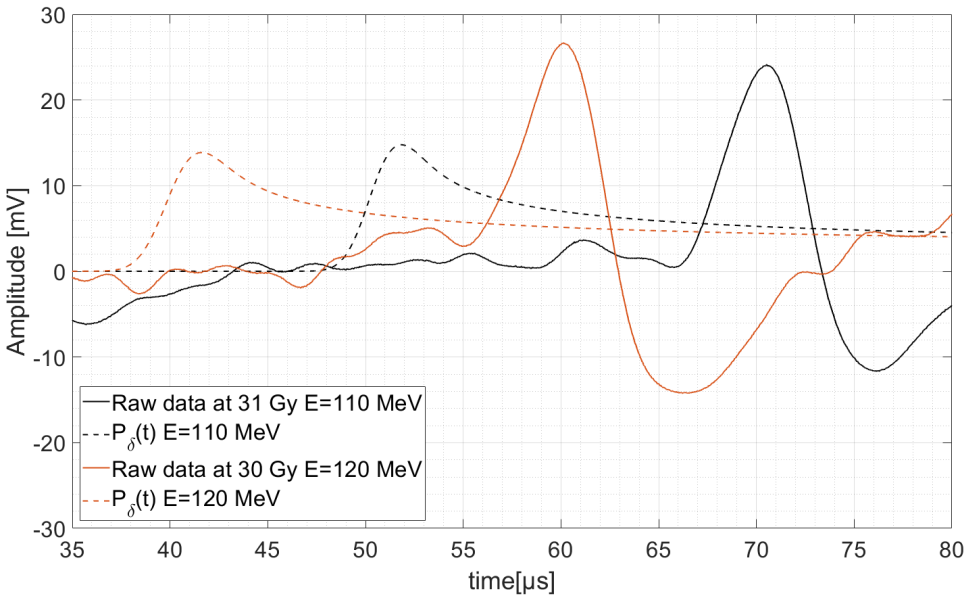

Figure 4.12: Raw ionoacoustic signals (solid) with energies of $E = 110\,MeV$ (black) and $E = 120\,MeV$ including 1200 averages each. For each energy, the corresponding position of $P_\delta(t)$ is plotted with the same colour scheme (dashed lines).

peak reduces for increasing energies (and thus ranges) which results in a shorter time of flight. An equal trend can be observed with the corresponding $P_\delta(t)$.

The differences in time of flight of the different energies are determined by the differences in t_{P_δ} and can be converted into a distance by multiplication with the speed of sound of the water ($1485\,ms^{-1}$ at $21°C$), yielding ΔR_W, where the subscript W is short for 'water'.

$$\Delta R_W = (t_{P_{\delta,110}} - t_{P_{\delta,120}}) \times v_W$$

$$\Delta R_W = (52.03\,\mu s - 41.82\,\mu s) \times 1.485\,mm\mu s^{-1} = 15.16\,mm \pm 0.22\,mm$$

While for these high dose measurements a similar result would have been obtained by determining the time of flight difference directly from the raw signals, this becomes increasingly more difficult as the dose decreases. This is illustrated in Fig. 4.13, showing a dose dependent evaluation of t_{P_δ} for the two different energies. The measurements are evaluated relative to $x_{110} = t_{P_{\delta,110}} \times v_W$, defined after evaluating the $31\,Gy$ measurement from $E = 110\,MeV$ (cf. Fig. 4.12). Additionally, Fig. 4.13 also shows a similar evaluation considering only raw measurements without evaluation of t_{P_δ}. For the raw measurements the position of the zero-crossing of the measurement of $110\,MeV$ was defined as x_{110}.

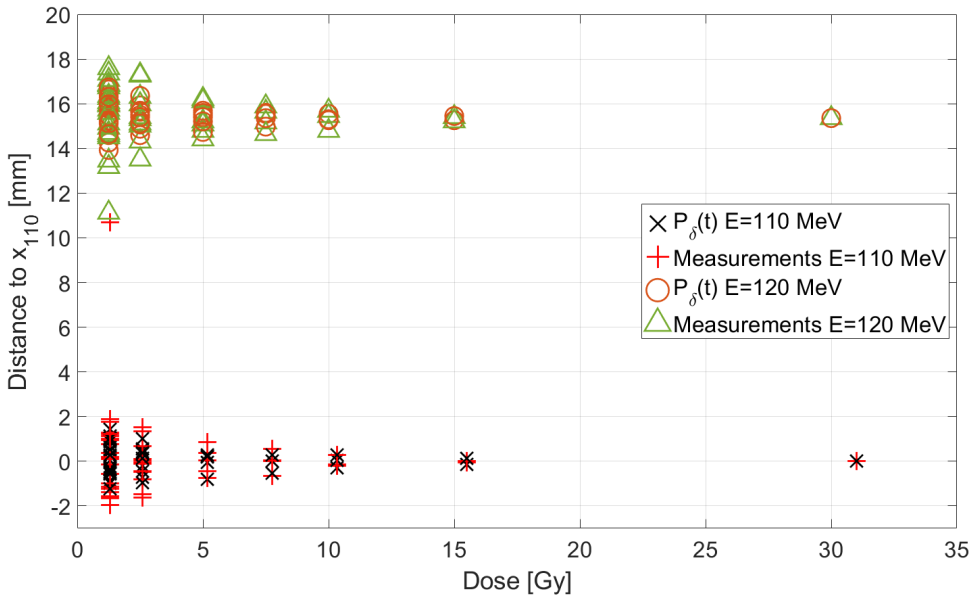

Figure 4.13: Dose dependent scattering of the evaluated time of flights for proton energies of $110\,MeV$ and $120\,MeV$. For both energies t_{P_δ} is plotted together with an evaluation considering only the raw data.

It shows the dose dependent scattering of the data from $110\,MeV$ and $120\,MeV$, starting on the right with one measurement containing all 1200 averages ($31\,Gy$ and $30\,Gy$, respectively) down to 24 measurements containing 50 averages where 50 averages correspond to a peak dose of approximately $1.3\,Gy$. For both energies and independent whether only the raw measurements or t_{P_δ} is considered for the evaluation, the scattering of the data increases for decreasing dose due to the increasing noise floor. The deviation of the markers at $31\,Gy$ and $30\,Gy$, respectively, corresponds to the range difference between the $110\,MeV$ protons and the $120\,MeV$ protons ($15.16\,mm$) as evaluated in Fig. 4.12 using all 1200 averages. The statistical error of the measurements at the lowest dose of $1.3\,Gy$ are summarised in table 4.1.

	$E = 110MeV$		$E = 120MeV$	
	$t_{P_{\delta,110}}$	Raw	$t_{P_{\delta,120}}$	Raw
Standard deviation σ [mm] (μs)	0.79 (0.53)	2.51 (1.69)	0.74 (0.50)	1.50 (1.01)
Max. deviation Δ_{max} [mm] (μs)	1.44 (0.97)	10.80 (7.27)	-1.44 (0.97)	-4.27 (-2.86)
Number of deviations $> 1\,mm$	6	14	3	10

Table 4.1: Quantification of the scattering of the evaluated t_{P_δ} and the raw measurements for a dose of $1.3\,Gy$ and energies of $110\,MeV$ and $120\,MeV$. The distribution of the evaluated time of flights are quantified by their standard deviation (row 1) given in millimetres and microseconds, which can be converted into each other using the speed of sound ($1485\,ms^{-1}$). Additionally, the maximum deviation of a single measurement relative to the mean is indicated by Δ_{max} (row 2) and the number of incidents, where individual measurements deviate from the mean by more than $1\,mm$ (row 3).

From the quantities listed, it can be concluded that the raw measurements perform worse than t_{P_δ} obtained after the correlation and matching procedure. For the raw measurements, it was even necessary to limit the evaluation to the first zero-crossing after the peak position, which was taken from the high dose measurement. Without this information finding the signal in the noise using only the raw measurement is impossible. Even with this information, the high noise at $1.3\,Gy$ produces outliers of $10.8\,mm$ and $-4.27\,mm$, which originate from the fact that the signal has no zero-crossing, since it is always positive ($110\,MeV$) or always negative ($120\,MeV$). This is massively improved by the evaluation of t_{P_δ}, producing no outliers above $2\,mm$ and standard deviations below $1\,mm$. The reason for this improvement originates from the fact that the correlation filter uses the signal shape to determine a time of flight, while for the raw measurements it is necessary to rely on a single point within the measurement. The standard deviations were used to calculate a standard error of the mean for both energies.

$$SEM_{110} = \frac{\sigma_{110}}{\sqrt{24}} = 0.16mm\,(0.11\mu s)$$
$$SEM_{120} = \frac{\sigma_{120}}{\sqrt{24}} = 0.15mm\,(0.10\mu s)$$

The *SEM* is the standard deviation to be expected for the measurements containing all 1200 averages if they were repeated multiple times. The range difference between the two proton beams can thus be calculated to $\Delta R_W = 15.16\,mm \pm 0.22\,mm$, which agrees

with TOPAS simulations (15.06 mm) within the margins of the measurement uncertainty. This shows that it is possible to measure the differences in the range of proton beams with sub-millimetre accuracy using ionoacoustics.

Measurements at the abdominal phantom

Analogous to the water phantom measurements, ionoacoustic measurements on the abdominal phantom were evaluated for proton energies of $E = 126\,MeV$ and $E = 127\,MeV$. The raw signals (solid) containing all 1200 averages (29 Gy) are plotted together with the corresponding $P_\delta(t)$ (dashed) in Fig. 4.14. The filtering and matching procedure to deduce the position of $P_\delta(t)$ was performed using the corresponding template (cf. Fig. 4.6 (b)).

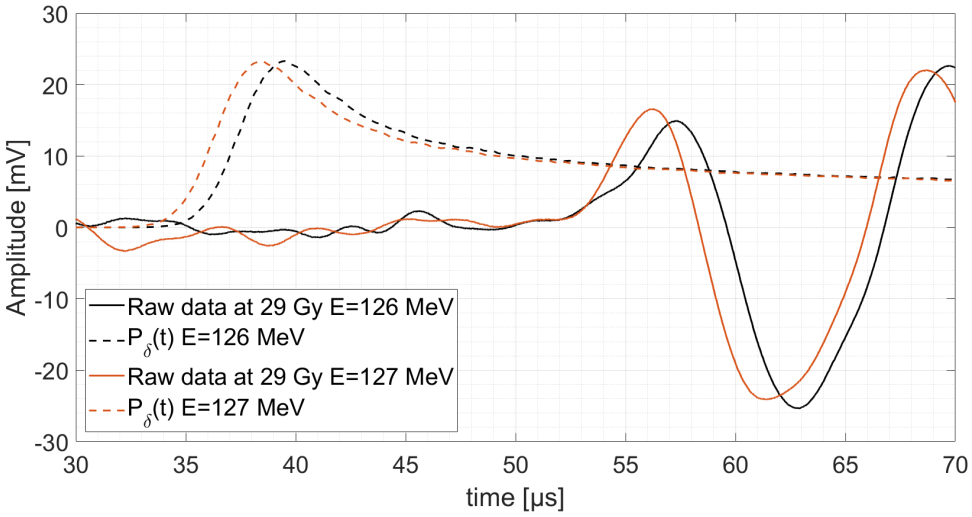

Figure 4.14: Raw Ionoacoustic signals (solid) plotted for $E = 126\,MeV$ (black) and $E = 127\,MeV$, containing 1200 averages or 29 Gy total. The corresponding $P_\delta(t)$ used for time of flight determination are plotted using the same colour scheme (dashed). Figure based on Schauer et al. [86].

From both the raw signals and the corresponding $P_\delta(t)$, the signals from an energy difference of 1 MeV can be well separated at the given dose. The time of flight difference between the energies was evaluated from t_{P_δ} and converted to a distance using the speed of sound within the irradiated region of the abdominal phantom ($v_P = 1540\,ms^{-1} \pm 10ms^{-1}$), which was provided by the manufacturer. The subscript P is short

for 'phantom'.

$$\Delta R_P = (t_{P_{\delta,126}} - t_{P_{\delta,127}}) \times v_P$$
$$\Delta R_P = (39.48\,\mu s - 38.43\,\mu s) \times 1.54\,mm\mu s^{-1} = 1.62\,mm \pm 0.14\,mm$$

A dose dependent evaluation was performed comparing the precision of measurements down to 50 averages or $1.2\,Gy$ peak dose at the Bragg peak maximum. In contrast to the water phantom measurements, the evaluation of the raw measurements was dispensed here in order to maintain clarity. However, similar results were found in which the evaluation of the raw measurements shows a significantly higher scattering compared to t_{P_δ} at low doses. The evaluation for the dose dependent t_{P_δ} is plotted in Fig. 4.15.

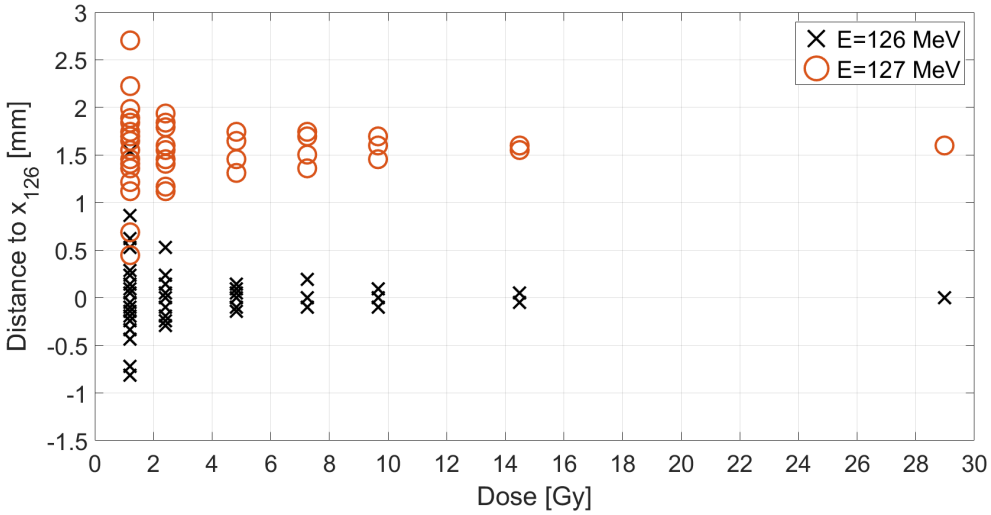

Figure 4.15: Dose dependent scattering of t_{P_δ} for energies of $E = 126\,MeV$ and $E = 127\,MeV$. The data is evaluated relative to $x_{126} = t_{P_\delta} \times v_P$ evaluated for all averages of the signals from $126\,MeV$. Figure adopted from Schauer et al. [86].

The results for the data points at the lowest dose of $1.2\,Gy$ are summarised for both energies in table 4.2.

	$E = 126\,MeV$	$E = 127\,MeV$
Standard deviation σ [mm] (μs)	0.52 (0.34)	0.46 (0.30)
Maximum deviation Δ_{max} [mm] (μs)	1.53 (0.99)	1.1 (0.71)
Number of deviations $> 1\,mm$	1	1

Table 4.2: Quantification of the scattering of the evaluated t_{P_δ} for a dose of $1.2\,Gy$ and energies of $126\,MeV$ and $127\,MeV$. Analogous to the measurements in the water phantom the scattering is quantified by the standard deviation (row 1), the maximum deviation from the mean (row 2) and the number of measurements that deviate more than $1\,mm$ from the mean. The quantities are given in millimetres and, in brackets, in microseconds, where the proportionality constant is the speed of sound in the phantom ($v_P = 1540\,ms^{-1}$).

In table 4.2, it is immediately noticeable that the results regarding all three quantities are smaller than the results presented for t_{P_δ} evaluated for the water phantom measurements (cf. tab 4.1). The reason for this is that the signal on the abdominal phantom is measured with air as backing material. The reflections that are responsible for the second oscillation of the signal give rise to a higher signal energy, which makes it easier to detect using the correlation procedure. In air, the hydrophone acts as a resonating body that extends the signal duration and thus makes it easier to detect.
Analogous to the water phantom measurements, the standard deviations of the data points at $1.2\,Gy$ are used to calculate the SEM.

$$SEM_{126} = \frac{\sigma_{126}}{\sqrt{24}} = 0.11\,mm\ (0.07\,\mu s)$$
$$SEM_{127} = \frac{\sigma_{127}}{\sqrt{24}} = 0.09\,mm\ (0.06\,\mu s)$$

The SEM is the expected standard deviation of the high dose measurement. Including these uncertainties and the uncertainty of the speed of sound provided by the manufacturer ($\Delta v_P = 10 ms^{-1}$) the range difference can be evaluated to be $\Delta R_P = 1.62\,mm \pm 0.14\,mm$. This result agrees with the simulations using TOPAS ($1.60\,mm$) within the calculated uncertainty. This shows that very accurate range differences can be measured using a heterogeneous abdominal phantom and a clinically realistic measurement of the ionoacoustic signals in air.

4.2.3 Robustness of the method

The use of a correlation filter with filter templates for the evaluation of the time of flight of the ionoacoustic signals causes a dependence of the results on the used template. For the best possible evaluation, it is therefore necessary that all three contributions, namely $P_\delta(t)$, $H_t(t)$ and $TIR(t)$, are known with the best possible accuracy. While it can be assumed that both the temporal heating function, i.e. the pulse structure of the accelerator, and the TIR(t) of the detector can be measured with almost arbitrary accuracy, this does not apply to the simulation-based determination of $P_\delta(t)$. Since the beams used for clinical treatment are characterised very accurately in terms of their spatial dose distribution during commissioning, the initial beam parameters such as energy, energy spread and initial beam width are well known and can be accurately taken into account in the simulation of $P_\delta(t)$. The biggest uncertainty in the modelling of the dose distribution is the influence of anatomical heterogeneities, which were partly responsible for range uncertainties in the first place.

Since the dose distribution is an input parameter for the simulation of $P_\delta(t)$, the range uncertainties have an influence on the evaluated results with regard to the time of flight. In order to quantify the robustness of the template against these uncertainties, hypothetical range uncertainties were approximated by the usage of different energies and thus ranges of the protons used for the simulation of $P_\delta(t)$. The approximation of range uncertainties by varying energies is not valid without limitations. Depending on the heterogeneities, their influence on the shape of the dose distribution can not be fully approximated by a varying energy, especially if the heterogeneities are not homogeneous across the lateral extend of the beam. However, as a first approximation, the ionoacoustic signal of $126\,MeV$ protons was evaluated with templates simulated for an energy of $120\,MeV$ and $130\,MeV$, respectively, while the position of the detector in the simulation of $P_\delta(t)$ was kept unchanged. The results are summarised in table 4.3.

Energy used in template simulation [MeV]	120	130
Associated range uncertainty relative to $E = 126 MeV$ [mm]	-9.5	6.5
Difference in the evaluated range relative to $E = 126 MeV$ [mm]	-0.20	0.39

Table 4.3: Robustness of the evaluated range with respect to templates simulated with an energy that purposely differs from the actual energy.

The differences in the evaluated ranges ($-0.20\,mm$ and $0.39\,mm$, respectively) show that the evaluation of the range is very robust against uncertainties in the range of the protons and the sensor position. Relative to the evaluation using the correct proton energy, the range difference in simulation exceeds $6\,mm$ in both cases, while the evaluated ranges deviate by less than $0.4\,mm$. The reason is that the template used for evaluation depends solely on the shape of the underlying dose distribution while the absolute range is not of importance.

In summary, it was demonstrated that a range variation measurement using ionoacoustic measurements achieves sub-millimetre accuracy using clinically relevant dose levels. This was shown not only for a water phantom but also for an abdominal phantom mimicking a realistic patient anatomy. Lastly it was shown that the presented method is robust with respect to range uncertainties, which can cause an error in the simulation of $P_\delta(t)$. This range variation measurement is already applicable in a clinical scenario to determine, for example, range differences of proton beams delivered in different fractions or compare a measured time of flight to a simulation. However, ionoacoustics additionally offers the possibility of absolute Bragg peak localisation, as presented in the next section.

4.2.4 Bragg peak localisation

Regarding a potential clinical usage of ionoacoustic measurements for range verification, it is desirable to not only measure range differences but also absolute Bragg peak locations. To do so, the maximum of P_δ (t_{P_δ}) as obtained from the correlation and matching procedure was calibrated by absolute means, connecting it to a physical distance.

Methodology and calibration

For such a calibration measurement, it is necessary to know the physical distance of the acoustic source to the sensor. This is provided in the optoacoustic setup (cf. sec. 4.1.3), as the acoustic signals are generated by a pulsed laser being absorbed on a thin ($50\,\mu m$) aluminium foil target. The laser can be adjusted with the help of a function generator in pulses of arbitrary shape, duration and repetition rate. Calibration consists of defining a calibration time (t_c) obtained from an optoacoustic signal and a calibration distance or location (x_c).

For the determination of the calibration time, the laser pulse was adjusted to match as accurately as possible the pulse profile of the synchrocyclotron at CAL (Gaussian with FWHM = $3.1\,\mu s$). The trigger was determined by the function generator and matched with the trigger time used to record the ionoacoustic measurements (50% of the rising flank). Depending on whether the sensor is to be calibrated for use in water (calibration setup Fig. 4.7 (a)) or in air (calibration setup Fig. 4.7 (b)), it was positioned accordingly. For both setups a measurement position an axial measurement configuration on the beam axis was ensured (cf. sec. 4.1.3)

In order to make the optoacoustic signals comparable to the ionoacoustic signals, the evaluation process was equalised to the evaluation process of the ionoacoustic measurements. This includes in particular the generation of a template according to $F(t) = P_\delta(t) * \frac{\partial H_t(t)}{\partial t} * TIR$, which was used to filter the measurements. As described, it was ensured as good as possible that $H_t(t)$ and $TIR(t)$ as well as the trigger position match the corresponding quantities from the ionoacoustic measurements. This was ensured not only during the measurement but also in the generation of the templates, for which the exact same $H_t(t)$ and $TIR(t)$ (same numerical vectors) were used. Regarding $P_\delta(t)$, it was assumed that $P_\delta(t) = \delta(t)$, as all photons are absorbed on the thin ($50\,\mu m$) aluminium foil target. While for the optoacoustic signals the correlation filtering process is not necessary to increase the *SNR* of the measurements, it still allows to determine the position of $P_\delta(t)$ relative to the signal position in the measurement. This is the calibration time t_c, which is illustrated in Fig. 4.16.

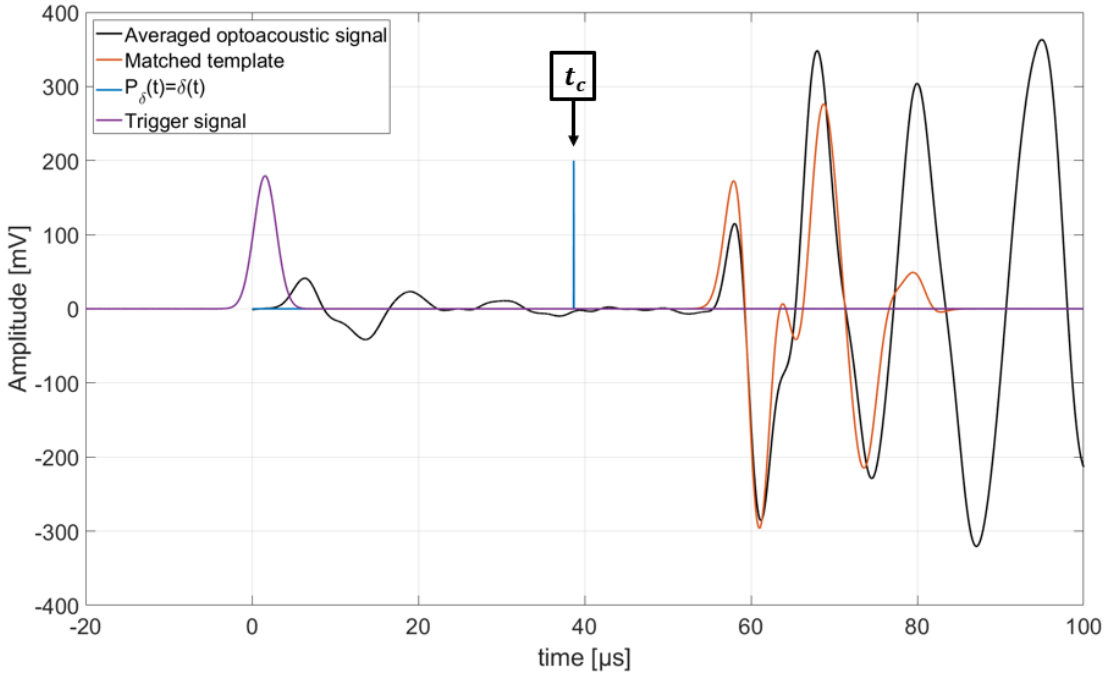

Figure 4.16: Optoacoustic measurement to determine t_c. The raw measurement (black) is matched with the template (orange) using the correlation procedure. The position of $P_\delta(t)$ (blue) is known from the template generation and determines the calibration time. To make this signal comparable to the ionoacoustic measurement, the pulse shape and trigger position (purple) is chosen to match the one from the ionoacoustic measurement as best as possible. Figure adopted from Schauer et al. [86].

The calibration time ($t_c = 38.69\,\mu s$) is deduced from the position of $P_\delta(t)$ (blue), whose relative position to the measurement (black) is known from the correlation and matching procedure using the optoacoustic template (orange). In order to make this calibration time comparable to the ionoacoustic signals, it has to be assumed that the pulse shape and trigger position (purple), the TIR of the detector as well as all secondary electronics (filters and amplifiers) are identical in both (ionoacoustic and optoacoustic) cases. The equal secondary electronics are necessary to exclude relative delays between the optoacoustic and ionoacoustic signals due to filters or amplifiers that are used in one case but not in the other.

To determine the calibration position, the distance between the sensor and the origin of the acoustic signal (aluminium foil target) needs to be measured. One approach is to do this as a physical distance measurement using a scale bar or a caliper starting the measurement at the surface of the hydrophone and ending at the aluminium foil target

(here $x_c \approx 65\,mm$). Once this distance is measured, it can be used to perform range measurements of arbitrary ionoacoustic measurements relative to this calibration position. In order to do so, it is necessary to know the speed of sound that was used within the calibration procedure (v_c) and the speed of sound that the ionoacoustic signal, which is to be evaluated, was subject to (v_s). The time of flight of the ionoacoustic signal is determined as t_{P_δ} as presented in the previous section.

$$x_{BP} - x_c = v_s t_{P_\delta} - v_c t_c \tag{4.2}$$

Since it is known that the maximum position of $P_\delta(t)$ corresponds to the Bragg peak position (cf. Fig. 4.5), the spatial offset calculated on the right side of equation 4.2 corresponds to the difference in distance between the Bragg peak and the aluminium foil target x_c. Using eqn. 4.2, a ionoacoustic signal can thus be used to perform distance measurements between the surface of the hydrophone and the Bragg peak position.

While the speed of sound of the water used in the calibration measurement (v_c) can be measured with high accuracy, this does generally not apply to the speed of sound within a patients body (v_s). This makes this method prone to errors especially if the distance between the Bragg peak and the hydrophone is large, as the uncertainty in the Bragg peak position due to the uncertainty of v_s scales directly with t_{P_δ}. Regarding a clinical use case of this method a second disadvantage arises: The distance between the hydrophone and the Bragg peak itself is not complete in the sense that it does not provide information on the Bragg peak position relative to the tumour or surrounding organs. To do so, the relative position between the surface of the hydrophone and the anatomy of the patient would need to be obtained from a CT or MRI image. This is in principle possible but difficult to realise and prone to errors. Therefore, the Bragg peak position relative to the hydrophone was not evaluated in this work, as it could only be determined with a large uncertainty.

An elegant solution for the indicated disadvantages is given by the combination of the ionoacoustic sensor with an ultrasound probe. Using a custom made holder (cf. Fig. 4.2 (b)), the low-frequency hydrophone ($10\,kHz - 250\,kHz$) was rigidly connected to the high-frequency ultrasound probe ($3.5\,MHz$). Two different devices are necessary because

of the different frequencies utilised in the two devices. The hydrophone is matched to the central frequency of the acoustic signals while the ultrasound probe is used at a frequency that shows the best trade-off between spatial resolution and view-depth. This setup allows to mark the evaluated Bragg peak position in the ultrasound image showing its position relative to the planned irradiation position. To do so, the relative longitudinal position of the two devices, which is fixed by the holding frame, needs to be calibrated. This requires a slightly modified calibration compared to the one presented above. While the calibration time (t_c) stays unaltered, the calibration position (x_c) is obtained from the ultrasound probe positioned in the optoacoustic setup [89]. The calibration position is determined as the position of the aluminium foil target visible in the ultrasound image. This is illustrated in Fig. 4.17.

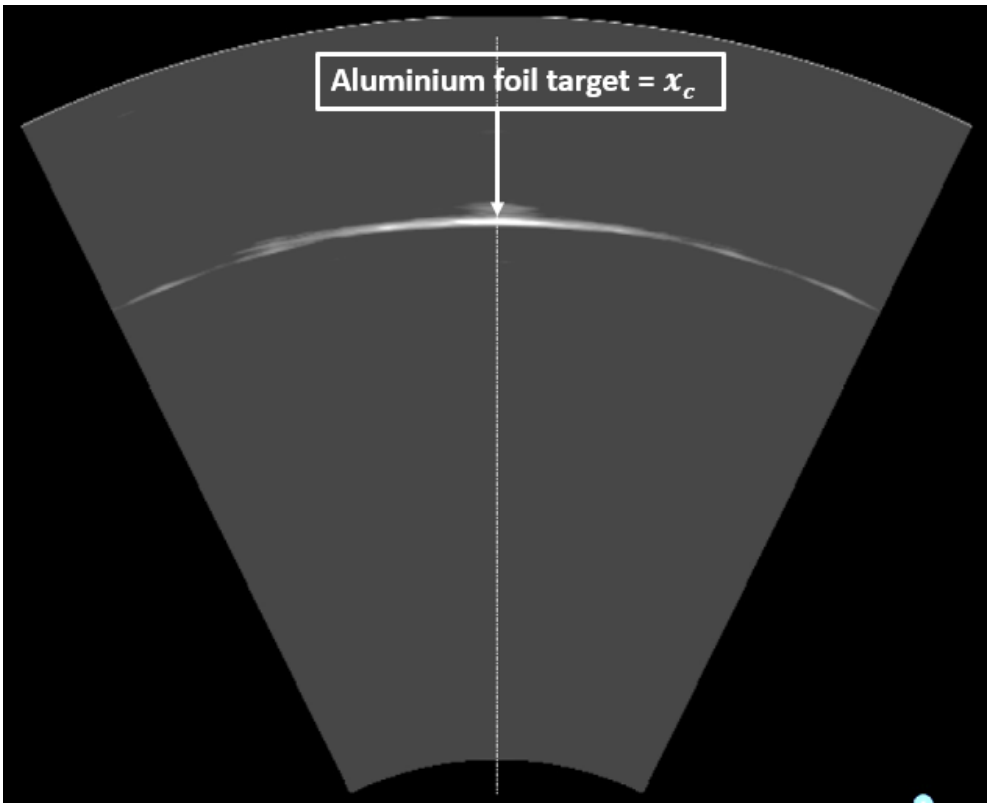

Figure 4.17: Ultrasound image within the optoacoustic setup showing the aluminium foil target, which serves as calibration position x_c. The ultrasound image was recorded at the same position as the optoacoustic measurement from which the calibration time was extracted. Figure adopted from Schauer et al. [86].

The ultrasound image showing the aluminium foil target, which serves as the calibration position x_c, was recorded at the same position as the ionoacoustic measurement from

which the calibration time was evaluated (cf. Fig. 4.16). For both devices an axial measurement position on the beam axis was ensured (cf. sec. 4.1.3). The depth (z-axis) was kept unchanged for the whole calibration procedure including the determination of t_c.
The calibration using the combination of both devices can be performed at an arbitrary distance to the aluminium foil target and in a medium of arbitrary speed of sound assuming that both devices are subject to the same speed of sound (i.e negligible dispersion, which is a valid assumption for water [70]). Assuming the calibration would have been performed in a medium of lower speed of sound, the arrival time of the acoustic signal (or more precisely t_c) would be delayed compared to Fig. 4.16. However, since the ultrasound probe assumes a constant speed of sound of $v_{US} = 1.54 mm\mu s^{-1}$ for image generation, the position of x_c would appear further away from the sensor compared to Fig. 4.17. A similar effect is observed performing a calibration at a different distance. There is thus always a one to one correspondence between the calibration time t_c and the calibration location x_c.
This calibration is used to transfer the time of flight obtained from an arbitrary ionoacoustic measurement (t_{P_δ}) to an ultrasound image recorded at the same location as this ionoacoustic measurement. The ultrasound image thus shows the irradiated region of the phantom. For the transfer of t_{P_δ} to the ultrasound image, the same argument as in the calibration holds: While t_{P_δ} is dependent on the speed of sound between its origin and the sensor, the corresponding regions in the ultrasound image of the irradiated phantom appear stretched or compressed. If it is ensured that the obtained time of flight from the ionoacoustic measurement is scaled with the speed of sound intrinsic to the ultrasound probe (v_{US}), the hydrophone can be seen as a low-frequency extension to the ultrasound probe. Using the calibration position x_c, the Bragg peak position can be marked in the ultrasound image, as if it was visible.

$$\Delta x = x_{BP} - x_c = (t_{P_\delta} - t_c) v_{US} \tag{4.3}$$

If, by chance, $t_{P_\delta} = t_c$, the right side of equation 4.3 vanishes, and the Bragg peak position is the calibration location. Correspondingly, the difference between t_{P_δ} and t_c is a measure for the distance between the Bragg peak and the calibration location. The evalu-

ation relative to the calibration location (x_c) in the combined holder accounts for physical offsets of the two devices in the longitudinal direction or electronic delays caused by built-in amplifiers or filters, which are present in the hydrophone and likely present in the ultrasound probe. The calibration is thus specific to the holder, the sensors, the secondary electronics and the pulse shape.

While the calibration was shown here for the hydrophone being positioned on the water surface, an equal calibration was performed for the holder being submerged in water, leading to a calibration time of $t_c = 44.83\,\mu s$. The absolute value of the calibration position is not of interest, as retrospectively only relative distances within the ultrasound image are evaluated. From the calibration procedure the relative offset of the two devices in the lateral direction was obtained as a by-product and accounts to $\Delta x = 11\,mm$ and $\Delta y = 63\,mm$. These values were used to drive to the measurement location alternately, either measuring ionoacoustic signals or taking an ultrasound image of the irradiated region, respectively.

As a final remark, the fact that both devices are subject to the same speed of sound is based on the assumption that dispersion in the region between the central frequency of the acoustic signals ($80\,kHz$) and the one of the ultrasound probe ($3.5\,MHz$) is negligible. This assumption is reasonable, since it was shown that dispersion in water and haemoglobin solutions mimicking soft tissues is smaller than $1\,ms^{-1}$ for the frequency region of interest [70]. This dispersion would account for less than 1‰ of the evaluated distances, which corresponds to an associated uncertainty of the Bragg peak position of less than $0.1\,mm$ for a distance of $100\,mm$ between the Bragg peak and the sensor.

Proof of concept

To demonstrate the independence of the Bragg peak position from the speed of sound, two ionoacoustic signals were measured in the water phantom using the setup shown in Fig. 4.2 at an energy of $E = 126\,MeV$. First, the signal was measured in pure water before a cylindrical fat layer was positioned in the acoustic path between the Bragg peak and the sensor. The fat layer has a diameter of $4.0\,cm$ and a thickness of $2.0\,cm$. The material of the fat layer is used in the CIRS abdominal phantom and is characterised by the manufacturer with a speed of sound of $(1430 \pm 20) ms^{-1}$. It is therefore expected that the

ionoacoustic signal measured with the fat layer in place is registered at the detector with a delay of $(0.53 \pm 0.20)\,\mu s$ relative to the measurement in pure water at a speed of sound of $1485\,ms^{-1}$ under otherwise identical conditions. The raw signals with and without the fat layer in place are shown in Fig. 4.18.

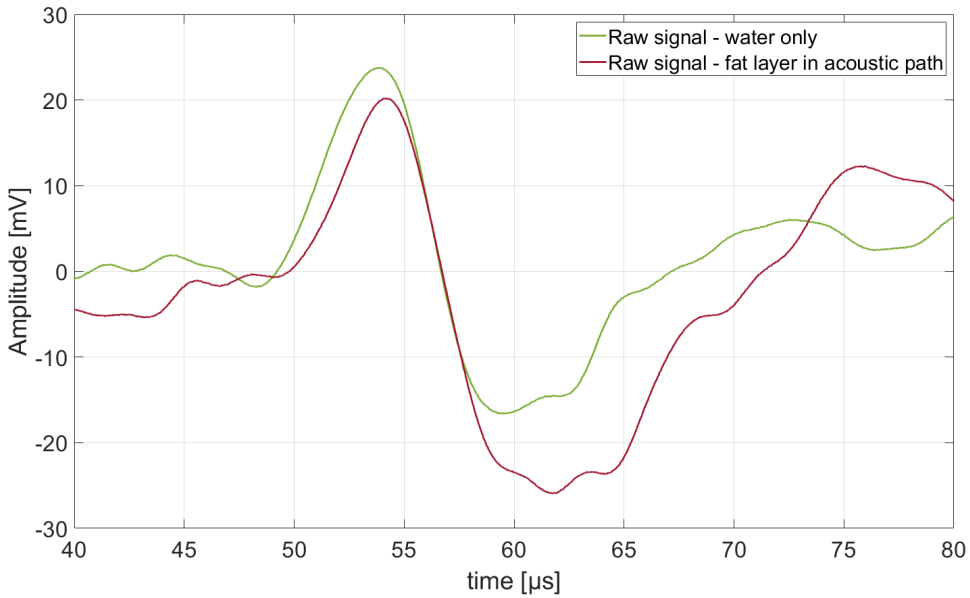

Figure 4.18: Influence of fat layer in the acoustic path. The raw signal has been measured using water only (green) and with a fat layer as a heterogeneity (red) in the acoustic path that is positioned between the Bragg peak and the sensor. Both signals are plotted using 1200 averages or $29\,Gy$ peak dose for identical beam parameters and detector positions.

It can be seen that the signal measured for water only (green) arrives at the detector earlier than the signal measured with the fat layer in the acoustic path (red). However, from the raw signals this delay can vary between $0\,\mu s - 3.0\,\mu s$ depending on the point of reference. Both signals were thus correlated with the same template which was generated for the water phantom measurements (cf. Fig. 4.6 (a)). Using the matching procedure (cf. Fig. 4.11), the corresponding positions of $P_\delta(t)$ relative to the measurements were deduced. Their position was subsequently compared to the calibration time t_c given by $P_\delta(t) = \delta(t)$, which was deduced in section 4.2.4. The calibration time and both $P_\delta(t)$ obtained from the water phantom measurements with (red) and without fat layer (green) in the acoustic path are displayed in Fig. 4.19.

The temporal difference between the two $P_\delta(t)$ is deduced from the respective peak position (t_{P_δ}) and accounts to $\Delta t_{W-F} = 0.57\,\mu s$. The subscript W is short for water, F is short

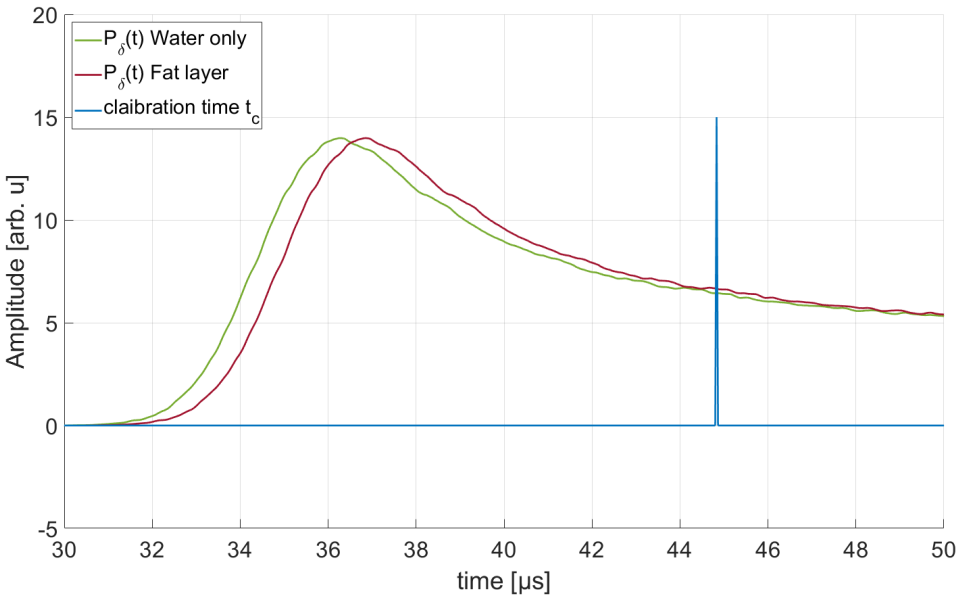

Figure 4.19: The positions of $P_\delta(t)$ for water only (green) and for the fat layer in the acoustic path (red) after performing the correlation and matching procedure for the raw measurements in Fig. 4.18. Additionally, the calibration time t_c is shown (blue) obtained from the calibration using the optoacoustic setup.

for fat and later C is used for calibration. The statistical uncertainty associated with each of the two t_{P_δ} can be approximated by the SEM deduced in section 4.2.2 for the $120\,MeV$ measurement, which is $0.10\mu s$. The measured time shift including uncertainties is thus $\Delta t_{W-F} = (0.57 \pm 0.14)\,\mu s$, which is in good agreement with the expected time shift calculated in the beginning of this section using the geometry and the provided speed of sound of the fat heterogeneity ($(0.53 \pm 0.20)\,\mu s$).

In order to localise the Bragg peak of the respective measurement, ultrasound images were taken at the same position as the ionoacoustic measurements, showing only the PMMA wall (water only measurement) or the fat layer and the PMMA wall. To transfer the time of flight obtained from the two t_{P_δ} to the corresponding ultrasound image, the temporal difference between t_{P_δ} and the calibration time was determined. It accounts to $\Delta t_{W-C} = -8.00\,\mu s$ and $\Delta t_{F-C} = -8.57\,\mu s$. This temporal difference is converted into a distance by multiplication with the default speed of sound of the ultrasound probe ($v_{US} = 1.54\,mm\mu s^{-1}$), which determines the distance to the calibration position x_c (cf. Fig. 4.17).

$$\Delta x_W = \Delta t \times v_{US} \tag{4.4}$$

Δx_W describes the distance between the calibration location x_c and the Bragg peak position as the ultrasound probe would display it. This distance is subsequently converted to pixels using the scale bar provided by the software of the ultrasound probe. In this case, one pixel corresponds to $212.8\,\mu m$. Starting from the calibration position, this distance is then measured on the central axis of the ultrasound image where the negative sign indicates that the Bragg peak position is closer to the sensor, since the time of flight obtained from t_{P_δ} is shorter than the calibration time. This yields the Bragg peak position how it would be displayed in the ultrasound image if it was visible. This is illustrated in Fig. 4.20.

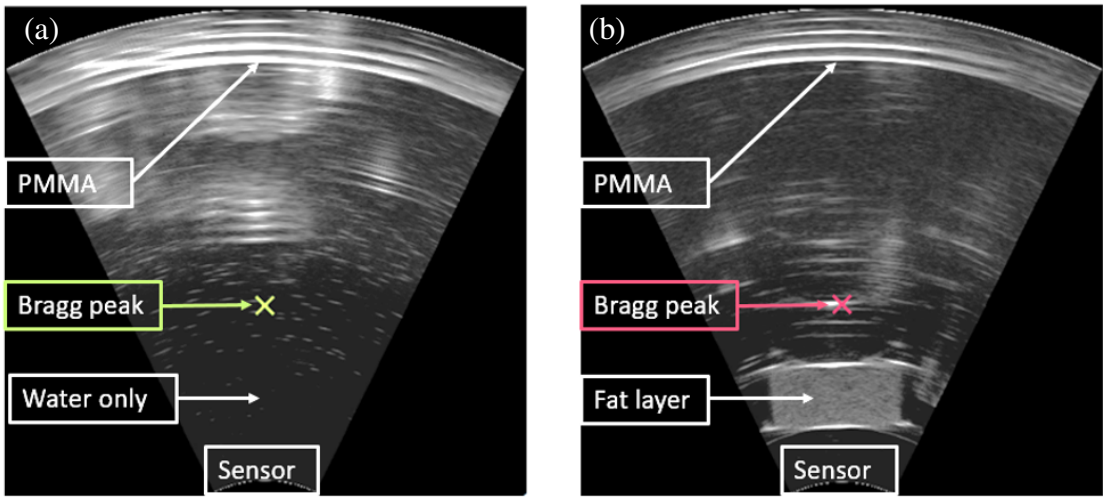

Figure 4.20: Ultrasound image corresponding to the water only measurement (a) and the measurement with the fat layer in place (b). The evaluated Bragg peak positions are indicated by the crosses in green and red respectively. Both ultrasound images show the PMMA wall where the proton beam enters the water phantom.

It shows the ultrasound images for the water only measurement (a) and the measurement with the fat layer in place (b). The evaluated Bragg peak positions are marked in green (water) and red (fat), respectively. In both ultrasound images, the PMMA wall is visible where the beam enters the water phantom.

Since in this case t_{P_δ} differs depending on whether the fat layer was in place or not (cf. Fig. 4.19), the evaluated Bragg peak positions are not identical. This is hardly visible in the ultrasound images, as the difference only accounts to $\Delta x_{W-F} = \Delta t_{W-F} \times v_{US} = (0.88 \pm 0.25)\,mm$, which corresponds to approximately 4.1 ± 1.2 pixels. Because of the slower speed of sound in the fat layer, the Bragg peak position is indicated further

away from the sensor position for the measurement where the fat layer was positioned in the acoustic path. However, this effect affects the PMMA wall in the same way and the distance between the PMMA wall and the sensor is displayed as larger when the fat layer is in place. The distances between the Bragg peak and the PMMA wall are evaluated as $d_{BP-PMMA,Water} = (494.5 \pm 0.7)px$ for the water case and $d_{BP-PMMA,Fat} = (494.6 \pm 0.7)px$. The indicated uncertainty was calculated from the SEM ($0.10\mu s$), which has been converted to a distance by multiplication with v_{US} and subsequently converted to pixels. These two values agree within the given measurement uncertainty, which demonstrates that the distance between the Bragg peak position and the PMMA wall can be consistently evaluated, independent on whether the fat layer was installed or not. It has therefore been shown, that the uncertainty regarding the speed of sound can be compensated, if the calibration is performed in an ultrasound image.

This relative comparison between the measurement using only water and the one with the fat layer works only because the fat layer is only in the acoustic path and thus the speed of sound between the Bragg peak and the PMMA wall is identical in both cases. While the workflow described to transfer the time of flight from a ionoacoustic measurement to an ultrasound image is not limited to heterogeneities in the acoustic path, a verification regarding heterogeneities in the beam path is challenging. On the one hand, heterogeneities in the beam path alter not only the speed of sound but also the range of the proton beam, which prevents the comparability of two measurements with and without heterogeneity in the beam path. On the other hand, distances in two ultrasound images can only be compared if, as here, the speed of sound between the two locations (here: Bragg peak and PMMA interface) is identical.

To deduce a real physical distance between two points within an ultrasound image, the real speed of sound of the media in between the two points of interest needs to be known. For the presented measurements in the water phantom this is provided as the speed of sound of the water between the Bragg peak and the PMMA interface is known ($v_W = 1485 ms^{-1}$ at $21°C$). The real physical distance R between the Bragg peak and the PMMA-water interface can be obtained by:

$$R = d_{BP-PMMA,Water} \times 212.8 \frac{\mu m}{px} \times \frac{v_W}{v_{US}} = (101.5 \pm 0.2) mm \tag{4.5}$$

This value deviates by approximately $2.8\,mm$ from FLUKA Monte Carlo simulations ($104.3\,mm$) indicating that the statistical error given in eqn. 4.5 is insufficient and the measurement was subject to systematic errors.

One systematic error to be addressed in this context is the uncertainty regarding the speed of sound of the water (v_W). While the speed of sound or rather the water temperature was measured during this experiment, a small systematic deviation can cause a big difference in the evaluated range. For example, a deviation of the measured speed of sound by only 1% could change the evaluated range to $R = (102.5 \pm 0.2)\,mm$ accounting for $1.0\,mm$ of range difference. The impact of the uncertainty of the speed of sound becomes large for large distances to be evaluated. With regard to a clinical application, this means that this method works best if the point of reference relative to which the Bragg peak position is evaluated is as close as possible to the evaluated Bragg peak position itself.

The second systematic error to be addressed is associated with the trigger signal. It was retrospectively found that the shape of the trigger signal depends on the irradiated phantom (water or abdominal phantom). Specifically, the Gaussian trigger signal for the measurements in the water phantom was found to be shorter than the measured pulse shape of FWHM = $3.1\,\mu s$. The associated error causes a systematic shift in the starting time of the ionoacoustic measurement $t = 0\,s$. This error is difficult to quantify because it is not clear how exactly the scintillator failed to accurately record the pulse shape. In the case that the originally measured $3.1\,\mu s$ FWHM are also subject to error, this impacts the evaluation process at two additional incidents. On the one hand, the calibration was specifically created for this pulse duration and on the other hand, the pulse duration and shape are also included in the creation of the templates. It is thus likely that this error accounts for a large part of the deviation that explains the discrepancy between measurement and simulation.

Since the time-of-flight measurements are compared with the calibration measurement, a stable trigger alone is no longer sufficient. It is essential to know the entire pulse shape of the accelerator and to record a trigger signal that accurately reflects the pulse shape in order to know the starting time of the measurement ($t = 0\,s$) relative to the pulse shape. It remains to be mentioned that the error associated with the trigger is expected to be drastically reduced, if at all present, in the measurements using the abdominal phantom,

since the trigger signals here accurately reflect the pulse shape of FWHM = 3.1 μs.

Bragg peak localisation using the abdominal phantom

Bragg peak localisation by marking the Bragg peak location in the ultrasound image showing the irradiated region of the abdominal phantom was performed using the same workflow as presented in the in the previous section. The measurement setup was shown in Fig. 4.4. To transfer the time of flight to the ultrasound image all 1200 individual measurements (total dose of 29 Gy) were used, however the statistical uncertainty for 50 averages or 1.2 Gy evaluated in section 4.2.2 holds.

The ionoacoustic signals were recorded in an axial measurement configuration and have already been shown in Fig. 4.10. Additionally, an ultrasound image was taken at the same location as the ionoacoustic measurements, showing the target lesion. The ionoacoustic signal was filtered using a template (cf. Fig. 4.6 (b)) to determine the position of the corresponding $P_\delta(t)$ (cf. Fig. 4.11). The peak position of $P_\delta(t)$ (t_{P_δ}) is compared with the calibration time measured in air (cf. Fig. 4.16). This is illustrated in Fig. 4.21.

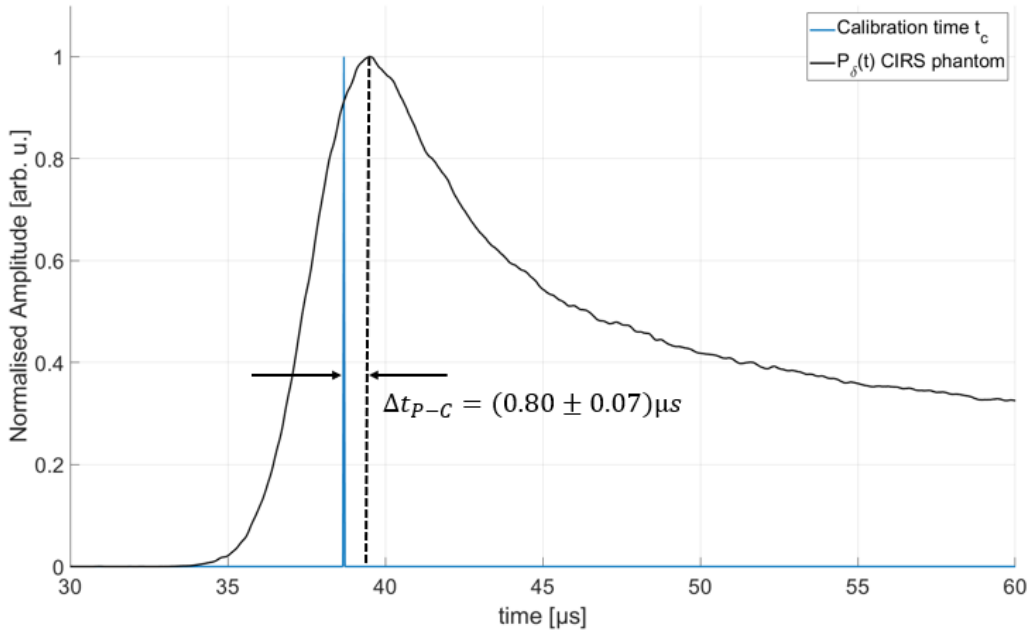

Figure 4.21: Comparison of the temporal difference between peak-position of $P_\delta(t)$ obtained from the CIRS measurements (black) relative to the calibration time (blue). The subscript P is short for 'phantom' while C stands for 'calibration'. Figure based on Schauer et al. [86].

The temporal difference between t_{P_δ} obtained from the measurements at the CIRS abdominal phantom (black) and the calibration time (blue) accounts to $\Delta t_{P-C} = (0.80 \pm 0.07)\,\mu s$. The subscript P is short for 'phantom', while C is short for 'calibration'. The uncertainty indicated is the standard error of the mean (SEM) evaluated in section 4.2.2. The spatial difference between the calibration position (cf. Fig. 4.17) and the Bragg peak position (Δx_P) can thus be calculated.

$$\Delta x_P = \Delta t_{P-C} \times c_{US} = (1.23 \pm 0.11)\,mm \tag{4.6}$$

Analogous to the measurements in the water phantom, this value can be converted to pixels using the built in scale bar ($1\,px \hat{=} 119.1\,\mu m$) and transferred to the ultrasound image, which was recorded at the same position as the ionoacoustic measurement showing the irradiated region and in particular the target lesion. This is displayed in Fig. 4.22. Panel (a) shows the entire ultrasound image of the irradiated region of the abdominal phantom with the target lesion on the central axis. Additionally, the beam direction and the sensor positions are indicated. A red dashed region is marked, which is the region of interest including the target lesion. This rectangle is magnified in (b), showing the originally planned Bragg peak position in treatment planning pre-irradiation (blue), the expected Bragg peak position after fine tuning the treatment planning procedure (cf. sec. 4.1.1) using the measured SPR (red) and the evaluated Bragg peak position from the ionoacoustic measurement (yellow). The contrast of the images was enhanced for better visibility, which is the region they look overexposed in certain areas. The indicated error bars are obtained from the standard deviation of the individual measurements at $1.2\,Gy$ as evaluated in section 4.2.2. The SEM indicating the uncertainty of the $29\,Gy$ measurement only accounts for $90\,\mu m$, which is less than $1\,px$ and therefore not visible.

For the assessment of the systematic deviation the expected Bragg peak position (red) is used rather than the one determined pre-treatment. The deviation between the expected planned Bragg peak position and the one obtained from evaluation deviate by $9\,px$, which can be converted to a real distance using

$$\Delta x_{Planning-Evaluation} = 9\,px \times 119.1 \frac{\mu m}{px} \times \frac{v_P}{v_{US}} \tag{4.7}$$

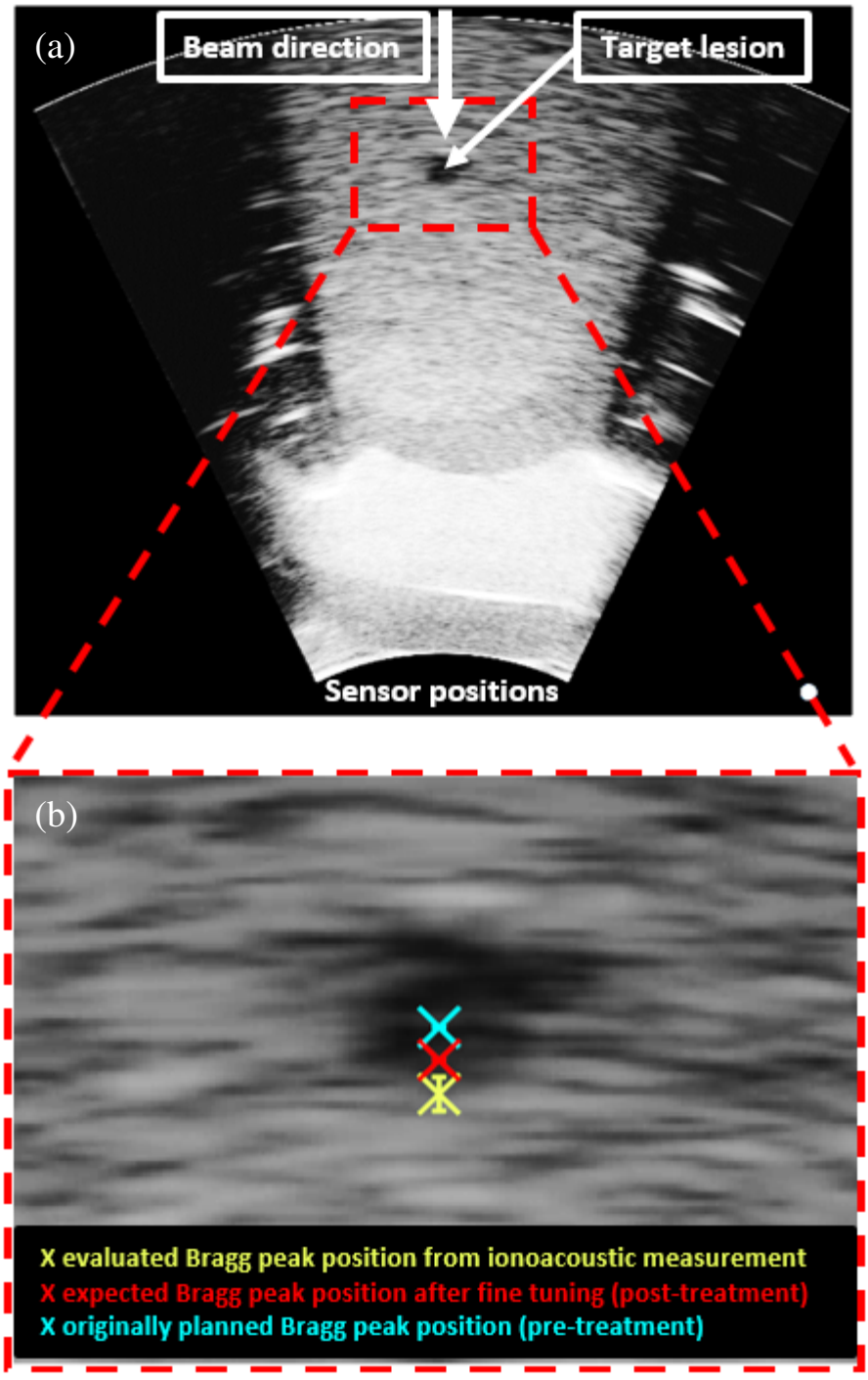

Figure 4.22: The ultrasound image showing the irradiated region of the abdominal phantom and in particular the target lesion (a). Additionally the beam direction and the sensor positions are indicated. The red dashed rectangle shows an inlay which is zoomed in (b). It shows the target lesion with the originally planned Bragg peak position (blue), the expected Bragg peak position after fine tuning the irradiation planning post-irradiation (red) and the evaluated Bragg peak position (yellow) with the error bars indicating the standard deviation found for a dose of $1.2\,Gy$. Figure adopted from Schauer et al. [86].

As the speed of sound within the liver is provided by the manufacturer ($v_P = (1540 \pm 10) ms^{-1}$), the deviation can be calculated to be $(1.07 \pm 0.11)\,mm$ for the $29\,Gy$ measurements or $(1.07 \pm 0.52)\,mm$ for the $1.2\,Gy$ measurements. In contrast to the measurements in the water phantom, the real speed of sound only plays a minor role here since the distance to be evaluated (between the measured and planned Bragg peak position) is small. A deviation of the speed of sound of 1% would in this case only account for approximately $20\,\mu m$. The small deviation between the expected Bragg peak position and the evaluated Bragg peak position shows that ionoacoustic offers the potential to perform Bragg peak localisation with high accuracy. In particular the indicated deviation is substantially smaller that the typical range uncertainty assessed in proton therapy of $1\,mm - 8\,mm$ depending on the tumour location. However, the deviation can not be entirely explained by the statistical uncertainty indicating a systematic uncertainty.

Neglecting systematic errors in the evaluation process of the ionoacoustic measurements, the systematic uncertainty must be attributed to the irradiation planning. The range uncertainty associated with irradiation planning and delivery is typically calculated as at least 3% of the full range plus one additional millimetre [15] for patients which would account for approximately $4\,mm$ in this case given the range of the protons in the phantom ($\approx 100\,mm$). Since in this work irradiation planning was performed for a static phantom and with well characterised materials with respect to their SPR, the uncertainties are expected to be reduced compared to those expected for a human patient. However, it can not be ruled out that a small systematic uncertainty remains. In the assumed case, where the ionoacoustic measurement is not subject to any systematic uncertainties, the information obtained from the ionoacoustic measurement could be used to reduce the proton energy in order to irradiate the lesion.

However at this point, systematic errors in the evaluation process of the ionoacoustic measurements are non-negligible. In this context the trigger signal obtained from the PMT should be addressed once again. Although it is expected that the uncertainty associated with the trigger is drastically reduced compared to the water phantom measurements, it cannot be ruled out that the trigger signal here does also not perfectly represent the actual pulse shape of the proton pulse. As explained in the context of the water phantom measurements, this systematic uncertainty is difficult to quantify.

4.3 Summary and discussion

This chapter has demonstrated the feasibility to use ionoacoustics for range verification in proton therapy. It was demonstrated how, with the use of a correlation filter, a robust time of flight can be extracted from ionoacoustic signals recorded under clinical conditions. These conditions include the proton energy ($126\,MeV$), the deposited dose at the Bragg peak ($1.2\,Gy$) and the irradiated phantom (CIRS abdominal phantom). The used dose of $1.2\,Gy$ is significantly lower than the dose of $2\,Gy$, which is typically applied in a tumour treatment fraction in proton therapy. For signals at $1.2\,Gy$, a statistical uncertainty of approximately $0.5\,mm$ was found, which defines the currently possible accuracy, given the used hardware and signal processing method. Additionally it was shown how the extracted time of flight from a ionoacoustic measurement can be transferred to an ultrasound image recorded at the same location as the ionoacoustic measurement showing the Bragg peak location within the irradiated region of the phantom. To do so the relative position of the two detectors must be fixed and calibrated as performed here using an optoacoustic setup.

Although the used dose of $1.2\,Gy$ is smaller than the typical dose of $2\,Gy$ delivered in one treatment fraction, it is necessary to further improve the signal quality. Depending on the tumour and therapy centre, it is common to irradiate the tumour from different directions, which means that no single lateral pencil beam contains the full dose of $2\,Gy$. A promising starting point for further improving ionoacoustic signal quality is the used hydrophone. In a recently published study by Patch et al. [92], ionoacoustic signals were measured on the same abdominal phantom (CIRS abdominal phantom). Signals containing a dose of less than $0.5Gy$ could be used for evaluation, which indicates that the used sensor is better suited for signal detection than the Cetacean C305X used in this thesis. In the study of Patch et al., the ToF of measured signals were compared with the ToF of simulated signals to infer a difference in distance between the planned irradiation position and the actual irradiation position from the difference in time of flight between measurement and simulation. This method has the disadvantage that the sensor position assumed in the

simulation must be replicated with high accuracy in the physical setup. Additionally the speed of sound assumed in the simulation must match the speed of sound traversed by the ionoacoustic signal. While for the abdominal phantom the speed of sound is known from the manufacturer, this does generally not translate to a clinical scenario. In contrast, the combination of the ionoacoustic sensor with the ultrasound probe as presented in this thesis is very robust against the speed of sound as long as they are equal for both devices. Additionally the absolute sensor position relative to the phantom must not be known, in order to localise the Bragg peak in the ultrasound image. Although the idea of integrating the time of flight obtained from a ionoacoustic measurement into an ultrasound image has been proposed before [29, 93], it has so far only been demonstrated using the same sensor for both ionoacoustic signal detection and the generation of an ultrasound image [93]. This presupposes that the central frequency of the ionoacoustic signals is at least approximately equal to the frequency needed for high quality ultrasound images. This is generally not the case, since the central frequency of the ionoacoustic signal decreases with the energy [75] to a central frequency of approximately $20 kHz$ for the highest clinically used energy of approximately $250 MeV$ while ultrasound images are typically generated using central frequencies between $1 MHz - 20 MHz$. One very important component of this work is thus the combination of the two devices in the custom made holder and the calibration using the optoacoustic setup.

Compared to the arguably most advanced range verification method that uses prompt-gamma emissions, ionoacoustics offers decisive advantages but also comes with certain limitations. Range verification based on the detection of prompt-gamma photons only provides the range of the proton beam in the coordinate system of the detector. This information is incomplete, as the anatomy of the patient relative to the detector is not known and error prone to measure accurately. In a first clinical application of prompt-gamma based range verification [17] the experimenters thus only evaluated range differences between protons beams of different fractions. While this is also possible using ionoacoustics (cf. sec. 4.2.2), it was shown that ionoacoustics additionally offers the potential of Bragg peak localisation relative to the anatomy of the patient in an ultrasound image (cf. sec. 4.2.4). It must be acknowledged at this point that the calculation of the distance between the evaluated Bragg peak position and a reference location in the ul-

trasound image is dependent on the actual speed of sound between the two points. The speed of sound of body tissues is generally not known with high accuracy, which is why an additional error can occur here. The induced uncertainty of the Bragg peak position is directly proportional to the distance between the reference point and the Bragg peak. This distance should thus be minimised. Ideally the reference point would be the lesion itself.

Regarding the precision of the two methods, a similar statistical uncertainty of $0.5\,mm$ was found in a recent study using state of the art prompt-gamma-spectroscopy [19] after evaluating 12 consecutive measurements of the range of a clinical proton beam. In contrast to the evaluation of one single pencil beam, as presented in this thesis, the experimenters designed an irradiation plan to deliver a homogeneous dose distribution of $0.9\,Gy$ to a water phantom with a size of $(10 \times 10 \times 5)cm^3$. While the dose is reduced in comparison with the dose used in this thesis ($1.2\,Gy$), the experimenters defined a merging region including a total of 14 pencil beams to be included in the range uncertainty calculation. The total number of protons included in these 14 pencil beams adds up to a total of 1.7×10^9, which exceeds the number of protons used in this thesis (4.7×10^8) at a dose of $1.2\,Gy$ by a factor 3.5.

The limitations of ionoacoustics concern on the one hand the used accelerator and on the other hand the irradiated tumour. For an efficient ionoacoustic signal generation, the accelerator must operate in a pulsed mode, providing pulses in the microsecond range, with a sufficiently long pulse to pulse separation. The only accelerator type used clinically that matches these demands today is the synchrocyclotron. While an increasing number of synchrocyclotrons are installed, the vast majority of therapy centres use accelerators supplying a quasi-CW beam. As mentioned in the discussion regarding the preclinical experiments (cf. sec. 3.3), it is technically feasible to convert such a beam into a pulsed beam. However, in practice this means a massive intervention in the processes of the therapy centre with the additional consequence that pulsing the beam would reduce the average beam current and therefore prolong treatment times. However, there is an increasing demand on high beam currents in the context of FLASH irradiations ([85]), which benefits ionoacoustics. Additionally, the first LINAC designed for proton therapy is currently under construction at AVO/ADAM at CERN, which would provide suitable

pulse durations for ionoacoustics [40].

Another limitation for ionoacoustics is given by the treatment location. On the one hand a near axial measurement location is desired, which is not always possible dependent on the position of the target in the body. Additionally it must be ensured, that no acoustic blockages (like air) are in the acoustic path, which would hinder the detection of the ionoacoustic signal. For the Bragg peak position to be embedded in the ultrasound image, it must also be possible to image the irradiated region with the ultrasound probe. This concerns tumours, which cannot be imaged using ultrasound because of the high attenuation of dense materials such as bone (brain tumours). The attenuation is frequency-dependent and in the case of bone only affects the ultrasound imaging rather than the detection of ionoacoustic signals, which would still allow a limited use of ionoacoustics. However, on the good side, it should be mentioned that most of the most common tumours can be imaged using ultrasound such as in the breast [94], bladder [95], pancreas [96], uterus [97] and, with reservations, also the intestine [98] and the prostate [99].

Chapter 5

Conclusion and outlook

This work has elaborated the conditions under which range verification in proton therapy based on ionoacoustic measurements is possible. While this work was explicitly supported by experiments with protons, the same findings apply qualitatively to particle therapy in general and are not limited to protons.

In a first experiment using a preclinical tandem accelerator and $20\,MeV$ protons, ideal beam conditions were worked out and extrapolated to clinical energies. In order to be able to compare ionoacoustic signals with each other, a SNR_D was introduced, which represents a measure of the signal quality at a fixed dose. It was found that a maximum SNR_D can be obtained if the proton beam is pulsed with ideal duration. This ideal pulse duration increases with increasing energy and is in the range of $1\,\mu s - 8\,\mu s$ for clinically relevant proton energies. It was also found that the number of protons per pulse must be maximised for ideal signal generation. This finding is independent of the proton energy and is limited by the accelerator. It can be scaled up until, in the best case, the entire dose is deposited in as short a time as possible. As part of the evaluation of the ionoacoustic signals measured at the preclinical accelerator, a signal processing algorithm was developed that maximises the SNR_D of the ionoacoustic signals by correlation with filter templates. The filter templates describe the temporal shape of the signal at the detector and can be simulated, measured, or generated by a combination of the two. This correlation filter enables the visualisation of ionoacoustic signals measured with a clinical relevant dose.

In a follow-up experiment, these findings were applied to ionoacoustic experiments conducted at a clinical proton centre (CAL). Ionoacoustic signals were measured on the skin-like surface of a CIRS 3D abdominal phantom using a single lateral pencil beam with a pulse duration of $3.1\,\mu s$. Using the correlation-based post-processing algorithm, a robust time of flight with an uncertainty of approximately $0.5\,mm$ was extracted for

signals recorded at $1.2\,Gy$. This statistical uncertainty currently limits the accuracy with which range verification using ionoacoustic signals is possible. Ionoacoustics also offers the possibility of transferring the range information into an ultrasound image of the patient. A physical combination of the ionoacoustic sensor with an ultrasound device in combination with a calibration measurement allows the ionoacoustic sensor to be used as a low-frequency extension of the high-frequency ultrasound probe. The systematic deviation between the Bragg peak position as evaluated from the ionoacoustic measurements deviates from the expected Bragg peak position by approximately $1\,mm$. This accuracy is smaller than the typical range uncertainties assessed in clinical treatment planning of $1\,mm - 8\,mm$ depending on the tumour. In this work, the Bragg peak position was marked in the ultrasound image, but the method is in principle not limited to the Bragg peak position, but can be transferred without restrictions to other characteristic points of the dose distribution, e.g. the 80% fall-off. However, it must be emphasised, that shape of the dose distribution itself is not actually measured using the provided method but rather the a priori knowledge about the shape of the dose distribution is used (in the template) to determine its position in the ultrasound image.

Using the combination of ionoacoustics and ultrasound imaging comes with the condition to ensure that there are no acoustic blockages between the dose distribution and the combined sensors, which limits the use cases. One way to overcome this limitation in the future is the establishment of non-axial measurement locations, avoiding acoustic blockages in the way to the dose distribution. The disadvantage of non-axial measurement locations lies in the fact, the lateral position of the Bragg peak in the ultrasound image remains unclear from a single measurement. This disadvantage could be resolved by the usage of multiple detectors. With the aid of a triangulation algorithm, using signals from several measurement locations, not only the range of the proton beam could be accurately determined, but also its lateral position. In order to overcome the typically poorer signal quality in non-axial measurement positions, the noise must be further reduced. A possible starting point in this context is the hardware used, which includes not only the ionoacoustic sensor but also filters, amplifiers and the data acquisition itself.

Another important point for future work is the quantification and subsequent reduction of systematic errors in the evaluation process. At this stage, these errors are difficult to

quantify, because there is no ground truth measurement with which the Bragg peak information obtained from ionoacoustic measurements can be compared. Simulations such as the ones used in this thesis have only limited applicability, as the error-proneness of such simulations is part of the reason for the range uncertainty in proton therapy in the first place. It is therefore necessary to record ionoacoustic measurements in a dosimetric phantom in which the Bragg peak position in the phantom can be measured with high accuracy and thus serves as a comparative value for the ionoacoustic measurements. If possible sources of potential systematic errors can be found and eliminated, ionoacoustic range verification has the potential to provide sub-millimetre information regarding the Bragg peak positions relative to anatomical characteristics visible in the ultrasound image. This incorporation of the Bragg peak information in an ultrasound image showing the anatomy of the patient is the main advantage of ionoacoustics over other range verification approaches.

The localisation of the Bragg peak relative to anatomical characteristics or ideally the lesion offers the possibility to improve the conformity of the irradiated volume to the tumour volume and thus reduce side effects in proton therapy. In a first step towards clinical application, it is likely that ionoacoustics will serve as a quality assurance tool during irradiation. By visualising the irradiation position in the ultrasound image, it is possible to check whether the irradiated position coincides with the planning or whether the position deviates strongly from the planning. In the latter case, the irradiation can be interrupted and a new treatment planning can be initiated. In a second step of clinical applicability, it is conceivable that ionoacoustics will be used to perform adaptive treatment planning. In this context, it is plausible that a high-dose irradiation is planned in the centre of the tumour ensuring room for error. Using the visualisation in the corresponding ultrasound image with a ionoacoustic measurement, an adaptive irradiation could be applied in which energy changes are planned in order to irradiate the tumour homogeneously, starting from the initially irradiated location. Regarding the typical range uncertainties in current state of the art proton therapy (between $1\,mm - 8\,mm$ depending on the tumour location), ionoacoustics offers the potential to reduce these uncertainties substantially.

List of Publications and Patents

Jannis Schauer et al. “Proton beam range verification by means of ionoacoustic measurements at clinically relevant doses using a correlation-based evaluation”. In: *Frontiers in Oncology* 12 (2022), p. 5055.

Jannis Schauer et al. “Range verification of a clinical proton beam in an abdominal phantom by co-registration of ionoacoustics and ultrasound”. In: *Physics in Medicine & Biology* 68.12 (2023), p. 125009.

HP Wieser et al. “Experimental demonstration of accurate Bragg peak localization with ionoacoustic tandem phase detection (iTPD)”. In: *Physics in Medicine & Biology* 66.24 (2021), p. 245020.

Matthias Sammer et al. “Normal tissue response of combined temporal and spatial fractionation in proton minibeam radiation therapy”. In: *International Journal of Radiation Oncology* Biology* Physics* 109.1 (2021), pp. 76–83.

Annique C Dombrowsky et al. “Acute skin damage and late radiation-induced fibrosis and inflammation in murine ears after high-dose irradiation”. In: *Cancers* 11.5 (2019), p. 727.

Jannis Schauer et al. *Matched filter in ionoacoustic signal processing for ion beam range determination and dosimetry*. Patent number: 22 159 975.6. 2022.

References

[1] Freddie Bray et al. “The ever-increasing importance of cancer as a leading cause of premature death worldwide”. In: *Cancer* 127.16 (2021), pp. 3029–3030.

[2] ML Sautter-Bihl and M Bamberg. “Strahlen für das Leben”. In: *Im Auftrag der Deutschen Gesellschaft für Radioonkologie* 6 (2015), p. 28.

[3] Michael Wannenmacher, Jürgen Debus, and Frederik Wenz. *Strahlentherapie*. Springer-Verlag, 2007.

[4] Joseph Sia et al. “Molecular mechanisms of radiation-induced cancer cell death: a primer”. In: *Frontiers in cell and developmental biology* 8 (2020), p. 41.

[5] Rolf Sauer. *Strahlentherapie und Onkologie. 5. Auflage*. 2010.

[6] Jin-song Wang, Hai-juan Wang, and Hai-li Qian. “Biological effects of radiation on cancer cells”. In: *Military Medical Research* 5.1 (2018), pp. 1–10.

[7] Cyrus Chargari et al. “Brachytherapy: An overview for clinicians”. In: *CA: a cancer journal for clinicians* 69.5 (2019), pp. 386–401.

[8] Wolfgang Schlegel and Josef Bille. *Medizinische Physik*. Springer, 2018.

[9] Robert R Wilson. “Radiological use of fast protons”. In: *Radiology* 47.5 (1946), pp. 487–491.

[10] James M Slater. “From X-rays to ion beams: a short history of radiation therapy”. In: *Ion Beam Therapy*. Springer, 2012, pp. 3–16.

[11] *Particle Therapy Co-Operative Group https://www.ptcog.ch/index.php/patient-statistics*.

[12] Antony J Lomax et al. “A treatment planning inter-comparison of proton and intensity modulated photon radiotherapy”. In: *Radiotherapy and Oncology* 51.3 (1999), pp. 257–271.

[13] M Goitein and M Jermann. “The relative costs of proton and X-ray radiation therapy”. In: *Clinical Oncology* 15.1 (2003), S37–S50.

[14] SE McGowan, NG Burnet, and AJ Lomax. "Treatment planning optimisation in proton therapy". In: *The British journal of radiology* 86.1021 (2013), pp. 20120288–20120288.

[15] Harald Paganetti. "Range uncertainties in proton therapy and the role of Monte Carlo simulations". In: *Physics in Medicine & Biology* 57.11 (2012), R99.

[16] Shikui Tang et al. "Improvement of prostate treatment by anterior proton fields". In: *International Journal of Radiation Oncology* Biology* Physics* 83.1 (2012), pp. 408–418.

[17] Christian Richter et al. "First clinical application of a prompt gamma based in vivo proton range verification system". In: *Radiotherapy and Oncology* 118.2 (2016), pp. 232–237.

[18] Joost M Verburg and Joao Seco. "Proton range verification through prompt gamma-ray spectroscopy". In: *Physics in Medicine & Biology* 59.23 (2014), p. 7089.

[19] Fernando Hueso-González et al. "A full-scale clinical prototype for proton range verification using prompt gamma-ray spectroscopy". In: *Physics in Medicine & Biology* 63.18 (2018), p. 185019.

[20] Antje-Christin Knopf and Antony Lomax. "In vivo proton range verification: a review". In: *Physics in Medicine & Biology* 58.15 (2013), R131.

[21] Katia Parodi and Jerimy C Polf. "In vivo range verification in particle therapy". In: *Medical physics* 45.11 (2018), e1036–e1050.

[22] Katia Parodi et al. "Patient study of in vivo verification of beam delivery and range, using positron emission tomography and computed tomography imaging after proton therapy". In: *International Journal of Radiation Oncology* Biology* Physics* 68.3 (2007), pp. 920–934.

[23] Xuping Zhu and Georges El Fakhri. "Proton therapy verification with PET imaging". In: *Theranostics* 3.10 (2013), p. 731.

[24] L Sulak et al. "Experimental studies of the acoustic signature of proton beams traversing fluid media". In: *Nuclear Instruments and Methods* 161.2 (1979), pp. 203–217.

[25] Yoshinori Hayakawa et al. “Acoustic pulse generated in a patient during treatment by pulsed proton radiation beam”. In: *Radiation Oncology Investigations* 3.1 (1995), pp. 42–45.

[26] Katia Parodi and Walter Assmann. “Ionoacoustics: A new direct method for range verification”. In: *Modern Physics Letters A* 30.17 (2015), p. 1540025.

[27] K Stantz, F Alsanea, and V Moskvin. “TH-C-144-01: BEST IN PHYSICS (THERAPY)–Use of Radiation-Induced Ultrasound to Image Proton Dosimetry”. In: *Medical Physics* 40.6Part33 (2013), pp. 546–546.

[28] Kevin C Jones et al. “Experimental observation of acoustic emissions generated by a pulsed proton beam from a hospital-based clinical cyclotron”. In: *Medical physics* 42.12 (2015), pp. 7090–7097.

[29] W Assmann et al. “Ionoacoustic characterization of the proton Bragg peak with submillimeter accuracy”. In: *Medical physics* 42.2 (2015), pp. 567–574.

[30] Kevin C Jones, Chandra M Seghal, and Stephen Avery. “How proton pulse characteristics influence protoacoustic determination of proton-beam range: simulation studies”. In: *Physics in Medicine & Biology* 61.6 (2016), p. 2213.

[31] Bradley E. Treeby and B. T. Cox. “k-Wave: MATLAB toolbox for the simulation and reconstruction of photoacoustic wave fields”. In: *Journal of Biomedical Optics* 15.2 (2010), p. 021314. ISSN: 10833668. DOI: 10.1117/1.3360308.

[32] Sebastian Lehrack et al. “Submillimeter ionoacoustic range determination for protons in water at a clinical synchrocyclotron”. In: *Physics in Medicine & Biology* 62.17 (2017), p. L20.

[33] Stephan Kellnberger et al. “Ionoacoustic tomography of the proton Bragg peak in combination with ultrasound and optoacoustic imaging”. In: *Scientific reports* 6.1 (2016), pp. 1–7.

[34] Dieter Schardt, Thilo Elsässer, and Daniela Schulz-Ertner. “Heavy-ion tumor therapy: Physical and radiobiological benefits”. In: *Reviews of modern physics* 82.1 (2010), p. 383.

[35] *mll operating pricnciple, https://www.mll-muenchen.de/tandem/besucherinfo/vortrag2017.pdf*.

[36] Hywel Owen, Antony Lomax, and Simon Jolly. “Current and future accelerator technologies for charged particle therapy”. In: *Nuclear Instruments and Methods in Physics Research Section A: Accelerators, Spectrometers, Detectors and Associated Equipment* 809 (2016), pp. 96–104.

[37] Martin Prechtl and Christian Wolf. “Das klassische Zyklotron”. In: *Das Lehr-Zyklotron COLUMBUS*. Springer, 2020, pp. 11–15.

[38] Alfred R Smith. “Vision: proton therapy”. In: *Medical physics* 36.2 (2009), pp. 556–568.

[39] David Bohm and LL Foldy. “Theory of the synchro-cyclotron”. In: *Physical Review* 72.8 (1947), p. 649.

[40] Alberto Degiovanni et al. “Status of the Commissioning of the LIGHT Prototype”. In: *9th Int. Particle Accelerator Conf.(IPAC’18), Vancouver, BC, Canada, April 29-May 4, 2018*. JACOW Publishing, Geneva, Switzerland. 2018, pp. 425–428.

[41] Aafke Christine Kraan. “Range verification methods in particle therapy: underlying physics and Monte Carlo modeling”. In: *Frontiers in oncology* 5 (2015), p. 150.

[42] Thomas Bortfeld and Wolfgang Schlegel. “An analytical approximation of depth-dose distributions for therapeutic proton beams”. In: *Physics in Medicine & Biology* 41.8 (1996), p. 1331.

[43] David Robert Grimes, Daniel R Warren, and Mike Partridge. “An approximate analytical solution of the Bethe equation for charged particles in the radiotherapeutic energy range”. In: *Scientific reports* 7.1 (2017), pp. 1–12.

[44] WT Chu, BA Ludewigt, and TR Renner. “Instrumentation for treatment of cancer using proton and light-ion beams”. In: *Review of Scientific Instruments* 64.8 (1993), pp. 2055–2122.

[45] Joseph Perl et al. “TOPAS: an innovative proton Monte Carlo platform for research and clinical applications”. In: *Medical physics* 39.11 (2012), pp. 6818–6837.

[46] Gerald R Lynch and Orin I Dahl. “Approximations to multiple Coulomb scattering”. In: *Nuclear Instruments and Methods in Physics Research Section B: Beam Interactions with Materials and Atoms* 58.1 (1991), pp. 6–10.

[47] Peter Mausbach et al. “Comparative study of the Grüneisen parameter for 28 pure fluids”. In: *The Journal of chemical physics* 144.24 (2016), p. 244505.

[48] Lihong V Wang and Hsin-i Wu. *Biomedical optics: principles and imaging*. John Wiley & Sons, 2012.

[49] Sebastian Lehrack et al. “Ionoacoustic detection of swift heavy ions”. In: *Nuclear Instruments and Methods in Physics Research Section A: Accelerators, Spectrometers, Detectors and Associated Equipment* 950 (2020), p. 162935.

[50] Kevin C Jones et al. “Acoustic-based proton range verification in heterogeneous tissue: simulation studies”. In: *Physics in Medicine & Biology* 63.2 (2018), p. 025018.

[51] Susannah Hickling et al. “Ionizing radiation-induced acoustics for radiotherapy and diagnostic radiology applications”. In: *Medical physics* 45.7 (2018), e707–e721.

[52] HM Lai and K Young. “Theory of the pulsed optoacoustic technique”. In: *The Journal of the Acoustical Society of America* 72.6 (1982), pp. 2000–2007.

[53] Markus W Sigrist. “Laser generation of acoustic waves in liquids and gases”. In: *Journal of applied physics* 60.7 (1986), R83–R122.

[54] Minghua Xu and Lihong V Wang. “Photoacoustic imaging in biomedicine”. In: *Review of scientific instruments* 77.4 (2006), p. 041101.

[55] Lihong V Wang. “Tutorial on photoacoustic microscopy and computed tomography”. In: *IEEE Journal of Selected Topics in Quantum Electronics* 14.1 (2008), pp. 171–179.

[56] Philip M Morse and Herman Feshbach. “Methods of theoretical physics”. In: *American Journal of Physics* 22.6 (1954).

[57] Hans J Weber and George B Arfken. *Essential mathematical methods for physicists, ISE*. Elsevier, 2003.

[58] G Paltauf, H Schmidt-Kloiber, and M Frenz. “Photoacoustic waves excited in liquids by fiber-transmitted laser pulses”. In: *The Journal of the Acoustical Society of America* 104.2 (1998), pp. 890–897.

[59] Vasilis Ntziachristos and Daniel Razansky. “Molecular imaging by means of multispectral optoacoustic tomography (MSOT)”. In: *Chemical reviews* 110.5 (2010), pp. 2783–2794.

[60] Yoh-Han Pao. *Optoacoustic spectroscopy and detection*. Elsevier, 2012.

[61] Frederick W Kremkau. *Sonography Principles and Instruments E-Book*. Elsevier Health Sciences, 2019.

[62] Josef Krautkrämer and Herbert Krautkrämer. *Werkstoffprüfung mit ultraschall*. Springer-Verlag, 2013.

[63] JC Bamber. “Attenuation and absorption”. In: *Physical principles of medical ultrasonics* 2 (1986), pp. 93–166.

[64] W Chen and S Holm. “Modified Szabo’s wave equation models for lossy media obeying frequency power law”. In: *The Journal of the Acoustical Society of America* 114.5 (2003), pp. 2570–2574.

[65] JM Mi Pinkerton. “The absorption of ultrasonic waves in liquids and its relation to molecular constitution”. In: *Proceedings of the Physical Society. Section B* 62.2 (1949), p. 129.

[66] Fikri M Abu-Zidan, Ashraf F Hefny, and Peter Corr. “Clinical ultrasound physics”. In: *Journal of Emergencies, Trauma and Shock* 4.4 (2011), p. 501.

[67] Matthew O’Donnell, ET Jaynes, and JG Miller. “Kramers–Kronig relationship between ultrasonic attenuation and phase velocity”. In: *The Journal of the Acoustical Society of America* 69.3 (1981), pp. 696–701.

[68] T King McCubbin Jr. “The Dispersion of the Velocity of Sound in Water between 500 and 1500 Kilocycles”. In: *The Journal of the Acoustical Society of America* 26.2 (1954), pp. 247–249.

[69] Romard Barthel and AW Nolle. “A precise recording ultrasonic interferometer and its application to dispersion tests in liquids”. In: *The Journal of the Acoustical Society of America* 24.1 (1952), pp. 8–15.

[70] Bradley E Treeby et al. “Measurement of the ultrasound attenuation and dispersion in whole human blood and its components from 0–70 MHz”. In: *Ultrasound in medicine & biology* 37.2 (2011), pp. 289–300.

[71] Jonathan Y Stein. *A computer science perspective*. Wiley, 2000.

[72] Leon Cohen. “The generalization of the Wiener-Khinchin theorem”. In: *Proceedings of the 1998 IEEE International Conference on Acoustics, Speech and Signal Processing, ICASSP’98 (Cat. No. 98CH36181)*. Vol. 3. IEEE. 1998, pp. 1577–1580.

[73] George Turin. “An introduction to matched filters”. In: *IRE transactions on Information theory* 6.3 (1960), pp. 311–329.

[74] Norbert Henze. *Irrfahrten und verwandte Zufälle*. Springer, 2013.

[75] Jannis Schauer et al. “Proton beam range verification by means of ionoacoustic measurements at clinically relevant doses using a correlation-based evaluation”. In: *Frontiers in Oncology* 12 (2022), p. 5055.

[76] Linh T Tran et al. “3D Silicon Microdosimetry and RBE Study Using Ion of Different Energies”. In: *IEEE Transactions on Nuclear Science* 62.6 (2015), pp. 3027–3033.

[77] MATLAB. *MATLAB version 9.3.0.713579 (R2017b)*. Natick, Massachusetts, 2017.

[78] Giuseppe Battistoni et al. “The FLUKA code: Description and benchmarking”. In: *AIP Conference proceedings*. Vol. 896. 1. American Institute of Physics. 2007, pp. 31–49.

[79] Mariano De Souza et al. “Gruneisen parameter for gases and superfluid helium”. In: *European Journal of Physics* 37.5 (2016), p. 055105.

[80] P.G.Grodzka. “Gruneisen Parameter Study”. In: *National Technical Information Servicice* (1967).

[81] Hua Chen et al. “Measurement of the Mie-Gruneisen equation of state for polyimide”. In: *Chinese Science Bulletin* 58.6 (2013), pp. 585–588.

[82] Bradley Treeby, Ben Cox, and Jiri Jaros. “k-Wave,Manual Version 1.1”. In: 1 (2016).

[83] HP Wieser et al. “Experimental demonstration of accurate Bragg peak localization with ionoacoustic tandem phase detection (iTPD)”. In: *Physics in Medicine & Biology* 66.24 (2021), p. 245020.

[84] Alberto Degiovanni et al. “LIGHT: a linear accelerator for proton therapy”. In: *Proceedings of NAPAC2016, Chicago, USA* (2016).

[85] Vincent Favaudon et al. “Ultrahigh dose-rate FLASH irradiation increases the differential response between normal and tumor tissue in mice”. In: *Science translational medicine* 6.245 (2014), 245ra93–245ra93.

[86] Jannis Schauer et al. “Range verification of a clinical proton beam in an abdominal phantom by co-registration of ionoacoustics and ultrasound”. In: *Physics in Medicine & Biology* 68.12 (2023), p. 125009.

[87] *IBA homepage*. URL: https://www.iba-worldwide.com/ (visited on 12/14/2022).

[88] *CIRS homepage*. URL: https://www.cirsinc.com/ (visited on 12/14/2022).

[89] Jannis Schauer et al. *Matched filter in ionoacoustic signal processing for ion beam range determination and dosimetry*. Patent number: 22 159 975.6. 2022.

[90] *Coherent DILAS homepage*. URL: https://www.coherent.com/ (visited on 12/14/2022).

[91] *messtec power converter homepage*. URL: https://www.powerconverter.com/ (visited on 12/14/2022).

[92] Sarah K Patch et al. “Thermoacoustic range verification during pencil beam delivery of a clinical plan to an abdominal imaging phantom”. In: *Radiotherapy and Oncology* 159 (2021), pp. 224–230.

[93] Sarah K Patch, Daniel Santiago-Gonzalez, and Brahim Mustapha. “Thermoacoustic range verification in the presence of acoustic heterogeneity and soundspeed errors–Robustness relative to ultrasound image of underlying anatomy”. In: *Medical physics* 46.1 (2019), pp. 318–327.

[94] Mark Mccavert et al. “Ultrasound is a useful adjunct to mammography in the assessment of breast tumours in all patients”. In: *International journal of clinical practice* 63.11 (2009), pp. 1589–1594.

[95] PR Malone et al. “The use of transabdominal ultrasound in the detection of early bladder tumours”. In: *British journal of urology* 58.5 (1986), pp. 520–522.

[96] CF Dietrich et al. “Improved characterisation of solitary solid pancreatic tumours using contrast enhanced transabdominal ultrasound”. In: *Journal of cancer research and clinical oncology* 134.6 (2008), pp. 635–643.

[97] Umesh Mahantshetty et al. “Trans-abdominal ultrasound (US) and magnetic resonance imaging (MRI) correlation for conformal intracavitary brachytherapy in carcinoma of the uterine cervix”. In: *Radiotherapy and Oncology* 102.1 (2012), pp. 130–134.

[98] Alois Hollerweger, Klaus Dirks, and Kazimierz Szopinski. “Transabdominal ultrasound of the gastrointestinal tract”. In: *EFSUMB Course Book on Ultrasound* (2012), pp. 233–271.

[99] Leo Pallwein et al. “Ultrasound of prostate cancer: recent advances”. In: *European radiology* 18.4 (2008), pp. 707–715.

Acknowledgements

I would like to take this opportunity to thank all the people who supported me during my dissertation and thus contributed to this thesis.

First and foremost, I would like to thank Prof. Günther Dollinger, who supervised my work excellently and contributed to it with many constructive discussions. I would also like to thank him for giving me the freedom to pursue my own ideas.

I would also like to thank Professor Katia Parodi from the Ludwig-Maximilians-Universität, who has enriched the research on ionoacoustics in many constructive meetings. I would also like to explicitly thank her for her networking skills, through which a contact to a clinical radiation facility could be established.

Many thanks to my friend and former colleague Hans-Peter Wieser, who researched the topic of ionoacoustics with me. Without many hours spent together at the blackboard and in the laboratory, this work could not have been realised in this form.

Thanks also go to all the other colleagues who supported me with beam times or in the evaluation of the data. In particular, I would like to thank Yunahui Huang, Julie Lascaud, Matthias Würl and Katrin Schnürle.

A big thank you also to the operators of the MLL and the CAL, who took over the beam preparation and application for the experiments.

Thanks to the workshop manager Ralf Schubert, who took over the manufacture of the holders for the sensors.

Special thanks also go to my colleagues at Unibw, who also provided valuable input, not least in the preparation of this thesis. In particular, I would like to thank Stefanie Girst, Michael Mayerhofer and Matthias Sammer for their contribution.

Last but not least, I would like to thank my family, who have always fully supported me in my work. Many thanks to my wife Lena Schauer and my daughter Marah. I would also like to thank my parents, Susanne Schauer and Andreas Thalmaier, who have supported me throughout my academic career.